Differentiation Between Quark Induced and Gluon Induced Hadronic Jets

Richard Edward Carney

Department of Physics

University of Sheffield

September 1992

Thesis Submitted in Partial Fulfilment
of the Requirements for the
Degree of Doctor of Philosophy
in the subject of Physics.

Abstract

Several variables have been investigated in an attempt to elucidate differences between quark induced and gluon induced hadronic jets of particles. A sample of symmetric 3-jet events (with opening angles $100° \leq \theta_{ij} \leq 140°$) were selected from e^+e^- annihilation data collected by the *ALEPH* detector at $\sqrt{s} = 91.2GeV$ during 1991.

The variables considered were transverse momentum P_t, momentum out of the three jet event plane P_{out}, charged multiplicity N_{ch} and two measures of particle and energy flow - the 'core energy fraction' and 'cone fraction' which determine a jet's energy fraction housed in its central region.

Trends observed in the data do suggest that there are differences between the jet species, particularly in the core energy fraction. However, no decided contrasts can be said to have been exposed, which is in contradiction to expectations founded on QCD parton level predictions. This subsequently implies that underlying differences may be either lost, reduced or hidden during the fragmentation or hadronization process, as they do not clearly manifest themselves in the final hadronic state. Data indications suggest that the effects are both reduced and hidden. Therefore, the methods of analysing the data need to be amended to change our perspective of it, to the effect that it is not the overall value of a distribution that should be considered, but its shape and angular dispersion. This should then allow us to see the contrasts more clearly and resolve this problem more definitively.

Acknowledgements

The writing of a Ph.D. is fraught with ups and downs. However, I can truly say that on any one day there were just as many of one as the other, and anyone who knows of my 'pastime' should get the gist.

Despite being a very self motivated and individual undertaking, no (wo)man is an island, and none of this would have been possible without much help and support. Although not wanting to produce an Oscar acceptance speech, thanking the cast of thousands of 'lovies' (sorry Dicky), several people do deserve a special mention.

First and foremost I would offer much gratitude to my supervisor Professor Fred Combley, for both his guidance and friendship during my time at Sheffield; but also for his undictatorial and non-intimidatory style of supervision, which always kept me at ease and allowed me to produce my best work.

Also, my other colleagues at Sheffield receive my warmest thanks for the encouragement, advice and friendship they have given : John, Chris, Susan, Lee - particularly for the computing expertise, Craig - for taking the abuse (see you !), Fraser, Mahmut, Mike, Daz, Jols, Mark, Hou, Ian and Wayne (where's that reference ? oooharhh !), A mention must also be given to Glen at CERN for many often lengthy discussions and several good ideas.

Finally but by no means least, thanks to my family. Particularly Mom and Dad who started it all by supporting me through my first degree and always allowing me to navigate my own course, and to Mandy who is now as much a friend as a sister (but then she *has* got the car !).

August 28, 1992

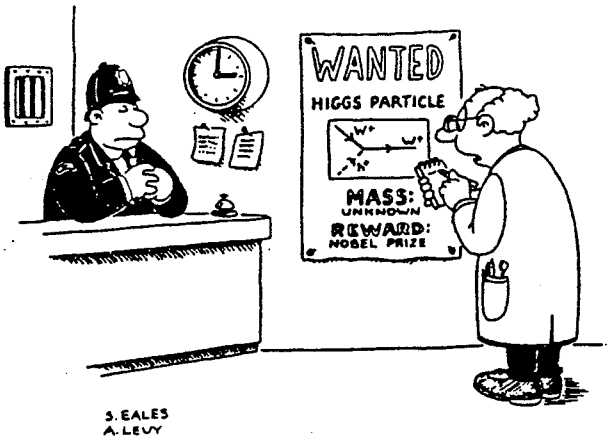

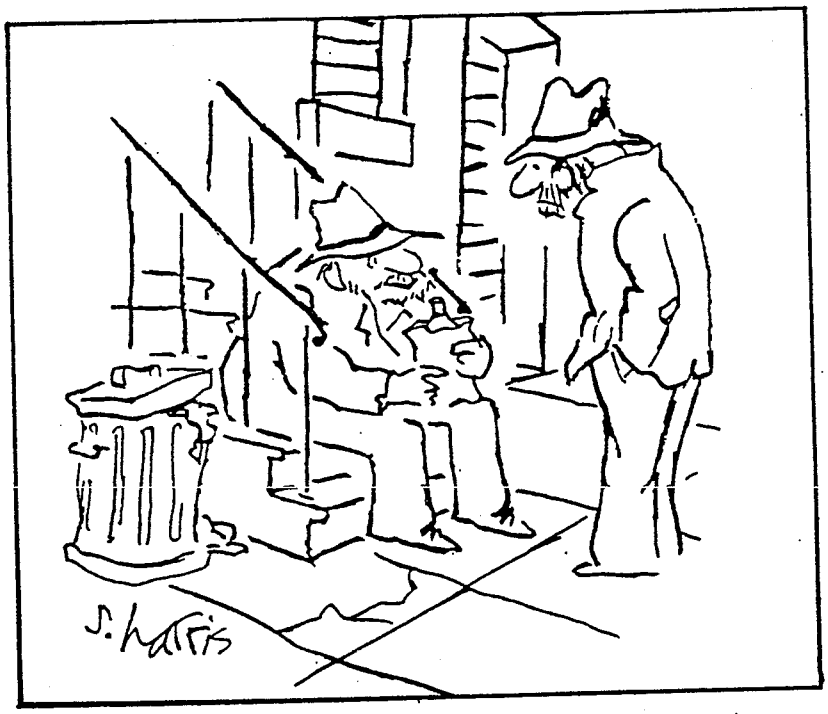

"Quarks. Neutrinos. Mesons. All those damn Particles you can't see. That's what drove me to drink. But now I can see them."

Contents

List of Figures

List of Tables

Chapter 1

Introduction.

Since the dawn of time itself, man has reflected on the nature of matter and the laws governing the universe. Asking such questions as what is matter, how did the universe begin, and why is there an apparent underlying order in nature. In antiquity, philosophers and scientists who pondered these questions believed that everything in existence was composed of the four 'elements' - earth, air, fire and water. However, about 2400 years ago, the Greek philosopher Democritus proposed that matter was composed of tiny indivisible grains and a void, and although primitive, this 'model' does not differ too widely from what we believe today.

The universe appears to have had a definite beginning some 15 billion years ago. This process is now referred to as the 'big bang', which theorists believe was an intensely hot fireball of energy, heat and light. To answer the above questions we need to understand the process of the big bang. The objective of particle physics is exactly this, and by using particle accelerators, the big bang can be created in miniature, back to a time when the universe was less than $10^{-6}s$ old. The particle accelerators which are effectively massive particle racetracks, collide particles at very high energies. In beam-beam machines the particles completely annihilate and all of their kinetic energy and mass converts to pure energy, which in turn reforms into matter and antimatter

particles. Some of which may not have existed since the big bang itself.

All stable matter in the known universe can be built from four fundamental particles, which can be divided into two subgroups known as

quarks - up, down (u, d)

leptons - electron, electron neutrino (e^-, ν_e)

The particles are acted on by four forces, and particles known as bosons mediate these forces. A force is a phenomenon such as attraction or repulsion, via which particles act on each other across the space between them. The four forces are outlined below.

Strong nuclear force - is the most powerful of the four forces and acts to bind quarks together into particles called mesons (quark-antiquark combinations) and baryons (qqq combinations). These are collectively known as hadrons. The mediator of the strong force is the gluon (g).

Electromagnetic force - acts between particles which carry electric charge. It is $\simeq$ 100 times weaker than the strong force, and is responsible for holding the negative electron cloud around the positively charged proton, and builds atoms into molecules. The mediator of the electromagnetic force is the photon (γ).

Weak nuclear force - triggers radioactive β-decay and is $\simeq 10^6$ times weaker than the strong force, but becomes less weak at higher energies. The mediators of the weak nuclear force are the intermediate vector bosons W^+, W^-, Z^0.

Gravitational force - acts between all particles and pulls all matter together. Between individual particles its effect is negligible, and it is only observed on a macroscopic scale. The mediator of the gravitational force has been named the graviton, although its existence is still to be proved.

The basic family of particles above is supplemented by two more 'exotic families' with parallel structures. These are also governed by the above four forces.

quarks - charm, strange (c, s)

bottom, top (b, t)

leptons - muon, muon neutrino (μ^-, ν_μ)

tau, tau neutrino (τ^-, ν_τ)

They are extinct in the modern universe (excepting the muons in cosmic rays) but were in abundance at the time of the big bang. Since the mid 1970's a theory known as the Standard Model has evolved. This is in fact a set of theories which tries to explain the nature of matter and energy as simply as possible. The discovery of the intermediate vector bosons $W^\pm$ and Z^0 was a crucial development for the validation of the model, and observation of the yet unseen top quark and much sought after Higgs particle would all but complete the theory.

Since the end of the last century, several major developments in particle physics have been combined to formulate the 'picture' of the world that we now assume to be correct.

Despite the thoughts of the early philosophers, particle physics can truly be said to have been born in 1887 when J.J. Thompson discovered the electron and put forward the famous, although incorrect 'Plum Pudding Model'. However, Rutherford by use of his α-particle scattering experiment showed that atoms consisted of a nucleus and electrons which were separate. He called the nucleus of the lightest atom - Hydrogen - a proton (p). There now follows a chronological summary of the major events within the field of particle physics since the turn of the century.

1900 - Planck, in attempting to explain the black body spectrum of e.m. radiation emitted by a hot object, found that statistical mechanics, which until that time

had proved very successful for other thermal processes, implied nonsensical results for the e.m. field. This was due to the U.V. catastrophe which implies that the total power radiated should be infinite. However, this can be avoided by quantising the energy into 'packets' with values $E = hf$.

1905 - Einstein proposed that quantisation was in fact a feature of the e.m. field itself and adapted Planck's idea to describe the photo-electric effect.

1923 - Compton, by use of scattering experiments found that light scattered from particles at rest was wavelength shifted. This result led him to conclude that light could be treated as a particle of zero rest mass with energy given by $E = hf$. By applying the laws of conservation of relativistic energy and momentum, light behaves as a particle on a subatomic scale.

The period 1923-1926 saw a rapid formulation of nonrelativistic quantum mechanics.

1927 - Dirac formulated an equation to describe a free electron with energy given by the relativistic formula $E^2 = p^2c^2 + m^2c^4$, but for every positive solution, there exists a negative solution also. This posed a considerable problem, as systems evolve to the lowest energy state, and this required the electron to radiate infinite energy to reach the state $E = -\infty$. Dirac's solution was that the negative energy states were filled by an infinite sea of electrons which was ever present and homogeneous. Therefore, no net force was exerted, and thus, no effect was visible. He then applied the Pauli exclusion principle to explain why an electron in the sea behaved as a net positive charge, and a 'hole' in the sea acted as a particle with positive energy.

1930 - Pauli, while studying nuclear β-decay ($A \rightarrow B + e^-$) believed that due to energy conservation, the electron should be emitted with a fixed energy.

$$E_e = \left[\frac{M_A^2 - M_B^2 + M_e^2}{2M_A}\right] c^2 \tag{1.1}$$

However, experimental results showed the electron energy had a spectrum. Pauli proposed another electrically neutral particle which was responsible for carrying the missing energy.

1931 - Anderson discovered the positron which completely vindicated Dirac's theory. Stuckelberg and Feynman developed this and said that the negative energy states could be reexpressed as positive energy states of the positron, which removed the need for Dirac's sea of holes. However, Dirac's equation has proved to be a universal attribute of quantum field theory, as for every particle, there exists an antiparticle.

1932 - Chadwick discovers the neutron and accurately determines its mass. Thus completing the atomic model.

1933 - Fermi proffers a more complete theory of β-decay including Pauli's unseen particle, the neutrino (ν).

1934 - Yukawa proposed the first significant theory of a strong force, and assumed that protons and neutrons were attracted to each other by a field, just like the electron and proton. The field should be quantised, and due to its short range of force, the mediator should be heavy. The mass was calculated to be $\simeq 300M_e$ or $\simeq M_p/6$. Cosmic ray experiments identified particles matching this hypothesis, but discrepancies were found as they had the wrong lifetime and were also too light.

1947 - Powell finally resolved this problem with the discovery of two particles in cosmic rays - the pion (π) and the muon (μ).

In 1947 all looked well for particle physics, but the discovery of the K^0 particle, and the later discovery of the K^+ in 1949 again began to cloud the issue. Further

particles were also discovered i.e. η, ϕ, ω, ρ, which were all added to the meson family.

1950 - A new neutral particle, the Λ was discovered. This was heavier than the proton, and so, with subsequently discovered particles such as Σ, Ξ, Δ, formed the baryon family.

1953 - Stuckelberg proposed a baryon number which must be conserved. This prevented the proton from decaying as it is the lightest stable baryon.

These new heavy baryons and mesons became known as 'strange particles' as they behaved strangely. They were produced in a time $\simeq 10^{-23}s$ but decayed $\simeq 10^{-10}s$. This was because they were produced by the strong force but decayed via the weak force. Later in 1952 Gell-Mann and Nishijima proposed a new strange quantum number which is conserved in strong interactions but not in weak interactions.

1961 - Gell-Mann introduced a scheme known as the Eightfold Way, which arranged the baryons and mesons into geometrical patterns which were dependent upon their charge and strangeness. The patterns of octets and decuplets were analogous to the work of Mendeleev with the periodic table. One of the decuplets however had a space where an as yet unobserved particle was expected to fit. This was labeled the Ω^- and was discovered in 1964 with all of the attributes predicted by Gell-Mann.

1964 - Gell-Mann and Zweig independently propose that all hadrons are composed of more elementary constituents called quarks. The quark model states that every baryon is a three quark (qqq) state, and every meson is a quark-antiquark ($q\bar{q}$) state. The quarks are always held in confinement as free quarks are never seen. The baryon/meson structure was probed using deep inelastic scattering experiments similar to the α-particle scattering of Rutherford.

Later Greenberg developed the concept of 'colour'. This was used to resolve the problem of the Δ^{++} Δ^{-} Ω^{-} particles which consist of three identical quarks, but since quarks are fermions, they should obey the Pauli exclusion principle. The colour quantum number facilitated this, as it states that any quark may exist with one of three colour charges, labeled red, green and blue. It soon became evident that all naturally occuring particles should be colourless. This also explained why we do not see free quarks.

1974 - The next major development was the simultaneous discovery of the J/Ψ particle by Ting/Richter respectively. It had a mass $\simeq 3M_p$ and a very long lifetime $\simeq 10^{-20}s$ before decaying. The quark model and much debating provided the solution that the J/Ψ was a new meson consisting of a new quark-antiquark combination - the charm quark (c).

At this point everything appeared to be well balanced with four known quarks and leptons. i.e. d, u, s, c and e, ν_e, μ, ν_μ.

1975 - The scales were unfortunately tipped with the discovery of the tau (τ) lepton which presumably had an associated neutrino ν_τ.

1977 - Order was partially restored with the discovery of the Upsilon meson (Υ). This was a heavy meson consisting of a new fifth quark - beauty or bottom. Theory also predicted a sixth quark - truth or top (t), which as yet remains undiscovered but should be found at future accelerators with high enough energy.

In his original theory of β-decay, Fermi treated the process as a contact interaction occuring at a single point and therefore required no mediating particle. The weak force, which is the cause of β-decay has a very short range at low energies and thus approximates to Fermi's contact interaction. However, at higher energies the interaction would have to be mediated by some particle. The Glashow-Weinberg-Salam (GWS) electroweak theory predicted that the force be mediated by the

Lepton	Q	L_e	L_μ	L_τ
e	-1	1	0	0
ν_e	0	1	0	0
μ	-1	0	1	0
ν_μ	0	0	1	0
τ	-1	0	0	1
ν_τ	0	0	0	1

Table 1.1: Leptons and Their Quantum Numbers.

intermediate vector bosons $W^{\pm}$ and Z^0 with masses

$$M_W = 82 \pm 2GeV/c^2$$

$$M_Z = 92 \pm 2GeV/c^2$$

1983 - Rubbia reports the discovery of the W with a mass $M_W = 81 \pm 5GeV/c^2$ and 5 months later the Z with $M_Z = 95 \pm 3GeV/c^2$.

Since 1978 the standard model has evolved to present the view that all matter is created with three types of elementary particles. Leptons, quarks and mediators.

The six leptons are classified according to their charge Q and electron, muon or tau (L_e, L_μ, L_τ) quantum numbers. The leptons thus fall into three families (see table 1.1). There are also six antileptons with the same numbers but reversed signs.

Similarly the 6 (5) quarks can also be classified by charge and quantum numbers, and they too fall into three families (see table 1.2). Each quark also has an associated antiparticle or antiquark, and as with the leptons the numbers are the same with reversed signs. Also, all of the quarks and antiquarks come in three colours - red, green and blue.

Quarks	Q	D	U	S	C	B	T
d	$-\frac{1}{3}$	-1	0	0	0	0	0
u	$\frac{2}{3}$	0	1	0	0	0	0
s	$-\frac{1}{3}$	0	0	-1	0	0	0
c	$\frac{2}{3}$	0	0	0	1	0	0
b	$-\frac{1}{3}$	0	0	0	0	-1	0
t	$\frac{2}{3}$	0	0	0	0	0	1

Table 1.2: Quarks and Their Quantum Numbers.

Finally, every interaction has its mediators. The electromagnetic - the photon (γ), the weak - the $W^{\pm}, Z^0$, and gravity the graviton. But what of the strong force ? In Yukawa's original theory, the pion was supposedly the mediator, but the discovery of heavier mesons crushed this theory as protons and neutrons could exchange ρ, η, K, ϕ etc. However, as baryons and mesons are composite particles, the question was readdressed to ask what mediates the reaction between their constituent quarks. The mediator was called the 'gluon' and in the Standard Model, 8 gluons exist. Like quarks gluons carry colour and are not observed as free entities. The proof for the existence of gluons is very strong, as deep inelastic scattering experiments have shown that 50% of the proton momentum is carried by neutral constituents.

So we now have 12 leptons, 36 quarks and 12 mediators (not including the graviton which is not in the Standard Model). Also the theory requires at least one Higgs particle so we have 61 elementary particles in all. Is this too large a number for the particles to be 'truly' elementary, or is there yet another level of sub-structure to be uncovered ?

Since its inception just over a century ago, the field of Particle Physics has answered many questions and solved many problems with regard to nature's fundamental laws and the structure of matter. However, equally as many, if not more are still to be answered before we can sincerely claim to understand the universe we inhabit. The

desire to find the solutions and attain this goal is what fuels particle physicists world wide to continue their research. Not only to satisfy their own thirst for knowledge, but hopefully for the long term benefit of humankind.

Chapter 2

The Standard Model.

2.1 Introduction.

High Energy Particle Physics is concerned with the study of the fundamental constituents of matter and the interactions between them. The fundamental particles are the spin-$\frac{1}{2}$ Fermions known as quarks and leptons. Four forces act on the particles which are summarised in table 2.1.

Within the scope of the energy range attainable in H.E.P. experiments at present, the gravitational force is negligible due to its very small effect at the distance scales involved. The interactions between the fermions are described using Quantum Field Theories (QFT) or Gauge Theories, which are a hybrid of Quantum Mechanics and Classical Field Theory. In QFT the forces are mediated by integral spin carriers known as bosons, which replace the fields of classical theories. Our overall 'picture' of the

	strong	weak	e.m.	gravity
quark	√	√	√	√
lepton		√	√	√

Table 2.1: The Fundamental Particles and the Forces they Experience.

world is currently described by a theory called The Standard Model, which is actually a combination of separate theories. The electromagnetic (e.m.) and weak interactions have been joined to produce a single theory known as the electroweak theory. In amalgamation with Quantum Chromodynamics (QCD) (discussed in section 2.7) which describes the strong interaction, the resulting theory is the Standard Model. The SM can be said to have been born from Quantum Electrodynamics (QED) which was the initial postulation employed to describe the e.m. interactions of electrons and photons. QED has proved to be very successful in describing the interactions, and is presently the best theory we have within the realms of physics. It thus provided a solid foundation on which to construct the Electroweak theory and the SM. In the following outline of the theory, standard notation and terminology which can be found in works such as [1,2,3,4,5] has been employed, where a more complete description of the topics discussed can also be found.

2.2 Electromagnetism (e.m.) and Gauge Invariance.

In classical e.m. and especially quantum mechanics, it is convenient to replace the magnetic and electric fields (B, E) with a vector potential A^μ.

$$A^\mu = (V, A) \tag{2.1}$$

Where A is a vector and V is a scalar potential, then

$$B = \nabla \times A \tag{2.2}$$

$$E = -\nabla V - \frac{\partial A}{\partial t} \tag{2.3}$$

which arise from the Faraday-Lenz law

$$\nabla \times \left[-\nabla V - \frac{\partial A}{\partial t}\right] = -\frac{\partial(\nabla \times A)}{\partial t} \tag{2.4}$$

and the no magnetic charges law

$$\nabla.(\nabla \times A) = 0 \tag{2.5}$$

The origin of gauge invariance in classical e.m. lies in the fact that the potentials A and V are not unique for given physical fields E and B. The transformations which A and V may undergo while preserving E and B (and hence the Maxwell equations) unchanged are called gauge transformations. The associated invariance of the Maxwell equations is called gauge invariance.

A local change in the electrostatic potential V can be compensated for - in the sense of leaving the Maxwell equations unchanged - by a corresponding change in the magnetic vector potential A. Therefore, by inducing magnetic effects, global invariance under a change of V by a constant can be extended to local invariance.

In general, when a global invariance is generalised to a local one, we require a new compensating field which interacts in a specific way. This is actually the physical field, which is itself invariant under local changes. These dynamical theories are based on local invariance principles and are termed gauge theories.

Applying the quantum operators to the classical energy-momentum relation with $A^\mu = (V, A)$ gives the Schrödinger equation for a particle in an e.m. field. As Schrödingers equation acts on a wave function ψ, then to maintain the harmony between quantum mechanics and Maxwell's equations, ψ must also be gauge invariant. Thus, the gauge invariance of Maxwell's equations is preserved in quantum mechanics so long as transformations to A, V and ψ are combined.

2.3 Generalised Gauge Invariance.

A scalar variable which is Abelian can undergo an infinite set of phase transformations, which form a unitary group $U(1)$. However, more complex transformations are possible involving non-commuting operators, and these belong to non-Abelian groups. Such transformations were proposed by Yang and Mills (1954) and include fields involving both charged and neutral massless bosons, specifically the group $SU(2)$ of isospin which involves the non-commuting group of Pauli matrices τ. Conservation of isospin in strong interactions implies invariance under isospin rotation.

In a similar way to e.m., a gauge invariant description can be formulated by introducing a massless isovector field W_μ, with charged and neutral components, and a coupling constant g.

Thus, although the Pauli matrices are non-Abelian (do not commute) gauge invariance can still be derived. However, this implies an interaction of W_μ with all particles carrying isospin, and hence itself, so the bosons W_μ are both carriers and part of the source of the isospin field. However, the hypothetical charged bosons of the isospin field are massless. Therefore, isospin symmetry in hadronic interactions is not exact as in reality they do not exist.

2.4 Weinberg-Salam $SU(2) \times U(1)$ Model.

In 1967-68 Weinberg and Salam proposed a gauge theory to unify the e.m. and weak interactions into one electroweak interaction. This was based on the $SU(2)$ group of weak isospin I, and a $U(1)$ group of weak hypercharge Y (phase transformations). It employed spontaneous symmetry breaking (SSB) which gave the gauge bosons mass without violating the renormalization criteria (see section 2.6) of the theory.

This can be achieved by introducing an isospin doublet of scalar particles - Higgs scalars - which generate mass as a result of their self interaction, and their use also acts

to remove the divergences in the process $e^+e^- \longrightarrow W^+W^-$. Thus, by introducing scalar particles, the weak isospin field is given mass and the theory is still renormalizable. The fundamental vector bosons are, for $SU(2)$ and $U(1)$ respectively, a massless isovector triplet and a massless isosinglet.

$$W_\mu = (W_\mu^1, W_\mu^2, W_\mu^3) \tag{2.6}$$

$$B_\mu \tag{2.7}$$

As a result of SSB, the three physical bosons W_μ^+, W_μ^-, Z_μ^0 acquire mass, and one, the photon A_μ has no mass. The four bosons are combinations of W_μ and B_μ. Z and A are linear combinations of W_μ^3 and B_μ (which are orthogonal) and $W_\mu^\pm$ are combinations of W_μ^1 and W_μ^2

Consider the electroweak coupling of the leptons. Just as with the gauge bosons, they too have weak isospin and weak hypercharge. Also, we know that the weak charged current (cc) interaction is parity violating as it connects left handed states of the electron and electron neutrino. On the other hand, the e.m. interaction is parity conserving and involves both the left hand and right hand states of the electron. Therefore we assign the lepton states to a left handed doublet and a right handed singlet.

2.5 The Standard Model.

The theory of weak and e.m. interactions combines several ideas. The most important of which is invariance under local gauge transformations. In $U(1)$, global invariance is equivalant to charge conservation, whereas local gauge invariance produces the minimal coupling between the current J_μ and the e.m. field A_μ.

Spontaneous symmetry breaking occurs when the Lagrangian (the Lagrangian is a measure of the interaction energy of the field) of a field theory possesses a certain

symmetry not shared by the ground or vacuum state of the system. e.g. consider an infinite cubic lattice, with particles at the corners having spin and magnetic moment. At high temperature the spins are randomly oriented and the Lagrangian of the system is rotationally invariant. However, below a critical value T_c, the spins begin to align, and this becomes complete at $T = 0$. As one direction has now been singled out, the rotational symmetry of the system is broken. In the case of the complex isodoublet scalar field of $SU(2)$ which has four independent real components, the outcome depends on a continuous parameter μ^2 (analogous to T) in the Lagrangian.

$\mu^2 > 0$ - ground state possesses full symmetry of the Lagrangian and the quanta are four real scalar bosons of identical mass μ.

$\mu^2 < 0$ - symmetry is broken in the ground state and we get one scalar quantum with positive mass (the Higgs) and three massless scalar (Goldstone) bosons.

For theories of this type, a massless scalar field appears for each degree of freedom in which symmetry is spontaneously broken. There is no experimental evidence for the Goldstone boson so we may have created a problem, but if we modify the Lagrangian of the complex isodoublet scalar field so that it is invariant under local $SU(2)\times U(1)$ gauge transformations, the outcome changes. In addition to the four scalar quanta, we now have four vector gauge quanta (3 from $SU(2)$ and 1 from $U(1)$), and when $\mu^2 < 0$ to give SSB, the Goldstone bosons do not appear. Instead the three degrees of freedom to which they correspond appear as an additional degree of freedom (longitudinal polarization) in each of the gauge quanta. The appearance of longitudinal polarization in a vector field is equivalent to mass so we obtain three massive gauge quanta and a fourth massless quantum. Of the four original scalar bosons, only the Higgs remains. This is known as the Higgs Mechanism and is the process where gauge invariance is combined with SSB. In the standard model, the Higgs Mechanism imparts mass to the $W^{\pm}$ and Z^0. The Higgs potential is as yet unobserved and is therefore unknown. There may be many

Higgs particles or it may be a composite particle, but it lets gauge fields acquire mass so the weak, strong and e.m interactions can be described by local gauge theories.

The leptons and quarks must also be coupled to the gauge fields. Weinberg and Salam proposed that the fermions appear in weak left handed isodoublets and a right handed isosinglet to accommodate the parity violating weak interaction. However, the problem of fermion mass generation still remains. In the standard model, the Higgs particle is also responsible for the masses of the quarks and leptons which are assumed to have a Yukawa coupling to the Higgs particle. Introducing a gauge invariant fermion-fermion-Higgs coupling (of Yukawa type) leads to the possibility of neutrino masses and oscillations. The quark-quark-Higgs coupling is related to the Cabibbo angles and the parameter describing CP violation. However, as the Yukawa coupling constant is undetermined we can not calculate the fermion masses, but have to use experimentally measured values until we capture the elusive Higgs.

2.6 Renormalization.

Consider the scattering process $A + A \longrightarrow B + B$. Problems occur when calculating the matrix element for higher order terms. This is due to the inclusion of the virtual loop diagrams of higher order which are divergent at high energies. However, these divergences can be removed by effectively absorbing them into a redefinition of the bare lepton charges and masses, which are in any case only arbitrary. Thus, the physical masses and couplings are not the same as those in the Feynman rules but the renormalized ones.

$$m_{phys} = m + \delta m \tag{2.8}$$

$$g_{phys} = g + \delta g \tag{2.9}$$

δm and δg become infinite but these values are never measured. We only ever look

at m_{phys} and g_{phys}. To take account of the infinities we therefore use the physical values in the Feynman rules and ignore divergent contributions from higher order diagrams. If all of the infinities from higher order diagrams can be accommodated in this fashion, the theory is renormalizable, as is QED. A theory is renormalizeable, if at the cost of introducing a finite number of arbitrary parameters (which are experimentally determinable), the predicted amplitudes of physical processes remain finite at all energies and to all orders of the coupling constant. 'tHooft showed that all gauge theories are renormalizable, which is important, as beyond the lowest order calculations, a non-renormalizable theory results in answers that are cut off dependent and therefore meaningless.

The effective masses and couplings depend on the energies of the particles involved, and are refered to as running masses and running coupling constants. Hence, the effective electron charge is dependent on the momentum transfer q in the collision. Thus, the higher is q, the closer is the approach, so really we can say that the effective charge of particles depends on how far apart they are. This is the result of Vacuum Polarization which screens each charge. According to renormalization theory, not only the strengths of the various interactions, but also the masses of the participating particles appear to vary on differing length scales. The following example makes this clearer to envisage.

Consider firing a cannon under water but neglecting friction. The trajectory of the ball will be different to that on land as the ball will drag an amount of water, which modifies its effective mass. We can measure this experimentally by shaking the ball to and fro' at a rate ω and calculating the mass from $F = ma$. Then, in Newtons equations we replace the true mass by the effective mass and the complicated details of the interaction with the medium can be reduced to determining one effective parameter. Thus, the mass only depends on ω, and as $\omega \longrightarrow 0$ the water has no effect.

Therefore the presence of the medium introduces a scale dependent $m_{effective}$ which

is renormalized by the medium. In quantum physics every particle moves through a medium consisting of all of the quantum fluctuations of all of the particles in the theory. We take into account this medium by ignoring it, but also by changing the values of our parameters to scale dependent effective ones.

2.7 Quantum Chromodynamics (QCD).

The theory of strong interactions between quarks is described by Quantum Chromodynamics (QCD) [6,7,8]. There are presently five (6) known varieties or 'flavours' of quark d, u, s, c, b (where the (6) indicates the expected arrival of the as yet unseen top quark t). However, in the 1960's with the discovery of hadrons such as Ω^-, Δ^{++} it became evident that the quarks required a further degree of freedom which was called colour [9]. Both colour and flavour are only conceptual labels and do not imply a physical colour or flavour of the partons. Colour was introduced to permit three quarks in an s-wave ground state which were consistent with Fermi statistics and the Pauli exclusion principle. However, the three colours of each flavour (labelled red, green and blue) all have the same mass as we do not see any evidence of fine structure in hadronic states. Inter quark forces are colour dependent as we do not observe colour multiplicity in hadronic states. All hadronic states are colour singlets and the force must account for this. Another consequence of colour confinement is the existence of massless gauge fields. This raises the question of what symmetry is involved in QCD.

The u and d quarks provide the ingredients for an approximate flavour isospin symmetry $SU(2)$, and the inclusion of the strange quark results in Gell-Mann and Ne'emans [10] approximate $SU(3)_f$ symmetry. (The f subscript indicates that the $SU(3)$ transformations mix the flavours). However, we also have to include the $SU(3)_c$ colour properties of the quarks, and unlike $SU(3)_f$, $SU(3)_c$ is an exact symmetry which if gauged may provide the theory of strong interactions, but the flavour degrees

of freedom can be related to the gauge group of electroweak interactions.

A baryon consists of three coloured spin-$\frac{1}{2}$ quarks. A non-relativistic wave function could be written as

$$\psi_{3q} = \psi_{spin}\psi_{flavour}\psi_{space}\psi_{colour} \tag{2.10}$$

The product of spin, flavour and space wave functions is symmetric under the interchange of any two quarks. However, as outlined above, we require a colour singlet wave function antisymmetric in colour indices, so we must add an extra antisymmetric component. This is the result of the $SU(3)_c$ colour property and the $SU(3)_c$ transformations which act on the quarks. Thus with ψ^α (α - 1,2,3 - colour index of each quark) then from 3 quarks with 3 colour degrees of freedom (dof), we can form an antisymmetric wave function for the colour dof using the antisymmetric tensor $\varepsilon_{\alpha\beta\gamma}$ which results in

$$\varepsilon_{\alpha\beta\gamma}\psi^\alpha\psi^\beta\psi^\gamma \tag{2.11}$$

this has no free indices and is therefore invariant under $SU(3)_c$ transformations and corresponds to a colour singlet. The two assumptions made are

a) - Each quark flavour exists in three colour states which transform under $SU(3)_c$ transformations.

b) - All observed hadrons are colour singlets.

2.8 Consequences of $SU(3)_c$ Symmetry.

As with QED consider the Dirac equation for a free fermion,

$$(i\partial^\mu - m)\psi = 0 \tag{2.12}$$

as a matrix equation in Dirac space and colour space. This produces 3 Dirac equations for the three colour components

$$\psi_{colour} = (\psi^1, \psi^2, \psi^3) \tag{2.13}$$

If we assume the existence of an exact $SU(3)_c$ symmetry for quarks, we can associate to this the invariance laws of physics. Converting a global non-Abelian phase transformation into a local one introduces eight vector gauge bosons as the eight generators of $SU(3)$ to mediate the forces between the quarks. These are called gluons as they effectively bind the quarks to form hadrons. The gluons belong to an 8_c representation of $SU(3)_c$ and are electrically neutral. Also, as we assume the local $SU(3)_c$ symmetry to be exact and not hidden, the gluons must be massless. An additional condition is that like the quarks, gluons are confined. We never observe free quarks or gluons, only colour singlet combinations

It should be noted that freely propagating particles do not change colour. However, the gauge bosons (gluons) also carry non-Abelian colour charge and are bicoloured. They can therefore self interact which allows 3 and 4 gluon vertices. The coupling at the $q-g$, ggg, and $gggg$ vertices is of equal strength. To ensure the theory remains gauge invariant, these interactions have to be accounted for. Again, as with QED this can be achieved by employing a generalized version of Maxwell's equations. The major difference between this case and electromagnetism is that even in the absence of all but gauge fields, the colour current is non-zero. The gluons self interact even in free space.

2.9 Asymptotic Freedom.

The interaction between two particles can be characterized by an effective charge or coupling parameter which is a function of the distance between them. The effective interactions mediated by non-Abelian gauge quanta tend to zero (logarithmically) at

very close range between the particles. This is what is meant by the term Asymptotic Freedom, and non-Abelian gauge theories are the only theories which support such a mechanism. This is a direct consequence of the gauge bosons carrying the colour charge. Confinement is believed to be due to colour forces at large range. Thus in high energy hard collisions, the quarks and gluons are probed to short distances where they appear to interact weakly and perturbation theory can be applied.

2.10 Perturbation Theory.

In renormalizable perturbation theory, we have a very well understood and reliable calculational procedure. Local non-Abelian gauge theories were proved renormalizable by 'tHooft in 1971 [11,12]. This is not true for globally invariant non-Abelian theories as gauge invariance is a prerequisite of renormalization. However, quarks and gluons are confined and interact strongly, so how can we employ perturbation theory, which is only really effective in relatively weakly interacting theories? This problem highlights one of the major differences between QED, whose fundamental quanta are leptons and photons which are observed as free particles, and QCD, whose quanta, the quarks and gluons are not. To be a valuable test of QCD, a process that is caused by a short range interaction needs to be investigated, so that $\alpha_s(Q^2)$ is small enough for perturbation theory to be applied. Also, if we use the parton model (the lowest order approximation to QCD) a large enough energy and momentum transfer are required to permit an impulse approximation to be used, whereby the time scale of the interaction is short and interactions with spectator partons can be ignored. Fortunately, this is also included in the α_s small requirement. Perturbative QCD can be applied to many experimental situations. However, a consequence of colour confinement is that there is currently no QCD test capable of matching the accuracy of the lepton magnetic moment calculation of QED [13].

2.11 QCD, QED, α and α_s.

In QED the coupling constant $\alpha = \frac{1}{137} \ll 1$, therefore the higher order vertices in Feynman diagrams become negligible, but, in QCD the coupling constant $\alpha_s > 1$ and the higher order, more complicated diagrams contribute increasingly. However, α_s is a running coupling constant dependent on the distance of separation between the interacting particles. Asymptotic freedom states that as $r \longrightarrow \infty$ then $\alpha_s \longrightarrow \infty$ and as $r \longrightarrow 0$ then $\alpha_s \longrightarrow 0$.

In one photon or gluon exchange we have virtual quark loops in QCD and virtual lepton loops in QED which are the constituents of vacuum polarization. However, due to the gluon self coupling, QCD also has virtual gluon loops. In QCD the two types of loop act in opposite senses, as the quark polarization diagrams increase α_s at short range, whereas the gluon loops act to decrease it. In QED two sources of charge can be physically separated to large distances and the physical effective charge is then defined in that limit - $e = e(Q^2 = 0)$, where $Q^2 = -q^2$ for a momentum transfer q. In QCD we can't measure the corresponding physical values g_s or α_s in the limit $Q^2 \longrightarrow 0$, as it is impossible to achieve the required separation. We can however, introduce an arbitrary parameter μ^2 with dimension (mass)^2 so a reference value of α_s is $\alpha_s(Q^2 = \mu^2)$

The quark polarization is dependent upon the number of quarks and hence the number of flavours f, and the gluon polarization upon the number of gluons and thus the number of colours n. A critical value a can be defined

$$a = 2f - 11n \tag{2.14}$$

If a is positive, the effective coupling increases at short distances as with QED, but if $a < 0$ then α_s decreases at short range. At present with $a = -21$ asymptotic freedom is supported and α_s decreases at short range.

In QED

$$\alpha(q^2) = \alpha(1 + (\alpha/3\pi)ln[|q^2|/m^2] + \cdots) \tag{2.15}$$

α increases at large q^2 and short distances. i.e. inside the vacuum polarization screening of the bare charge. Equation 2.15 is the lowest order correction to α for $|q^2| \gg m$. In this limit with $Q^2 = -q^2$.

$$\alpha(Q^2) = \frac{\alpha}{(1 - (\alpha/3\pi)ln[Q^2/m^2])} \tag{2.16}$$

The dominant vacuum poplarization terms can be isolated in each order of perturbation theory and summed explicitly. The equation 2.16 is the result of summing the leading logs.

In QCD

$$\alpha_s(Q^2) = \alpha_s(\mu^2)\left[1 - \frac{\alpha_s(\mu^2)}{12\pi}(33 - 2f)ln\left[\frac{Q^2}{\mu^2}\right] + \cdots\right] \tag{2.17}$$

The gluon self coupling allows them to split and hence 'smear' the QCD charge. Scattering at large Q^2 from diffuse charge is always weaker than from a point source. Again we can sum the leading logs in higher orders

$$\alpha_s(Q^2) = \alpha_s(\mu^2)\left[1 + \frac{\alpha_s(\mu^2)}{12\pi}(33 - 2f)ln\left[\frac{Q^2}{\mu^2}\right]\right]^{-1} \tag{2.18}$$

and $\alpha_s(Q^2)$ decreases as $Q^2 \longrightarrow \infty$ provided $33 > 2f$, i.e. the number of flavours $f \leq 16$. In this case the denominator of equation 2.18 is always positive. However in QED at very large Q^2 the denominator of equation 2.16 tends to zero which results in a singularity and perturbation theory breaks down.

Also, although equation 2.18 at first appears to contain two independent parameters, $\alpha_s(\mu^2)$ and μ^2, if we define

$$ln(\Lambda^2) = ln(\mu^2) - \frac{12\pi}{(33-2f)\alpha_s(\mu^2)} \tag{2.19}$$

then we can rewrite equation 2.18 as

$$\alpha_s(Q^2) = \frac{12\pi}{(33-2f)ln(Q^2/\Lambda^2)} \tag{2.20}$$

and α_s is only dependent upon one parameter in the Leading Log Approximation (LLA). It is very difficult to determine a value of Λ experimentally, but it is typically $\simeq 100 - 200MeV$. For $Q^2 \simeq \Lambda^2$ then $\alpha_s \longrightarrow \infty$ and perturbation theory breaks down. Therefore we can consider Λ as an energy scale at which the strong interaction becomes re-effective and confinement takes over. This is at a distance $\simeq 1fm$ corresponding to $\Lambda \simeq 200MeV$.

2.12 e^+e^- Annihilation into Hadrons.

Hadron production can be divided into four stages as illustrated schematically in figure 2.1. Unlike $p\overline{p}$ collisions, the e^+e^- process is clean as there are only leptons in the initial state. It is therefore not complicated by spectator parton interactions. The four stages are:-

i) e^+e^- annihilation and subsequent $q\overline{q}$ production via the electroweak interaction.

ii) The quarks are at high energies so we can apply perturbative QCD by either

- **a)** Calculating the full matrix elements of perturbative QCD up to a fixed order of α_s.
- **b)** Employing the Leading Logarithm Approximation of perturbative QCD.

iii) Fragmentation (hadronization) occurs as the quarks separate to large distances and small energy scales. Perturbative QCD can not be applied so we resort to phenomenological models.

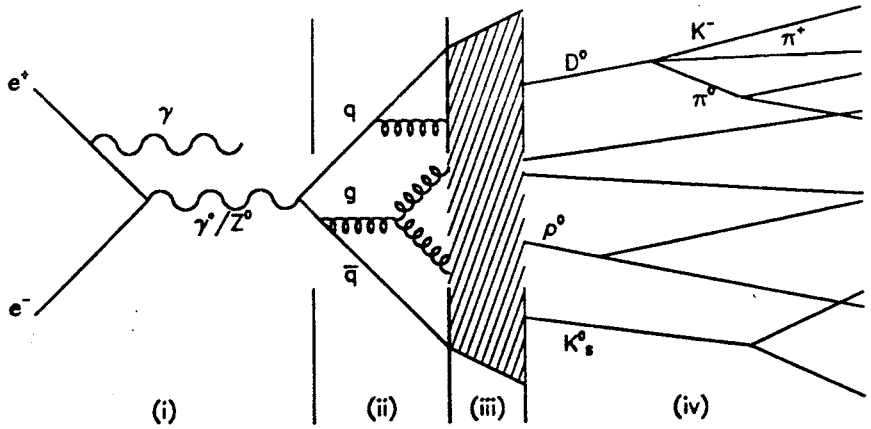

Figure 2.1: The Four Stages of the Process $e^+e^- \longrightarrow$ Hadrons.

iv) Hadrons and decay products of short lived particles emerge as the visible product of the process.

The cross section for the QED process $e^+e^- \longrightarrow \mu^+\mu^-$ is

$$\sigma(e^+e^- \longrightarrow \mu^+\mu^-) = \frac{4\pi\alpha^2}{3Q^2} \tag{2.21}$$

where $s = Q^2 = 4E_b^2$ is the C.M. energy squared. Then for $e^+e^- \longrightarrow q\bar{q}$

$$\sigma(e^+e^- \longrightarrow q\bar{q}) = 3e_q^2\sigma(e^+e^- \longrightarrow \mu^+\mu^-) \tag{2.22}$$

e_q - fractional quark charge.

3 - same diagram for all three colours.

To obtain the cross section for producing all types of hadrons we must sum over all quark flavours.

$$\sigma(e^+e^- \longrightarrow hadrons) = \sum_q \sigma(e^+e^- \longrightarrow q\bar{q}) = 3\sum_q e_q^2\sigma(e^+e^- \longrightarrow \mu^+\mu^-) \tag{2.23}$$

then the ratio

$$R = \frac{\sigma(e^+e^- \longrightarrow hadrons)}{\sigma(e^+e^- \longrightarrow \mu^+\mu^-)} = 3\sum_q e_q^2 \tag{2.24}$$

The ratio R is directly related to the magnitudes of the individual quark couplings to the photon. Also as $\sigma(e^+e^- \longrightarrow \mu^+\mu^-)$ is very well known, a measurement of the hadronic cross section, and subsequent calculation of R, acts as a direct count of the quark flavours and colours. All experimental values of R are consistent with a theory including colour.

2.13 Fragmentation Functions and Their Scaling Properties.

During the fragmentation phase (figure 2.1) the quarks transform into hadrons. This is the least well understood stage of the process and several phenomenological models exist to describe it. (These will be discussed later). However, fragmentation must happen with unit probability to satisfy equation 2.23. In the C.M. frame, the $q\bar{q}$ pair separate with equal and opposite momenta and appear to the observer as two back to back jets of hadrons with momentum approximately colinear with the parent parton directions. The hadrons may have p_t relative to the parton direction $\simeq 0.4GeV$. For the production of a $q\bar{q}$ pair, followed by either of them fragmenting into a hadron h with energy E_h, the differential cross section is

$$\frac{d\sigma}{dz}(e^+e^- \longrightarrow hX) = \sum_q \sigma(e^+e^- \longrightarrow q\bar{q})[D_q^h(z) + D_{\bar{q}}^h(z)] \tag{2.25}$$

The fragmentation functions $D(z)$ are the probabilities of the hadron h being produced from the $q\bar{q}$ with a fraction z of the $q\bar{q}$ energy.

$$z = \frac{E_h}{E_q} = \frac{E_h}{E_b} = \frac{2E_h}{Q} \tag{2.26}$$

The functions describe the parton $\longrightarrow$ hadron transition and are subject to the constraints of momentum and probability conservation.

$$\sum_h \int_0^1 D_q^h(z)dz = 1 \tag{2.27}$$

This is effectively the sum of the energies of all the hadrons, which is the energy of the parent parton.

$$\sum_q \int_{z_{min}}^1 [D_q^h(z) + D_{\bar{q}}^h(z)]dz = n_h \tag{2.28}$$

z_{min} - threshold energy $2m_h/Q$ to produce a hadron of mass m_h.

n_h - average multiplicity of hadrons of type h.

Taking the ratio of equation 2.25 with equation 2.23 and recalling equation 2.22 then

$$\frac{1}{\sigma_0}\frac{d\sigma}{dz}(e^+e^- \longrightarrow hX) = \frac{\sum_q e_q^2[D_q^h(z) + D_{\bar{q}}^h(z)]}{\sum_q e_q^2} \tag{2.29}$$

This is the inclusive cross section divided by the total annihilation cross section into hadrons σ_0. Both of these quantities are Q dependent, but equation 2.29 gives the ratio in a Q independent form.

2.14 QCD Corrections to $e^+e^- \longrightarrow$ Hadrons.

So far we have only considered the leading order process $e^+e^- \longrightarrow q\bar{q}$ of equation 2.23. Three jet events are produced by single bremsstrahlung when either of the $q\bar{q}$ pair radiates a gluon. The ratio of 3 jet events to 2 jet events is controlled by the coupling constant α_s. These events are observed as three fragmenting jets of hadrons. In 3-jet events the $q\bar{q}$ pair are no longer back to back and the $\bar{q}$ has a transverse energy

fraction x_T relative to the q-direction. The observable quantity is now $\frac{d\sigma}{dx_T^2}$. Consider the following energy fractions scaled to the beam energy, where the variables are defined relative to the most energetic jet, whose direction of motion is labelled the Thrust Axis.

$$x_\alpha = \frac{2E_\alpha}{Q} \qquad x_T = \frac{2p_t}{Q} \qquad \alpha = q, \overline{q}, g$$

Energy conservation sets the bound

$$x_q + x_{\overline{q}} + x_g = 2$$

and the partons 4-momenta (assuming coplanarity in the y-plane) are

$$(x_q; 0, 0, -x_q)$$
$$(x_{\overline{q}}; x_T, 0, x_L)$$
$$(x_g; -x_T, 0, x_q - x_L)$$

and assigning the partons zero mass

$$x_{\overline{q}}^2 - x_T^2 - x_L^2 = 0$$
$$x_g^2 - x_T^2 - (x_L - x_q)^2 = 0$$

then we can write

$$x_T^2 = \frac{4}{x_q^2}(1 - x_q)(1 - x_{\overline{q}})(1 - x_g) \tag{2.30}$$

To calculate the cross section we assume that the $\overline{q}$ radiates a soft gluon such that

$$x_q \geq x_{\overline{q}} \geq x_g$$

i.e. the $\bar{q}$ has a transverse momentum fraction x_T relative to the q direction.

Altarelli and Parisi based on the original work of Weizäcker and Williams defined the cross section which computes the probability of producing a gluon.

$$\frac{d\sigma}{dx_{\bar{q}}dp_T^2} = \sigma(e^+e^- \longrightarrow q\bar{q}) f_{\bar{q}g}(x_{\bar{q}}, p_T^2) \tag{2.31}$$

where σ is the probability of producing a $q\bar{q}$ pair, and $f_{\bar{q}g}$ is the probability that the $\bar{q}$ radiates a gluon with a fraction $(1-x_{\bar{q}})$ of its momentum and a transverse momentum $|p_T|$. The cross sections are calculated from probability amplitudes and the different amplitudes for each process (i.e $q\bar{q}$ pair production and subsequent gluon emission) are added, and the squared modulus of the sum is taken.

Then by substitution with

$$f_{qg}(x_{\bar{q}}, p_T^2) = \frac{1}{p_T^2}\frac{\alpha_s}{2\pi} P_{qg}(x_{\bar{q}}) \tag{2.32}$$

$$\sigma(e^+e^- \longrightarrow q\bar{q}) = 4\pi\alpha^2 e_q^2/Q^2 \tag{2.33}$$

$$P_{\bar{q}g}(x_{\bar{q}}) = \frac{4}{3}\left(\frac{1+x_{\bar{q}}^2}{1-x_{\bar{q}}}\right) \tag{2.34}$$

we obtain

$$\frac{1}{\sigma_0}\frac{d\sigma}{dx_{\bar{q}}dx_T^2} = \frac{\alpha_s}{2\pi}\frac{1}{x_T^2} P_{\bar{q}g}(x_{\bar{q}}) \tag{2.35}$$

If we integrate over all possible $\bar{q}$ energy fractions $x_{\bar{q}}$ and substitute for $P_{\bar{q}g}$ then

$$\frac{1}{\sigma_0}\frac{d\sigma}{dx_T^2} = 2\frac{\alpha_s}{2\pi}\frac{1}{x_T^2}\int_{x_{\bar{q}min}}^{x_{\bar{q}max}} \frac{4}{3}\left(\frac{1+x_{\bar{q}}^2}{1-x_{\bar{q}}}\right) dx \tag{2.36}$$

The factor 2 accounts for the fact that the process is equally likely for either the q or $\bar{q}$. The largest value that $x_{\bar{q}}$ can attain is $x_{\bar{q}} = x_q$. This occurs as $x_{\bar{q}} \longrightarrow 1$ and the integrand subsequently diverges. This value is approached if the gluon is very soft, when $x_g = x_T$ (x_T is fixed). Then

$$(x_q)_{min} = (x_{\overline{q}})_{max} \simeq 1 - \frac{x_T}{2} \tag{2.37}$$

and by approximating $1 + x^2 = 2$ and omitting all but the leading log term

$$\frac{1}{\sigma_0}\frac{d\sigma}{dx_T^2} \simeq \frac{4\alpha_s}{3\pi}\frac{1}{x_T^2} log \frac{1}{x_T^2} \tag{2.38}$$

The cross section $d\sigma/dx_q dx_{\overline{q}}$, must be integrated over both x_q and $x_{\overline{q}}$ from 0 to 1,to calculate the order α_s correction to R, but this results in a problem as the integral diverges as x_q or $x_{\overline{q}} \longrightarrow 1$.

$$\frac{1}{\sigma_0}\frac{d\sigma}{dx_q dx_{\overline{q}}} = \frac{2\alpha_s}{3\pi}\frac{x_q^2 + x_{\overline{q}}^2}{(1-x_q)(1-x_{\overline{q}})} \tag{2.39}$$

If either of the denominator terms $(1 - x_q)$ or $(1 - x_{\overline{q}}) \longrightarrow 0$ the $\overline{q}$ and g become colinear and the gluon energy $E_g \longrightarrow 0$. (colinear divergence). If both terms tend to zero the gluon is very soft resulting in an infra-red divergence. We must regularize the integral to remove the singularities (divergences). This is achieved by giving the gluon a fictitious mass m_g. By integrating equation 2.39

$$\sigma_{real} = \sigma_q \frac{\alpha_s}{2\pi}\frac{4}{3}\left[log^2\left(\frac{m_g}{Q}\right) + 3log\left(\frac{m_g}{Q}\right) - \frac{\pi^2}{3} + 5\right] \tag{2.40}$$

where $\sigma_q = \sigma(e^+e^- \longrightarrow q\overline{q})$. However, this is divergent as $m_g \longrightarrow 0$, but as well as emitting a real gluon, the q or $\overline{q}$ can emit or absorb a virtual gluon. The total α_s contribution is

$$\sigma = \sigma_{real} + \sigma_{virtual} = \sigma_q \frac{\alpha_s}{\pi} \tag{2.41}$$

The terms involving m_g in the virtual cross section cancel with those in the real cross section to give a form independent of the fictitious gluon mass. Then including the order α_s correction we have

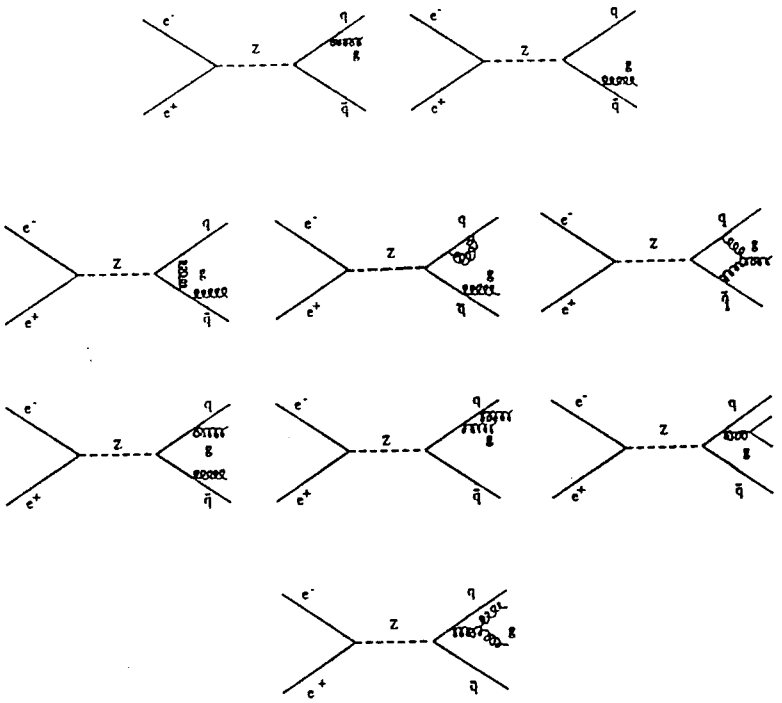

Figure 2.2: Various Diagrams and Loop Corrections which contribute to 3 and 4 Jet Production.

$$R = 3\sum_q e_q^2\left(1 + \frac{\alpha_s(Q^2)}{\pi}\right) \tag{2.42}$$

but this is no longer constant as R has a small dependence on $\alpha_s(Q^2)$.

For the next order $O(\alpha_s^2)$ in the perturbative QCD expansion, four parton final states are possible. i.e. $q\bar{q}q\bar{q}$ and $q\bar{q}gg$. Again we can have 2 or 3 parton diagrams with 2 or 1 virtual parton loops respectively. The $O(\alpha_s^2)$ contribution to the 2, 3, 4, parton cross section (figure 2.2) has been calculated [14,15]. At this order the predictions of the model depend on the renormalization scheme and scale used, as the perturbative expansion is terminated after a finite order.

2.15 Perturbative Calculations and Fragmentation Models [16].

When either discussing or simulating the perturbative phase (ii) of the process $e^+e^- \longrightarrow hadrons$, two procedural models can be employed.

1. Matrix Element (ME) - where the full matrix elements of perturbative QCD are calculated up to the required order of α_s. However, this method currently extends to four parton final states only.

2. Parton Showers (PS) - where the initial $q\overline{q}$ pair are allowed to cascade via the processes $q \longrightarrow qg$, $g \longrightarrow gg$, $g \longrightarrow q\overline{q}$. In the LLA of perturbative QCD the leading logs of the probabilities of these branchings are summed to all orders. At each branching, the parton energy decreases and the shower is terminated when the energy reaches a cut off value Q_0. This method allows for many parton final states.

The process by which the partons $\longrightarrow$ hadrons is known as fragmentation or hadronization. Perturbation theory can not be used here but we do have phenomenological models in which parameters are tuned to fit the data. The three most commonly used models are outlined below.

2.15.1 Independent Jet Fragmentation.

This model was initially designed by Field and Feynman for $e^+e^- \longrightarrow q\overline{q}$ only but was later modified by Hoyer, then Ali to include gluons, with the rate of 3 and 4 jet events controlled by α_s. All of the partons are treated as separate and independent entities. Each jet is produced by a cascade process of the form $Q \longrightarrow q + \overline{q}Q$. i.e. a $q\overline{q}$ pair is created from the colour field of the original parton Q, the $\overline{q}$ and Q join to form a meson and fragmentation continues as the q subsequently becomes the Q. Gluons are treated

via the process $g \longrightarrow q\overline{q} \longrightarrow hadrons$ and cuts are applied to control the singularities caused by soft or colinear gluon bremsstrahlung. Transverse p_t and longitudinal p_L momentum distributions are parameterized in the fragmentation functions. Neither energy, momentum or flavour are conserved, but are rescaled and corrected 'by hand' at the end of the cascade, which tends to scale the gluon momentum up. This model does not describe the observations of hadronic events very well.

2.15.2 String Fragmentation [17].

A $q\overline{q}$ pair separate and lose energy to the colour field between them. As the separation increases the string between the partons is stretched, increasing its stored energy until the string breaks, (stored energy $\simeq 1GeV/fm \simeq 16tons/m$) forming a new $q\overline{q}$ from the released energy. There are now two strings and the above process continues until all of the strings are small. Hadrons are formed from the $q\overline{q}$ at the string ends. Gluons are treated as kinks in the string between the $q\overline{q}$. The string fragments into mesons in its own rest frame which results in more soft particles between qg and $\overline{q}g$ jets than between the $q\overline{q}$ jets. This is referred to as the String Effect [18]. Again the p_t and p_L distributions of the hadrons are parameterized in the fragmentation functions, but in this case energy and momentum are conserved at each step. Divergences are avoided by introducing a cut in momentum on the gluon strength ($Q_0 \simeq 5 - 10GeV$) below which a 2 jet form is employed. In contrast to the Independent Jet model, calculations usually include all terms to $O(\alpha_s)$ and consequently describe the data very well.

2.15.3 Cluster Fragmentation.

This model is only applied at the end of a Parton shower whereas the preceding two schemes can be used after either Matrix Element or Parton Shower calculations. All gluons are treated as $q\overline{q}$ pairs which are combined with final state q and $\overline{q}$ into colourless clusters. The clusters then decay into hadrons. As this model is used after Parton

Showers, the LLA approach ensures that QCD vertices are present to all orders but they are not complete.

Chapter 3

L.E.P. And The ALEPH Detector.

3.1 Large Electron Positron Collider (L.E.P.)

In December 1981, after several preliminary studies which commenced in 1976, the CERN council authorized construction of the Large Electron Positron Collider (LEP). This is a giant particle accelerator designed to operate at centre of mass energies $E_{cm} \leq$ 110GeV during phase I or LEP100 and $E_{cm} \leq$ 200GeV (with a possible upgrade to 240GeV) in phase II or LEP200.

LEP [19] is the largest machine ever constructed, and is a powerful and precise scientific instrument which particle physicists are employing to primarily study electroweak interactions. In the 19th. century, a major theoretical advancement was the proof by Maxwell that electricity and magnetism, which were previously thought of as separate entities, were in fact different manifestations of the same quantity. An attempt to combine the electromagnetic (e.m.) and weak nuclear force in a similar fashion predicted a new form of particle interaction - the neutral current - which was first observed at CERN in 1973. Theory also predicted that there should be three bosons to mediate

the weak force. The $W^{\pm}$, responsible for radioactive β-decay, and the Z^0 for neutral currents.

LEP is an ideal machine for detailed studies of the electroweak phenomena, under conditions where the weak force becomes comparable in strength with the e.m. force. In particular, the Z^0 intermediate vector boson, which is produced in the copious quantities of $\simeq 10^4 day^{-1}$ is being studied to determine its rare decay modes, and a precise measurement of its parameters such as its lifetime and line shape are also being made. In addition to this, the production of hadronic states and a determination of the number of neutrino species is also under investigation. This can all be facilitated at LEP100, but after the upgrade to allow operation at higher centre of mass energies, the charged intermediate vector bosons W^+ and W^- and the $Z^0 - W^{\pm}$ coupling can be probed. This will take place during phase II at LEP200. Also at LEP200, it is hoped that new physics will be uncovered. This may include discovery of the Higgs' boson, which is thought to be responsible for giving all particles their mass, observation of the predicted but as yet unobserved top quark and the discovery of supersymmetric (SUSY) particles.

Construction of LEP began in 1983 and was completed in 1988. The official commissioning of the machine took place in July 1990.

The LEP accelerator is situated in a tunnel which straddles the Franco-Swiss border in the canton of Geneva and the Pays De Gex. Due to geological considerations the tunnel is not horizontal, but is inclined at an angle of 1.42°. It has a circumference of 26.658Km., and although described as a ring, is in fact an octagon with rounded corners. This consists of 8 straight sections of length 490m and 8 arcs of length 2840m. There are 3368 dipole magnets in the arc sections which act to bend the beams, and 1904 focusing and correcting magnets which reside in both the arcs and straight sections. (776 quadrapoles, 504 sextupoles, 8 superconducting quadrapoles and 616 orbit correctors). There are 8 collision points on the ring situated at the centres of the straight

sections. Each alternate site houses a specialist particle detector experiment, the four being known as ALEPH, OPAL, DELPHI and L3. As electrons and positrons are the same particle-antiparticle and only differ by charge, they can circulate in the same beam pipe, employing the same focusing and bending apparatus for both beams. The beams themselves are not continuous, but consist of 'bunches' of particles. Each bunch is $\simeq 1.8cm$ long and $\simeq 1-2mm$ high and wide. The time between bunch crossings is $23\mu s$, and the maximum beam current is $\simeq 1.3mA$ per beam. The collision points are equidistant and even in number, as are the bunches of counter rotating beams of electrons and positrons. However, the number of bunches is four, which results in 8 collision points, so electrostatic separators are used to ensure collisions occur only at the detector sites.

There are two performance parameters of particular importance. These are the beam energy E and the luminosity $\mathcal{L}$. As the electrons and positrons travel in opposite directions at the same speed, the energy available from an interaction is just $2E$. The rate at which interactions take place is proportional to the luminosity and the beam cross section.

$$\mathcal{L} = \frac{N^2 k f}{4\pi\sigma_x\sigma_y} \tag{3.1}$$

N - No. of e^+e^- in each bunch.

k - No. of bunches.

f - revolution frequency.

$\sigma_x\sigma_y$ - horizontal and vertical r.m.s. beam radii
assuming a Gaussian density distribution.

Thus, high luminosity requires a large numerator and a small denominator. However, the number of particles per bunch has two serious limitations - synchrotron radi-

ation and beam-beam interactions which are interactions with the e.m. fields created by the beams within the vacuum of the beam pipe. Electrons and positrons circulating with an orbit of radius ρ lose energy by synchrotron radiation at a rate $\propto E_{beam}^4$ at constant current. In radio frequency (RF) systems constructed from copper (typical of many e^+e^- storage rings) the RF power requirements are dominated by losses in the cavities. Therefore, synchrotron radiation sets an upper limit on the beam current and energy. The synchrotron radiation power is emitted as soft X-rays which strike the vacuum wall where they are absorbed. The resulting heat is dissipated with cooling water. The vacuum chamber walls are aluminium with a coating of lead which is a few millimetres thick to absorb the more penetrating X-rays.

The circulating bunches excite the e.m. fields within the vacuum chambers to produce the effect known as 'wakefields'. The wakefields increase with increasing beam current and decreasing bunch length. The wakefields react back on the bunches to limit the current within them. The largest contribution to the wakefields comes from the RF cavities as they make the largest change to the beam pipe cross section. The revolution frequency is inversely proportional to the machine circumference. The circumference is in turn proportional to the orbiting radius ρ and the length of the RF system L_{RF}, and ρ and L_{RF} are proportional to E_{beam}^2.

The beam-beam effect sets a lower limit on the allowable beam size. The particles in the e^+ beam are attracted by the e.m. field of the particles in the e^- beam and vice versa. This causes an increase of the betatron tune which is the number of oscillations produced along the circumference of the machine due to the focusing action of the magnets. The largest change in the tune is due to particles oscillating with small amplitudes compared to σ_x and σ_y at the crossing points and is given by

$$\varepsilon_z = \frac{N r_e \beta_z}{2\pi y \sigma_x (\sigma_x + \sigma_z)} \tag{3.2}$$

z - either x or y.

β_z - amplitude function in the x or y direction at the crossing point.

r_e - electron radius.

y - beam radius in the y direction.

Thus

$$N = \frac{\varepsilon_z 2\pi y \sigma_x (\sigma_x + \sigma_z)}{r_e \beta_z} \tag{3.3}$$

and by substituting into equation 3.1

$$\mathcal{L} = \frac{N k f \varepsilon_z y (\sigma_x + \sigma_z)}{2 r_e \beta_z \sigma_y} \tag{3.4}$$

and as $\sigma_x \ll \sigma_y$

$$\mathcal{L} = \frac{N k f \varepsilon_y y}{2 r_e \beta_y} \tag{3.5}$$

Therefore the experimental collision points are at sites where β_x and β_y are low, and σ_x and σ_y are reduced to a fraction of a millimetre.

The design procedure is thus to produce E, $\mathcal{L}$, ε_y, and β_y compatible with synchrotron radiation and wakefields. Therefore the machine size is an optimization between the cost of size ($\propto \rho$) and the cost of the RF apparatus ($\propto \rho^{-1}$).

3.1.1 Injection And Beam Transfer.

The injection system for LEP (figure 3.1) is capable of delivering 1.6×10^{12} of both electrons and positrons in 12 minutes, whenever LEP is to be filled. This corresponds to a beam current of 3mA in each beam with four bunches per beam. The LEP Pre-Injector (LPI) consists of LEP injector LINACS (LIL) and an e^+e^- accumulation ring (EPA).

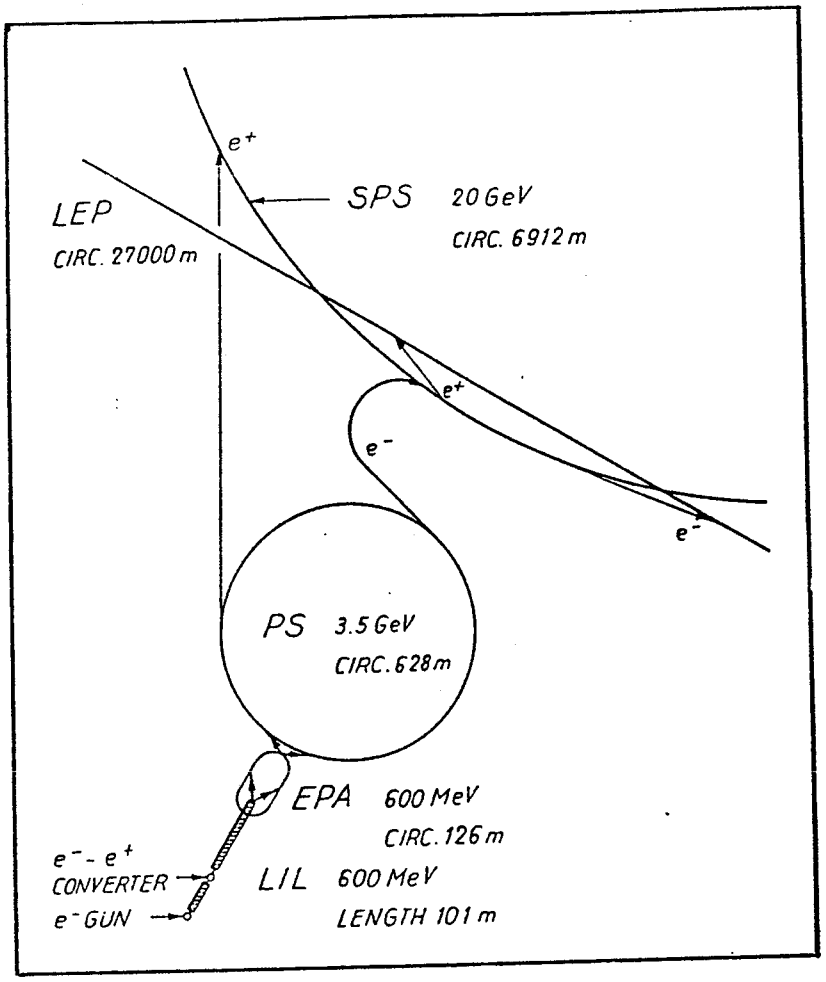

Figure 3.1: The LEP Injection And Transfer System

LIL - consists of two LINACS in tandem operating at $100Hz$. The first is a $200MeV$ machine and produces electron pulses of $2.5A$ (peak) for $\simeq$ 10-20ns. Positrons are created by colliding the electron pulse with a fixed tungsten target. The second LINAC accelerates the positrons to $600MeV$. During the electron production, the electron gun current is reduced and the tungsten target is removed from the LINAC. The acceleration of the second LINAC is reduced to $400MeV$.

EPA - has a racetrack shape with a circumference of $126m$. It acts as a particle buffer between the LIL operating at $100Hz$ and the Proton-Synchrotron (PS) operating at $0.8Hz$.

PS - accelerates either the e^+ or e^- to $3.5GeV$ for injection into the Super Proton-

Synchrotron (SPS).

SPS - accelerates the particles to $20GeV$ before the beams are finally injected into the LEP ring, where they are ultimately accelerated up to energies of $50GeV$ per beam.

The use of the existing $450GeV$ SPS and $28GeV$ PS greatly reduced costs as only the LPI and new e^+e^- transfer lines from LEP to the SPS had to be constructed. An SPS cycle time is $\simeq 15s$ so two electron and two positron acceleration cycles, both $\simeq 1.2s$ long can be accommodated between the $450GeV$ proton cycles. The pair of beams in LEP are accumulated over approximately 50 SPS cycles. Positron production in LIL is much lower than that of electrons, so the positrons are produced for $\simeq 10s$ and are accumulated in 8 bunches in the EPA during each SPS cycle. Half of the accumulated positrons go to the PS for the two positron acceleration cycles, then the electrons are accumulated for two electron acceleration cycles before resumption of positron production.

3.2 The ALEPH Detector.

The Apparatus for LEP Physics or ALEPH detector (figure 3.2) [20,21,22] is housed at collision point (or 'pit') number 4 of the LEP accelerator. This in turn is situated a few Kilometres inside the French border near the village of Echenevex.

Events at LEP100 contain typically 20 charged and 20 neutral particles which are generally contained within clusters or jets. However, as the event rate is only $\simeq 1Hz$, the detector was designed to cover as much solid angle and to collect as much data per event as possible. The detector as a whole can be considered as three macroscopic components. The barrel section and two end-cap regions. These are divided into several subdetector components, each of which plays a specific role in the data collection process. The detector is briefly described below, followed by a more in depth examination

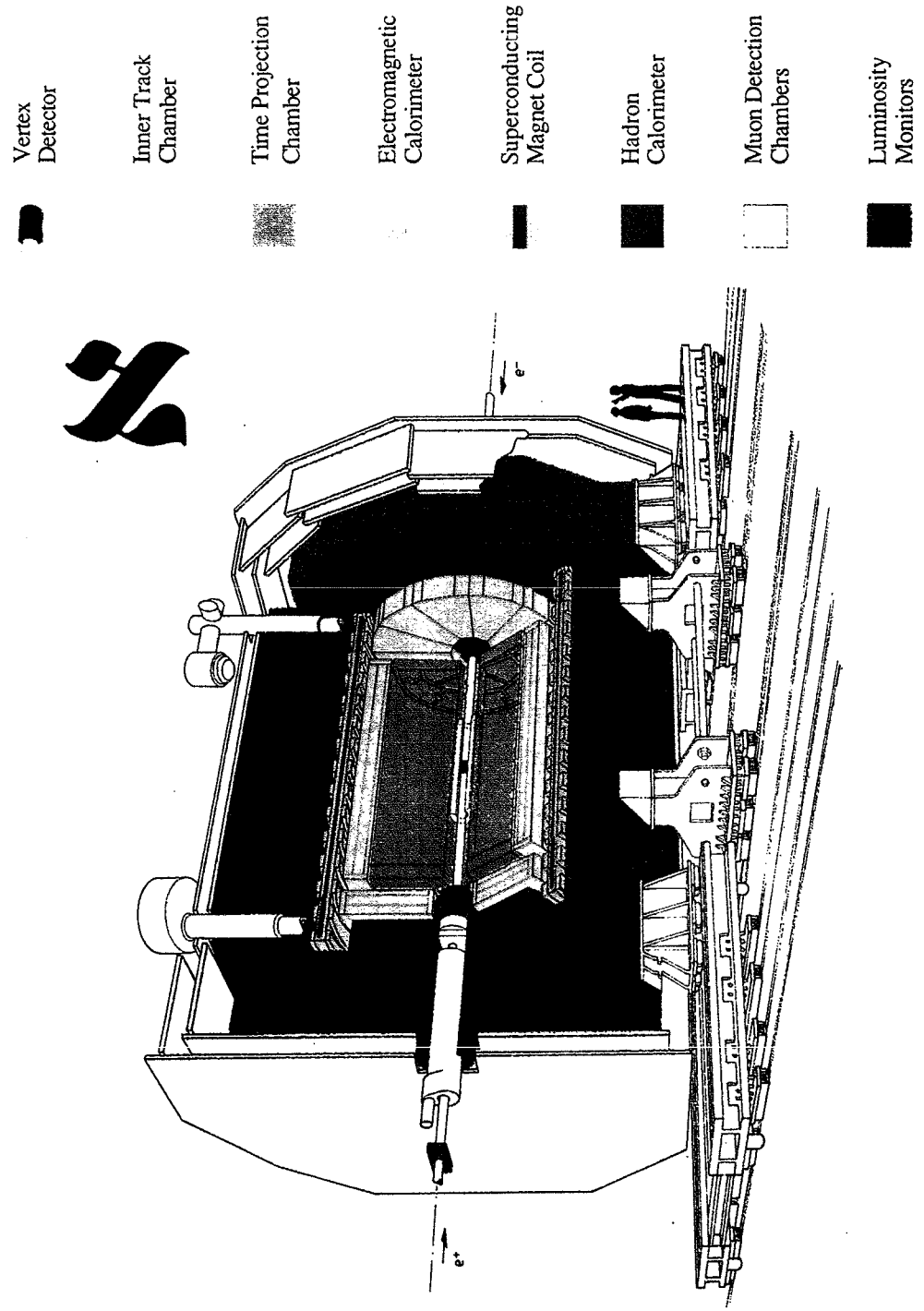

Figure 3.2: The ALEPH Detector.

of each subdetector.

Several hundred physicists from 30 mainly European, but also American and Chinese laboratories have worked together to construct and operate the detector. Its overall dimensions are $\simeq 12 \times 12 \times 12m^3$ and its mass is $\simeq$ 3000 tons. The detector extends radially from the beam pipe which is a 96% Al, 3.2% magnesium alloy tube of diameter 156mm and wall thickness 0.5mm. The first layer encountered is the Minivertex detector (VDET) which is a double layer silicon strip detector. This gives two pairs of coordinates at 9.6cm and 11.2cm radius from the beam axis with an accuracy of $\simeq 10\mu m$. Next is the Inner Tracking Chamber (ITC). This is a drift chamber with axial wires, an inner radius of 13cm, outer radius of 29cm and length of 2m. It gives up to eight coordinates per track in the $r - \phi$ plane with an accuracy $\simeq 100\mu m$. The Time Projection Chamber (TPC) completes the central tracking chamber group. Their purpose is to measure the emission angles and curvature of the charged particle trajectories. The TPC is a large tracking chamber with a diameter of 3.6m and length of 4.4m. It provides 3-dimensional measurements of tracks and yields a p_t accuracy of $\Delta p_t/p_t^2 \simeq 10^{-3}(GeV/c)^{-1}$ if used in combination with the ITC. Also, particle identification from energy loss from dE/dx measurement is possible.

The next group of subdetectors are the calorimeters, which are designed for energy measurement. The first is the Electromagnetic Calorimeter (ECAL). This is built from sandwiches of lead sheets and proportional tubes which are read out in 73,728 projective (i.e. pointing back to the interaction vertex) towers. The towers are subdivided into three depth layers or storeys. The ECAL was designed to give the highest possible spatial resolution and good electron identification. The Hadron Calorimeter (HCAL) is a very large array of layered streamer tubes and iron plates. The tubes form 4608 projective towers, and the iron, with a total thickness of 1.2m acts not only as a detector medium but also as the magnet return yoke. Finally the muon chambers consist of two double layers of streamer tubes which act to identify muons which traverse the

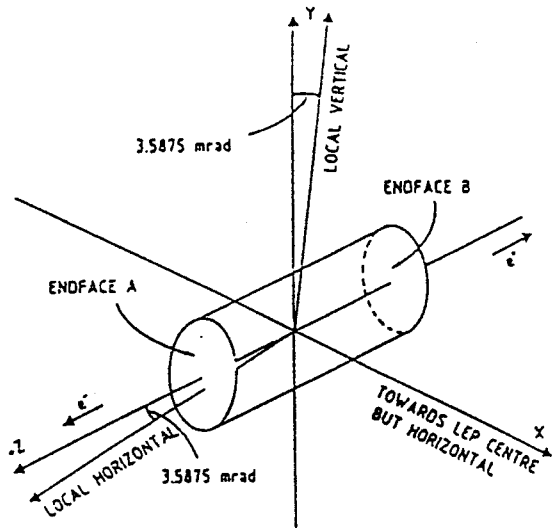

Figure 3.3: The ALEPH Coordinate System.

HCAL. Between ECAL and HCAL sits the superconducting solenoid, which at 6.4m long and with diameter of 5.3m, provides an axial magnetic field of 1.5T. This high field facilitates good momentum resolution in the tracking chambers.

Luminosity is determined by measurement of small angle Bhabha scattering. Three components are used for this task. The Luminosity Calorimeter (LCAL) and Small Angle Tracker (SATR) sit around the beam pipe at a distance of approximately 2.5m from the interaction point. The Bhabha Calorimeter or Small Angle Luminosity Monitor (BCAL/SALM) is also situated around the beam pipe but at the greater distance of 770cm from the interaction point.

In describing the subdetectors, many references are made to positional and spatial coordinates. The coordinate and naming system used by ALEPH can be seen in figure 3.3

The origin is the theoretical beam crossing point. The positive z-direction is that in which the electrons flow (i.e. anticlockwise). Due to an inclination of 1.42° of the LEP ring, the z-axis is 3.5875mrad to the local horizontal. The positive x-direction points

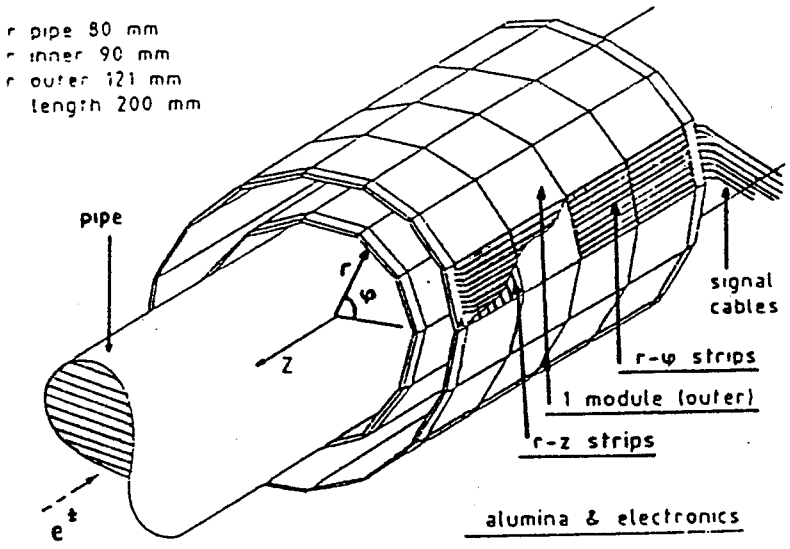

Figure 3.4: The ALEPH Minivertex Detector.

radially towards the centre of the LEP ring, and the positive y-direction is orthogonal to x and z and points skyward. The spherical components are thus

$$x = r \sin\theta \cos\phi$$

$$y = r \sin\theta \sin\phi$$

$$z = r \cos\phi$$

ϕ in x-y plane is radially about z-axis.

θ in y-z plane is radially about the x-axis.

3.3 The Minivertex Detector (VDET).

Vertex detectors allow highly precise 3-dimensional track reconstructions to be made. This in turn affords improved momentum measurement and permits the identification and lifetime measurement of short lived particles. The ALEPH Minivertex detector

[23] measures $r-\phi-z$ coordinates and is designed to reconstruct events with multistep decays. It is situated around the beam pipe and inside the ITC, with outer and inner radii of $80mm$ and $128mm$ respectively.

3.3.1 Construction.

The VDET consists of two concentric surfaces or barrels of length $200mm$. The inner barrel is dodecagonal with a radius of $95mm$ and covers 76% of 4π solid angle. The outer barrel is hexadecagonal with radius $114mm$ and has an angular coverage of 67% of 4π. (fig 3.4). Each surface of the two barrels is constructed from silicon wafer microstrip detectors of thickness $300\mu m$ and area $51.2 \times 51.2mm^2$. There are four wafers along the length of each module, giving a total of 112 wafers on all 28 surfaces. Individual strips are mounted on both sides of the wafers, with the strips on one side parallel to the beam to measure the ϕ coordinate, and on the other the strips are perpendicular to the beam to measure the z coordinate. The radial coordinate r is determined from the position of the wafer. The strip pitch is $25\mu m$ in $r-\phi$ and $50\mu m$ in z. However, the readout pitch is $100\mu m$ in $r-\phi$ and $200\mu m$ in z as only every fourth strip is used for the readout, but the three strips between are used to improve the position resolution.
The inner layer has 12,288 $r-\phi$ and 21,505 z strips.
The outer layer has 7,168 $r-\phi$ and 10,240 z strips.
The total of 51,200 strips are readout through charge sensitive preamplifiers which are multiplexed by a factor $\simeq 60:1$ to give 1008 readout channels.

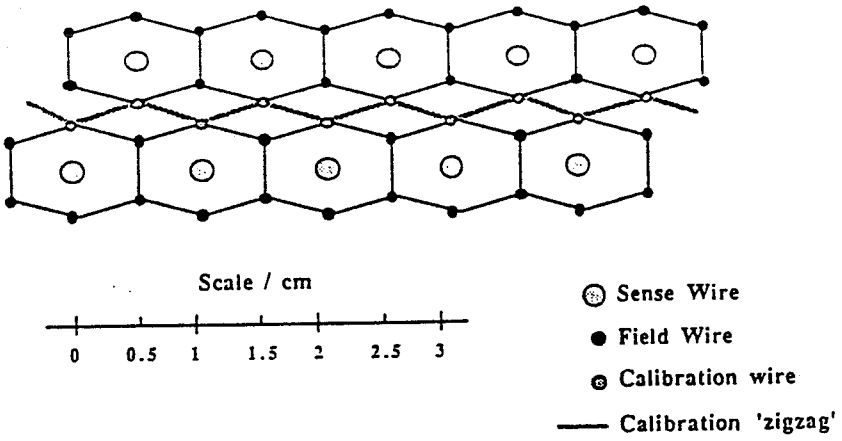

Figure 3.5: The Hexagonal Structure of the ITC Drift Cells.

3.3.2 Resolution.

Single track resolution is

$$\sigma_{r\phi} = 13\mu m. \tag{3.6}$$

$$\sigma_z = 20\mu m. \tag{3.7}$$

and two tracks can be resolved to $200\mu m$ in $r-\phi$ and $400\mu m$ in z.

3.4 The Inner Tracking Chamber (ITC).

The ITC is a conventional cylindrical, multiwire drift chamber with small hexagonal staggered cells. There are eight concentric layers of sense wires in the region $r = 160 - 260mm$, which are parallel to the z-axis. The wires are gold plated tungsten with a diameter of $30\mu m$, and are arranged with 96 wires on the inner four layers and 144 wires on the outer four layers. (960 total). The wires can give up to 8 $r-\phi$ coordinates accurate to $\simeq 100\mu m$, calculated from drift time, and a z coordinate with accuracy of $3cm$ calculated from pulse arrival time difference at each end of the wire.

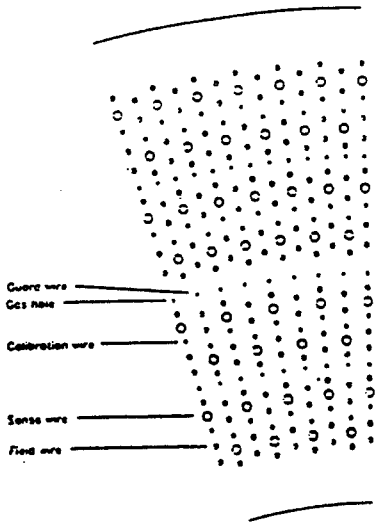

Figure 3.6: Detail of the ITC End-Plate.

3.4.1 Construction.

The ITC is a cylinder of length $2m$, inner radius $128mm$ and outer radius $285mm$. The outer wall is $2mm$ thick carbon fibre and the inner, a $2mm$ thick low mass polystyrene with an aluminium foil coating. The wires are strung from two aluminium end plates. The electronics are situated behind the Al plates and additional flanges provide extra support.

The drift cells are hexagonal and are arranged in a close packed structure (figure 3.5). The sense wire sits in the centre of the cell and is surrounded by 6 field shaping wires (gold plated aluminium - diameter $147\mu m$ - 3840 total), of which 4 are shared with neighbouring cells. The sense wires are held at a positive potential in the range 1.8 - 2.5kV, and the field wires are held at earth. Additionally, one field wire per cell is insulated and passes through the end plate so that a calibration pulse can be applied to each cell. This is more clearly illustrated in figure 3.6.

One of two gas mixtures below can be used in the chamber, with the second currently employed.

1. $Ar50\% - C_2H_6(ethane)50\%$ has a gas gain of 1.9×10^4 at 2.1kV and 5.2×10^4 at 2.3kV. The plateau in detection efficiency is reached at 2.0kV and the operating voltage is in the range 2.2 - 2.4kV.

2. $Ar80\% - CO_220\%$ has a gas gain of 1.2×10^4 at 1.8kV and 4.9×10^4 at 10^4kV. The plateau is reached at 1.85kV and the operating range is 1.85 - 2.05kV.

3.4.2 Electronics.

The signal wires are connected to preamplifiers with a voltage gain of 3X. Then the signal passes to the main amplifier with a gain 36X and is discriminated at a constant fraction threshold. The discriminator outputs from one end of the chamber are fed to Time to Digital Converters (TDC's), where a gated digital signal switches on a capacitor charging circuit. This is halted by the arrival of the signal at the other end of the chamber. During the period between the stop/start signals, a second current discharges the capacitor at a rate dependent on the wire layer (i.e. wire radius). The ratio of the charging and discharging current is known as the 'time expansion factor', and the time taken for the capacitor to reach zero is proportional to the charge deposited on it. Hence, the z-coordinate of the wire pulse can be calculated.

3.4.3 Triggering.

The ITC has two trigger processors which provide information within $2 - 3\mu s$ of the bunch crossing. The speed of the trigger decision is dependent upon drift time, hence the choice of small cells. The ITC is the only track detector used in the Level I trigger. Tracks, and thus a trigger decision are determined as follows.

1. A hit wire latch is used to search for tracks in radial patterns of wire cells. This provides $2 - d$ coordinates in $r - \phi$.

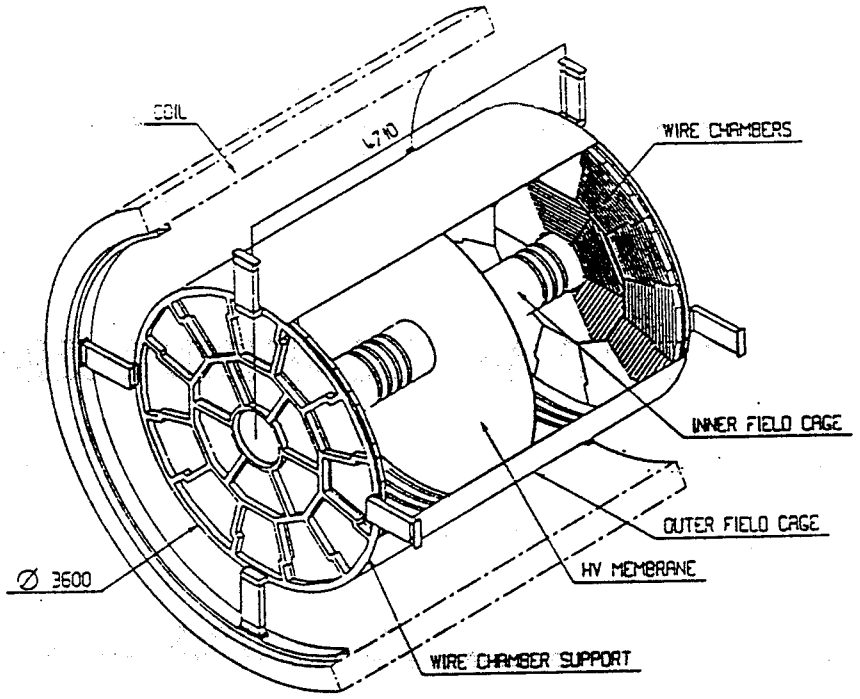

Figure 3.7: The Time Projection Chamber.

2. Pulsed outputs are used to determine the z-coordinate as described above, and this allows $3-d$ coordinates in $r-\phi-z$ to be calculated.

3.5 The Time Projection Chamber (TPC).

The TPC (figure 3.7) is a $3-d$ imaging drift chamber and is the main ALEPH central tracking detector. It's purpose is to give accurate momentum and emission angle values for charged tracks, and to aid particle identification from energy loss through dE/dx measurements. The chamber is cylindrical with parallel, axial magnetic and electric fields. The electric field propogates from two end plates towards a central membrane which divides the chamber into two halves. Each end plate houses 18 wire chambers (sectors) which can measure up to 21 $3-d$ coordinates per track. This typically yields an $r-\phi$ accuracy $\simeq 200\mu m$, z to within $1-2mm$ and a momentum resolution $\Delta p/p^2 \simeq 1.5 \times 10^{-3}(GeV/c)^{-1}$.

3.5.1 Construction.

The main components of the TPC are the inner and outer field cages, the central membrane and the end plates which seal the chamber and house the wire chambers. The inner and outer cages are cylinders of diameter $0.6m$ and $3.6m$ respectively, and length $4.4m$. The role of the cages is to shape the electric drift field of $11kVm^{-1}$. The central membrane dividing the cylinders is a reinforced $25\mu m$ mylar sheet coated with a conducting graphite paint. It is held at a high negative potential ($-27kV$), and the proportional wire chambers at each end of the cylinder are held at ground. Both the inner and outer cages are covered in electrodes, which are $10.16mm$ wide copper bands with spacings of $1.5mm$. On the outer cage the electrodes are $35\mu m$ thick and the inner electrodes are $19\mu m$ thick. They are affixed to both sides of a $75\mu m$ kapton sheet and are staggered to shield the TPC from the high fields that arise in the mylar foil insulator. The electrodes and insulator are supported by Al structural skins which are separated by Al honeycomb spacers. They are held at varying potentials to ensure that the drift field remains constant and parallel to the z-axis. The electrode rings are connected in series with $1M\Omega$ resistors. Four resistor chains connect the membrane to the last electrode ring held at $-65V$ and each resistor chain draws a maximum current of $60\mu A$.

3.5.2 Wire Chamber Sectors.

As both the bending power of the magnet and the TPC diameter are large, an accurate measurement of momentum can be made. Each end plate of the TPC has 18 sectors on each side which are divided into 6 inner K-type (kind) sectors, and 12 outer sectors of alternating M-type (mann) and W-type (weib) (figure 3.8). The zig-zag geometry of the chambers ensures minimum loss of lever arm when a track crosses an inter-chamber boundary.

Each chamber has three planes of wires - sense wires, gating grid wires and cathode

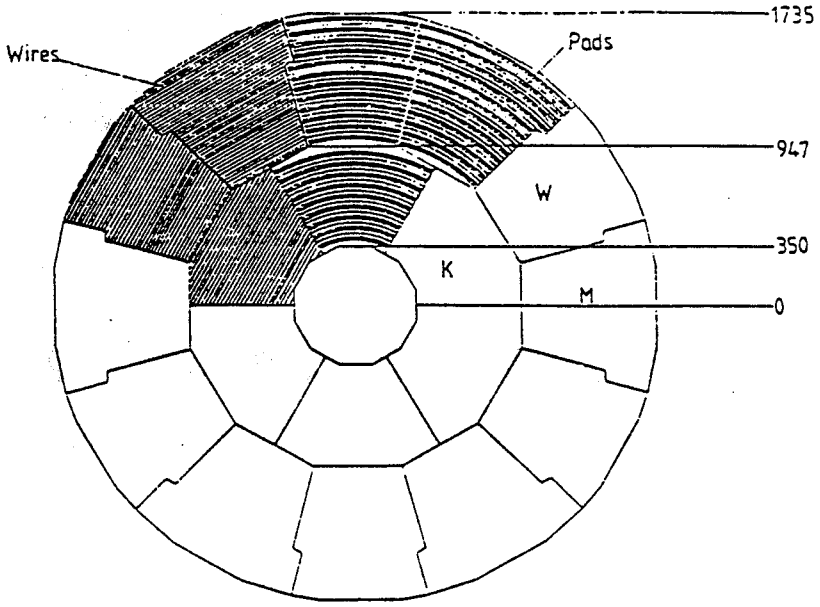

Figure 3.8: Arrangement of Sectors in the TPC End-Plates.

plane wires, which are interleaved with field shaping wires. Cathode pads are situated $4mm$ from the sense wires and a signal is induced on them due to the ionization avalanche around the wires. The pads are $6.2mm \times 30mm$ and have a pitch in azimuth of $6.7mm$, except for the two pads at a sector edge of each row which have a pitch of $3.35mm$. A K-sector has 909 pads in 9 pad rows, a W-sector has 1182 pads in 12 pad rows and an M-sector has 1326 pads in 12 pad rows giving a total of 41004 in the TPC as a whole. The pad rows are spaced with trigger pads which subtend an angle of 15° in ϕ and have a radius of $6.3mm$. The outer five rows are segmented to reduce noise. The trigger pads provide information for the level II trigger. The pad and sector structure is shown in more detail in figure 3.9.

3.5.3 Gas.

The TPC is operated with a gas mixture of $91\%Ar - 9\%CH_4$ (at 1 atm.) which is maintained at $8 - 12mbar$ above atmospheric pressure in the TPC volume. The gas is

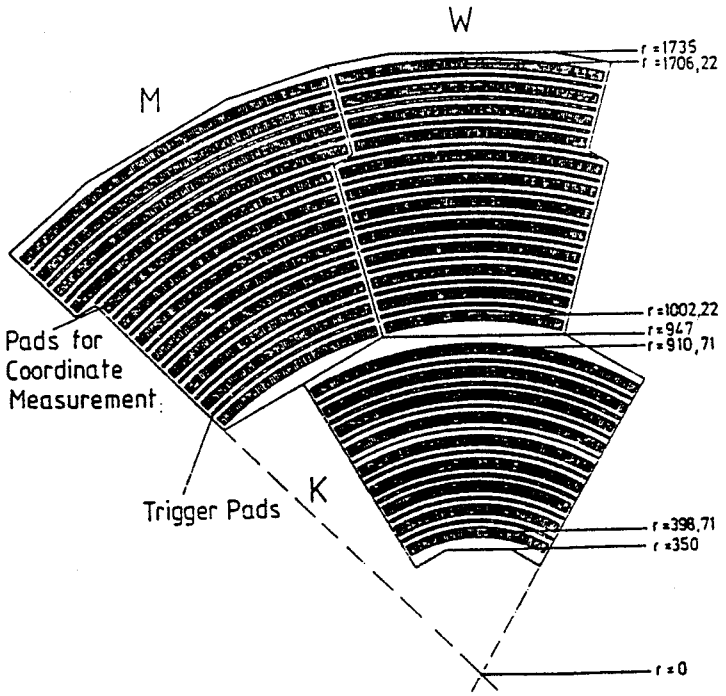

Figure 3.9: A More Detailed View of the TPC End-Plate Sectors, Showing the Arrangement of the Pad Rows.

premixed in a $900m^3$ buffer tank which provides uniformity and long term stability of the mix. The gas is kept at a temperature of $21\pm0.5°C$.

3.5.4 Gating.

The TPC functions in a continuously sensitive mode, but the positive ions produced by the Townsend avalanches near to the sense wires, drift towards the central HV membrane and can cause distortions in the drift field. The gating wire grid is situated between a shielding grid and the drift region, and can be in either an open or closed state.

In the open state, a potential $V_g \simeq -67V$ is placed on the gate wires and the gate is effectively transparent to the drifting charged particles.

In the closed state, potentials of $V_g \pm \Delta V_g$ are placed on alternate grid wires and the resulting dipole field is sufficient to prevent the passage of the charged particles. A

potential of $\Delta V_g \simeq 40V$ is sufficient to stop the slow drifting positive ions. However, due to the magnetic field and their lower mass, $\Delta V_g \simeq 150V$ is required to stop electrons and is the value used.

Switching between the open and closed states is done synchronously with bunch crossings. Approximately $3\mu s$ before a bunch crossing, the gate is opened to allow the ionization electrons in the shower to drift into the amplification region. If the level I trigger is negative the gate is closed, but if positive it remains open for the full $45\mu s$ drift time of electrons in the TPC.

3.5.5 Tracking.

The charged track trajectories are helical and are projected onto the end plate sectors as arcs. The electrons produced by the track ionization drift towards one of the end plates, where they induce an ionization avalanche in one of the wire chamber planes. The z-coordinate is deduced from the drift time of the electrons as the drift velocity of the field is known. The $r - \phi$ coordinate is calculated by interpolating the signals induced on the cathode pads which are precisely located in the sectors. The r-coordinate alone is simply determined from the pads radial position.

3.5.6 Electronics.

The TPC readout electronics are based on FASTBUS with one crate cluster allocated to each module (i.e. 36 clusters in all). The pad and wire signals pass through amplifiers which are grouped in sixteens on preamplifier boards. The preamplifier outputs then go to one of 64 channels in a FASTBUS module known as a Time Projection Digitizer (TPD). The signals at the TPD stage can be buffered for up to four events so that data is not lost while awaiting trigger decisions. Readout of a TPD is controlled by a Time Projection Processor (TPP) of which there are 36 for each end cap (18 pad 18 wire). One TPP controls several TPD's and is responsible for formatting and reading

data from the TPD, reducing wire data, handling data transfer errors and subsequent recovery and calibration testing.

Calibration is remotely controlled by a pulse generator which is installed in each sector. This pulses the field wires, and the signals induced on the sense wires and pads are processed as if generated by ionizing particles. The pulse generator is controlled by a special FASTBUS module (STPC). The calibration programme runs on a TPP which controls the STPC's, and calculates from the calibration response, the necessary settings to equalize and linearise the responses.

The output of the TPP's of each end cap are sent to two Event Builders (EB), whose output in turn passes to another combining EB.

3.5.7 Laser Calibration.

The TPC is calibrated by employing two UV lasers (Nd-yag 266nm). They are situated above the magnet and the polarized beams are guided and deflected over a path of approximately 10m to reach the TPC. The beam is adjusted and steered by precise sensors and computer controlled actuators. Upon reaching the TPC, the beam is split twice to produce three axial rays of equal intensity. Then, by use of four semitransparent mirrors and a pentaprism, simulated ionization tracks are produced at angles (θ) of 18°, 30°, 39°, 67°, 90° and ϕ of 84°, 204°, 324° with an effective origin at the interaction point. Within the chamber the transverse rms width of the beam is typically $\simeq 1mm$. The calibration beams provide data on particle track distortions and are used to calculate the vector drift velocity in the TPC. Systematic effects are also studied during calibration periods.

3.5.8 Resolution And Performance.

The performance of the TPC [24] as a track measuring device was extensively studied with a small test module - the TPC90, which had a diameter of $90cm$ and drift length

of $130cm$ within a magnetic field of $1.2T$. The momentum resolution of the TPC can be expressed as functions of several parameters upon which it depends. The error on p_t of a track with 21 measured coordinates is

$$\frac{\Delta p_t}{p_t} \simeq 10^{-3} p_t \left(\frac{<\sigma>}{150\mu m}\right)\left(\frac{1.5}{B}\right) \oplus 0.003 \tag{3.8}$$

p_t - Transverse momentum.

$<\sigma>$ - Average error on each coordinate.

$\oplus$ - Added in quadrature.

This term is due to multiple scattering of the gas in the chamber.

By measuring the sagitta of the arc of a track, its radius of curvature can be determined. This radius is proportional to the modulus of the momentum component perpendicular to the magnetic field. The resolution is quoted as

$$\frac{\Delta p_t}{p_t} = 0.027 \times p_t \frac{\Delta s}{l^2 B} \tag{3.9}$$

Δs - Resolution of sagitta measurement (mm).

B - Modulus of the magnetic field (T).

l - Length of the projected trajectory.

The spatial resolution obtainable is summarised in table 3.1. Two tracks can become confused if they are close in both $r-\phi$ and z, so a minimum separation of $1.5cm$ in $r-\phi$ or $2cm$ in z is required to resolve the tracks independently. A dE/dx resolution of 4.5% can be achieved with a minimum of 280 wire samples.

$r-\phi$			
$160\mu m$ at 0° pad crossing angle. $400\mu m$ at 10° pad crossing angle.			
z			
θ	90°	45°	20°
per pad row (mm)	0.7	1.7	2.3
per wire (mm)	3.0	2.0	2.0

Table 3.1: The resolution of the TPC in $r-\phi$ and z.

3.6 The Electromagnetic Calorimeter (ECAL).

The ECAL is a lead/wire chamber sampling detector of 22 radiation lengths (X_o) nominal thickness. The calorimeter is highly granular and hermetic, and has a total coverage of 3.9π of solid angle. The high granularity was a well considered feature as it simplifies the identification of electrons within hadronic jets, and facilitates the measurement of the energy and position of electromagnetic showers to a high degree of accuracy. These measurements are made with cathode pads having an area $\simeq 30 \times 30mm^2$ which are connected internally to form projective towers. (i.e. pointing back to the interaction point). There are some 73,728 towers in ECAL which are read out in three depth sections or storeys, corresponding to the first 4, middle 9 and last 9 radiation lengths. Cracks form only 2% of the barrel and 6% of the end cap surface area's, giving rise to an e.m. energy resolution $\Delta E/E = 18\%/\sqrt{E}$.

3.6.1 Construction.

The ECAL consists of a barrel section which is closed with two end cap sections. Each of the two subdetector types is divided into 12 modules which subtend an angle of 30° in ϕ (figure 3.10). The end caps are rotated by 15° with respect to the barrel to avoid

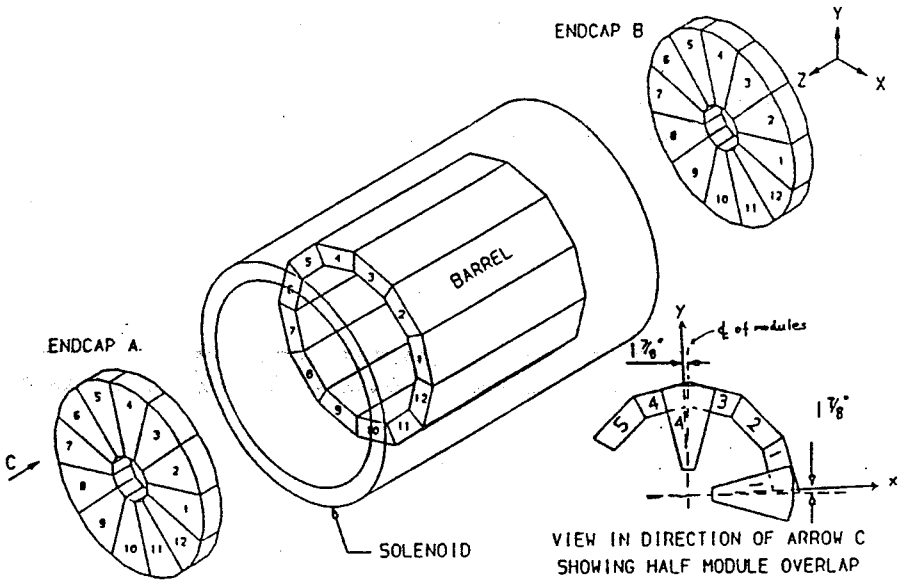

Figure 3.10: The Modular Structure of the ECAL Barrel and End-Caps.

crack continuation and overlap, and the ECAL as a whole is rotated by $-1.875°$ w.r.t. the Hadron Calorimeter for the same purpose.

The barrel has an outer radius of 2.25m, inner radius of 1.85m and overall length of 4.77m. Its twelve 10.4 tonne modules each house 4096 towers in an array of 32×128 (49,152 in total). These are read out in three storeys or channels giving 12,288 channels per module and 147,456 channels in the barrel in total.

The end caps have an outer radius of 2.35m, inner radius of 0.54m and length of 56.25cm. The twelve 2.6 tonne modules in each cap individually contain 1024 towers and hence 3072 channels or storeys. This gives a total for both end caps of 24,577 towers and 73,731 channels or storeys. The end cap modules are also known as 'petals' due to their foliole like geometry.

The e.m. calorimeter is a sandwich of 45 lead/wire proportional chamber layers. (Figure 3.11 illustrates the construction of one layer). The wire chambers are made from open sided aluminium extruded channels of square cross section. A $25\mu m$ diameter

gold plated tungsten wire is centred in each channel, and the open side is sealed with a layer of highly resistive graphite coated mylar. Each chamber has a cross section of $3.2 \times 4.5mm^2$ and the wires are spaced on a $5mm$ pitch. Signals are read out using cathode pads which are positioned on the opposite side of the mylar to the extrusions, and a lead sheet placed before the extrusions completes one read out layer. Particles passing through the lead sheets induce e.m. showers, which in turn result in ionization in the detector gas. This is subsequently amplified in avalanches around the wires. The signals are read out capacitively through the pads which connect through subsequent layers to form the towers. The three storeys of each tower are divided as follows

- Stack 1 - 1st. 10 layers $\simeq 4X_o$.
- Stack 2 - 2nd. 23 layers $\simeq 9X_o$.
- Stack 3 - 3rd. 12 layers $\simeq 9X_o$.

Stacks 1 and 2 are constructed with lead sheets of $2mm$ thickness and one radiation length corresponds to $2.0 - 2.4cm$. Stack three uses lead of $4mm$ thickness and a radiation length is typically $1.3 - 1.4cm$.
Due to their differing geometries, the barrel and end caps do vary as described below. The barrel design was optimised to

1. Keep the spacing of the anode wires from the readout pads and extrusion walls constant. This is required to ensure uniform response of the pads.
2. To be leak free for the gas. (or as near as possible).
3. To minimize dead areas between the modules.

Each anode wire plane has between 193 and 233 wires running parallel to the z-axis and magnetic field. The wire lengths are all $4630mm$ and they are strung with a tension of $65g$. Each wire is supported every $450mm$ by a plastic spacer, which is varied in position from layer to layer to avoid a build up of dead zones due to plastic.

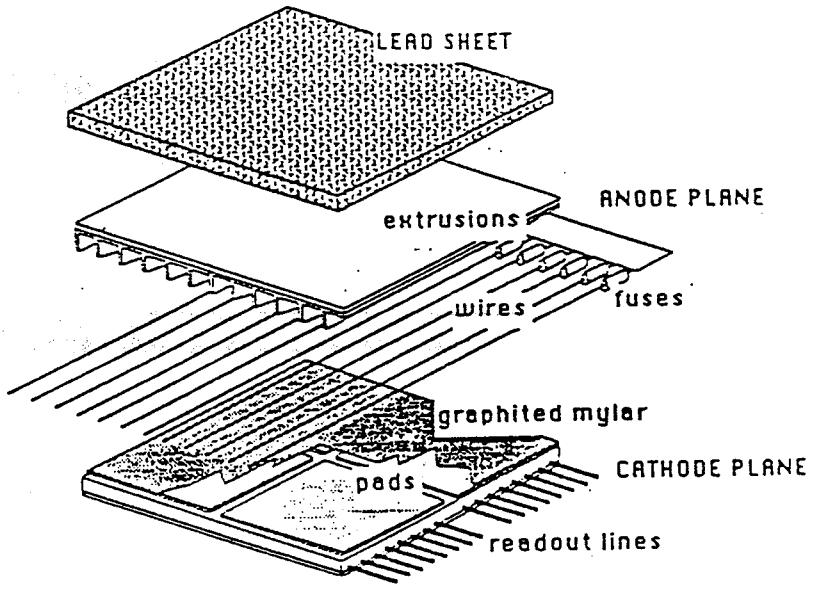

Figure 3.11: A Single Wire Chamber Layer of the ECAL.

The end caps, in addition to incorporating points 1-3 above have 210 wires per anode plane, which run parallel to the right hand side of a petal as viewed from the front with the narrow end uppermost. The wires range in length from $80 - 1700mm$ and a plastic spacer is inserted every $350mm$.

3.6.2 Gas.

An $80\%Xe - 20\%CO_2$ mixture is used within the ECAL. This is a high Z gas which was chosen to minimise the path length fluctuations to the energy resolution (due to $\delta - rays$ perpendicular to the shower direction). The gas gain depends upon the mixture, absence of impurities and gas density. The gas system maintains the xenon content at $80\pm1\%$ and purifies the recycled gas. The pressure is held at $60mbar$ above atmospheric pressure and the temperature is maintained at $20\pm0.5°C$. Pressure and temperature are monitored for each module. Also, each module has a small single wire chamber containing a Fe^{55} source. The charge collected on the wire due to the $6KeV$

X-rays is used to monitor the gas gain.

3.6.3 Electronics.

The ECAL electronics has to read out 221,184 pad channels and 1620 wire channels. To minimise cabling and front end electronics the pad channels are multiplexed by 32 and again by 8 before the ADC. However, each wire plane is read as a single channel.

Pads.

The pad towers have a capacitance $\simeq 2nF$ and are directly connected to a BIFET operational amplifier, which integrates the charge on a $200pF$ feedback capacitor. The signal is then relayed to a sample and hold circuit and a 32 channel multiplexer. The unit sums the 32 channels for trigger purposes and when the sample and hold circuit completes the charge integration, the 32 charges are sent in sequence to two cable drivers with gains of 1X and 8X. Therefore, a dynamic range of 2^{16} is obtained from the 12-bit ADC's connected to each multiplexed readout channel.

Wires.

The wire planes have a higher capacitance $\simeq 10nF$ and far fewer channels to read, so a design with better noise performance is employed. In this case the signals pass to a common base transistor then to a differential cable driver. After transference down a $30m$ long cable the signal is amplified and integrated. Again, two outputs with gains 1X and 8X are used. The channels are also multiplexed into groups of 32 but the sums of odd or even planes are formed for triggering.

ADC.

Each twisted pair cable carries the charge from the 32 channels sequentially to one input of an 8 channel multiplexer. The signal is then fed to a 12-bit successive approximation

ADC which sequentially digitizes the signals from each of its 256 inputs (8×32). The total operation time is $\simeq 3.7ms$ including settling time between conversions. Twelve ADC chips are mounted on a single width FASTBUS module. After all conversions the results for each channel are compared with thresholds preloaded in its memory for zero suppression. The unit then generates the address of each fired channel and the corresponding pulse height. The complete sequence of sampling, multiplexing, conversion and resetting the front end is controlled by a microprogrammed sequencer contained in the FASTBUS module. This is connected to the front end boxes and ADC modules.

Tests and Calibration.

Each wire chain is tested and calibrated by a test pulse applied at the detector level. For the pad chains, the test pulses are only applied after the front end multiplexer due to the large number of channels involved. For test purposes it is possible to inject pulses on each wire plane and to measure the response of each pad channel. This facilitates a check of the connections between the pads and amplifiers and the operation of the amplifiers. It is not possible however to calibrate a complete pad chain like this as the ratio of wire/pad capacitances varies over a module due to mechanical non-uniformities. But, in the barrel it can be used to measure the distance between pads and wires, and hence deduce the wire position within a cell. The wire gain can thus be determined and module gain maps of pads and wires produced. This is not possible in the end caps due to stray capacitances.

Digital Readout.

Readout Controllers - After zero suppression in the ADC, the data are read out by a Read Out Controller (ROC). A ROC is a *FASTBUS* master and each reads 17 barrel or 27 end cap ADC's. Additionally a ROC performs pedestal subtraction

and gain correction before recording and formating the data to be sent to the event builder (EB).

Event Builders - There is one EB for the whole ECAL which takes data from the ROC's and records it. The data is then sent to the main ALEPH EB and the ECAL VAX for monitoring.

Error Handling - Errors are detected by the ROC's (e.g. *FASTBUS* in the ROC crate, protocol in trigger signals) and are reported to the EB. The EB reports all errors to the DAQ VAX.

Precision - The total energy per module ($\Sigma 45$ wire planes) is measured to $\pm 10 MeV$ which provides the possibility of triggering at the $200 MeV$ level. For the pads $\simeq 100$ channels are added to encompass a typical shower. The sum of 96 channels is measured typically to $\pm 100 MeV$.

3.6.4 Performance.

Spatial and Angular Resolution.

The granularity of the modules varies between $17 \times 17 mrad^2$ at $\theta = 90°$ in the barrel to $9 \times 10 mrad^2$ at $\theta = 40°$ in the end caps. The centre of gravity of a shower is reconstructed from the four leading towers.

$$\theta = \frac{\Sigma_{i=1}^{4} E_i \theta_i}{\Sigma_{i=1}^{4} E_i} \tag{3.10}$$

$$\phi = \frac{\Sigma_{i=1}^{4} E_i \phi_i}{\Sigma_{i=1}^{4} E_i} \tag{3.11}$$

E_i - energy deposited in tower i.

θ_i, ϕ_i - centre coordinates of the tower i.

The centre of gravity coordinates are corrected with periodic functions of θ_0 and ϕ_0.

$$\theta_c = \theta + C_1 \sin[2\pi\theta_0 + d_1 \sin 2\pi\theta_0] \tag{3.12}$$

$$\phi_c = \phi + C_2 \sin[2\pi\phi_0 + d_2 \sin 2\pi\phi_0] \tag{3.13}$$

θ_0, ϕ_0 - hit coordinates of incident particles.

C_i, d_i - obtained by fits to e^- test data at various θ, ϕ, E and independent of θ, ϕ, E.

$C = C_1 = C_2 = (9.3 \pm 0.7) \times 10^{-2}$ tower units.

$d = d_1 = d_2 = (0.45 \pm 0.15)$ radians.

The standard variations of the Gaussian fits are given by

$$\Delta\theta = \Delta\phi = a + b/\sqrt{E} \tag{3.14}$$

$a = (2.0 \pm 0.2) \pm 10^{-2}$

$b = (17.6 \pm 0.9) \pm 10^{-2} GeV^{1/2}$ both in tower units.

For electrons up to $50GeV$ the angular resolution for e.m. showers is below $1 \times 1 mrad^2$ for the whole detector.

Energy Resolution.

The energy resolution was measured with test beams of 10, 25 and 50 GeV for the barrel modules, and energies in the range 5-70GeV for the end caps. An operating voltage of $1340V$ was used. The energy resolution obeys the law

$$\frac{\Delta E}{E} = a + \frac{b}{\sqrt{E}} \tag{3.15}$$

where for the barrel the constant terms for the wires are

$a = (0.3 \pm 0.1)\%$

$b = (16.5 \pm 0.3)\% GeV^{-1/2}$

and for the end caps the data for the wires and pads respectively gives

$a = 0.45\%$

$b = (17.0 \pm 0.5)\% GeV^{-1/2}$

$a = 0.33\%$

$b = (19.2 \pm 0.5)\% GeV^{-1/2}$

Linearity Of Response.

The response of the ECAL to incident electrons increases almost linearly with the electron energy in the range $10 - 70 GeV$. Small deviations from the linearity can be parameterized by

$$\frac{E_m}{E} = 1 - \alpha E \tag{3.16}$$

E_m - energy response.

$\alpha = \alpha_1 + \alpha_2$ - observed non linearity.

α_1 - saturation effect.

α_2 - leakage effect.

Test measurements give

$$\alpha = (9.0\pm0.7) \times 10^{-4} GeV^{-1} \ \theta = 50° - 90° \text{ at nominal voltage } 1340V.$$

$$\alpha_1 = (7.8\pm0.6) \times 10^{-4} GeV^{-1}$$

α_1 is assumed linear with gas gain and was determined using different gains and angles. The gas gain G varies with high voltage V according to $G \propto V^{16.2\pm0.1}$.

3.6.5 $e - \pi$ Separation.

This is achieved by employing both the calorimeter segmentation and several cuts. By summing the energy of the 4-towers E_4 adjacent to the particle impact point, then for a particle with momentum p the cut

$$E_4/p \geq 0.75 \tag{3.17}$$

ensures that only 0.8±0.2% of a 10GeV pion sample can fake electrons, yet still leaves an electron efficiency of 99%. Additional cuts are based on longitudinal shower shape and track hit coordinates. The final pion contamination for an electron efficiency of $> 95\%$ is

$$\varepsilon_\pi = (1.1\pm0.5) \times 10^{-3} \text{ at } 10\text{GeV}.$$

$$\varepsilon_\pi < 3 \times 10^{-3} \text{ at } 95\% \text{ confidence level at } 5\text{GeV}.$$

Test beam studies have been used to reconstruct energy independent estimators of the quality of electron identification based upon the compactness ratio E_4/p or R_2, and the longitudinal shower shape R_3. These two estimators are normally distributed, dimensionless and centred on zero. R_2 measures the deviation of the compactness of the shower from the expected transverse shape reconstructed in the calorimeter stories.

$$R_2 = \frac{(E_4/p)_{measured} - (E_4/p)_{expected}}{\delta(E_4/p)} \tag{3.18}$$

R_3 is similar but for the longitudinal shower shape. It is formed from the first and second moments of the longitudinal energy deposition measured in the three stacks.

3.7 The Magnet.

The ALEPH magnet consists of two main components - the superconducting solenoid and a fully calorimeterized iron return yoke. A nominal operating current of $5000A$ provides a homogeneous $1.5T$ field parallel to the beam axis. This provides a uniformity such that the sagitta distortions in the TPC are $\leq 0.2mm$. Also, an axial symmetry is maintained to avoid ϕ components.

3.7.1 The Iron Yoke.

The iron return yoke has a barrel section and two end cap pieces, and has four main functions.

- Shaping of the longitudinal magnetic field.
- To act as a sampling medium for the Hadron Calorimeter (HCAL).
- To provide muon identification as muons will penetrate the iron.
- Mechanical support for many of the other subdetectors.

The barrel is a hollow dodecagonal cylinder $7.24m$ long, $9.37m$ wide with a mass of 1680 tonnes. It accommodates 22 layers of $50mm$ thick steel plates with an outer plate of $100mm$. The plates themselves are separated by a distance of $22mm$ to house the HCAL streamer tubes. The end caps are also dodecagonal cylinders of length $1.18m$, width $8.7m$, and mass 450 tonnes each. In the nominal field the end caps are pushed against the barrel, by the field, with a force $\simeq$4000 tonnes. This force gives rise to a maximum distortion of $\leq 3mm$ in the steel plates.

3.7.2 The Solenoid.

The solenoid is a cylinder of volume $123m^3$. It is suspended at both ends from the barrel of the iron yoke, and itself supports both ECAL and TPC with a combined mass of 130 tonnes. The solenoid is encased in a vacuum chamber and is a continuous uniform winding of 1532 turns over its full length of $6.35m$. There are two compensating coils at the ends of the main solenoid, each of length $40cm$ with a winding length of $188mm$ in 45 turns.

3.7.3 Performance And Testing.

The overall field requirement can be expressed as a tolerance of the integral of the radial field component B_r, along the z-axis in the whole volume of the TPC ($4.4m$ long). This is given by

$$\int_0^{2200} (B_r/B_z)dz < 2mm. \tag{3.19}$$

B_z - main field component.

The complete magnet was assembled on the surface during the autumn of 1987. The field inside the coil was measured with two sets of moveable Hall plates at 17,500 points within the solenoid. (20 radial positions $r = 32.6 - 232.5cm$, 25 axial positions $z = -2.6 - +2.6m$ and 35 points in ϕ). The Hall probes were oriented to measure the main field component B_z, the radial component B_r and the azimuthal component B_ϕ. The test gear was aligned with a precision of $0.5mm$ in r and $0.3mrad$ in angle, which produced axial and azimuthal positioning accuracies of $\delta z = 0.2mm$ and $\delta\phi = 1mrad$. This led to an overall sensitivity of $\delta B = 0.1G$ for the Hall plate measurement.

Optimization of B_z is achieved by adjusting the current in the compensating coils, until its value along the z-axis is constant to a degree such that $\Delta B_z/B_z \leq 0.2\%$. The

main field component B_z is a function of the azimuthal position, and variations up to $\delta B_z/B_z = 5 \times 10^{-4}$ at $r = 1.7m$ occur due to differences of magnetic reluctance in the end caps, and imperfections in the solenoid construction.

3.8 Hadron Calorimeter and Muon Detector (HCAL & MUON).

The main support for all of the other ALEPH subdetectors is a large iron construction which serves a dual role. It acts as both the absorbing medium of HCAL and as the return yoke for the magnet. The iron is interspersed with layers of limited streamer tubes which provide the active part of HCAL. Beyond the HCAL are two further double layers of streamer tubes which provide both the position and direction of muons penetrating the iron.

3.8.1 Streamer Tubes.

The streamer tubes (figure 3.12) are constructed from a PVC plastic base, from which projects nine orthogonal fins, thus forming eight contiguous, open sided square cross sectional channels or cells. The tubes are $\simeq 7m$ long, have a wall thickness of $1mm$ and an internal cross section of $9 \times 9mm^2$. The inner walls of the channels are graphite coated and a $100\mu m$ diameter anode wire running the whole length of the channel is centred within each. The wires are supported every $0.5m$ by plastic spacers. Aluminium strips running parallel to the wires are positioned beneath the base of the channels. The strips are $0.4cm$ wide, are on a pitch of $1.0cm$, and are used to obtain standard logic signals whenever a cell fires. The open faces of the channels are covered by cathode pads.

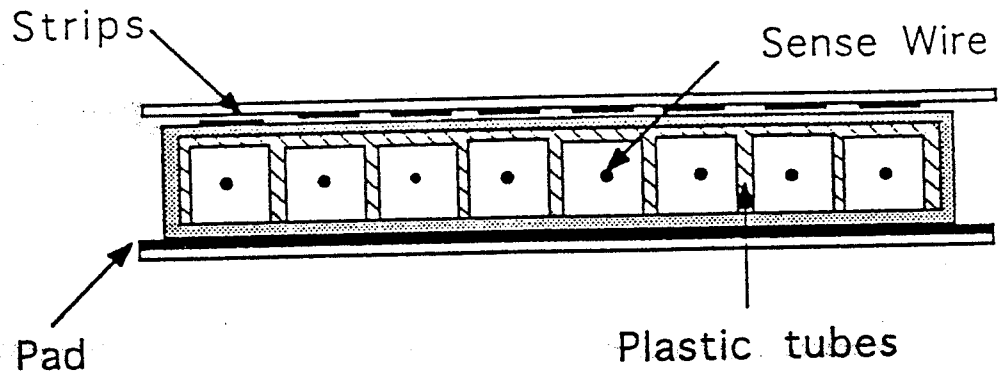

Figure 3.12: End View Showing the Construction of a HCAL Streamer Tube Unit.

3.8.2 Construction.

The HCAL consists of 22 × 5cm thick iron slabs with 22mm spacing to house the streamer tube units. This is supplemented by an outer slab of 10cm thickness between the HCAL and muon chambers. This provides a total iron thickness of 1.2m corresponding to 7.16 interaction lengths for hadrons. The first layer of tubes sits in front of the iron and is held in place by a 5mm thick aluminium sheet. Cathode pads from different tube layers are connected to form projective towers pointing back to the interaction point. Due to the immense mass of the subdetector, several support members have to be included which results in a loss of detector space. However, this loss is restricted to 3-4% of azimuthal cover in the barrel and 6% of the area of the end caps.

The Barrel.

The barrel is dodecagonal with a radius of 4.68m and overall length of 7.24m. It is subdivided into 12 modules, each of mass 70 tons, which themselves consist of two mirror image halves. The streamer tubes run parallel to the z-axis and there are 2688 towers fully contained in the barrel with 768 in the end cap overlap region. additionally the barrel houses a total of 48,384 strips and wires. The tube/iron layer structure can

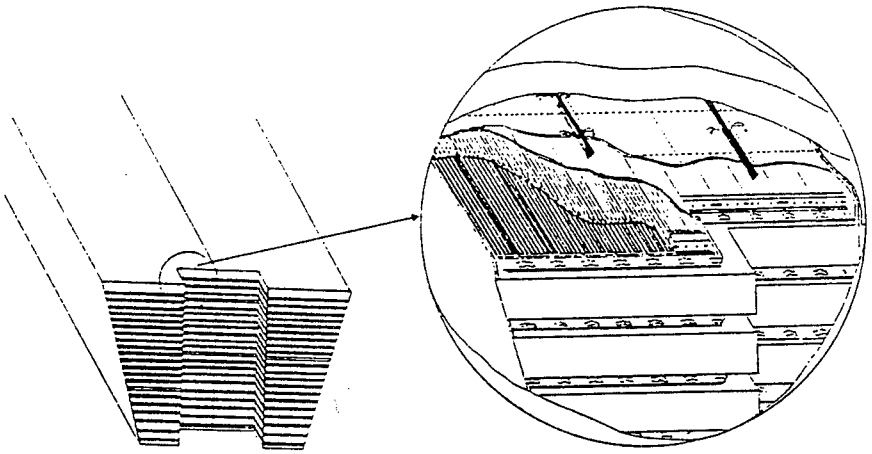

Figure 3.13: A HCAL Barrel Module With Detailed View of the Positioning of the Streamer Tubes Between the Iron.

be seen in figure 3.13.

The End Caps.

Each end cap consists of six petals with a radius of $4.35m$ and a mass of 75 tons per petal. The petals differ from the barrel in that they only have 16 layers of tubes at the broad end where they meet the barrel. The tubes are oriented horizontally in the four petals with an edge in the horizontal plane, and at 60° to the horizontal in the remaining two. There are 1332 towers fully contained in the end caps with 768 overlapping. This corresponds to a total of 71,040 strips and wires.

The Muon Chambers.

MUON consists of two double layers of tubes known as the inner and outer chambers. The tubes within one double layer are perpendicular to each other (figure 3.14). The layout of MUON is virtually identical to the HCAL barrel and end caps, with the addition of middle angle chambers to cover the overlap regions. Each double layer is offset by half a pitch to ensure good spatial resolution, and the layers are separated by

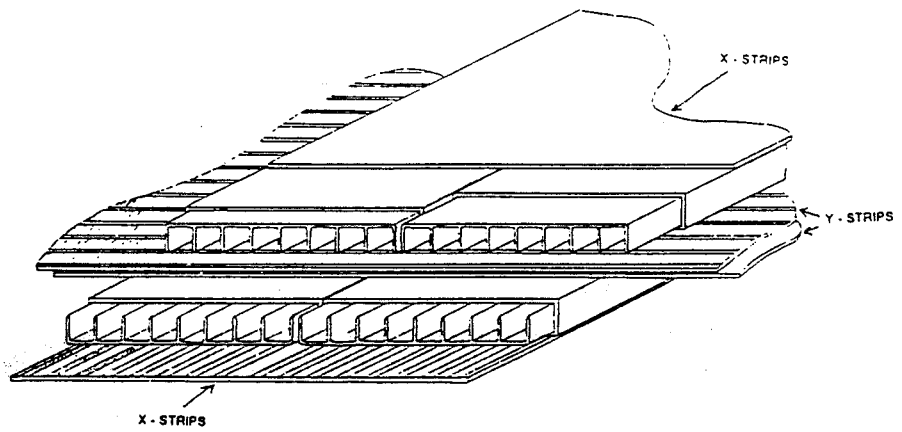

Figure 3.14: The Double Layer Arrangement of Streamer Tubes in the MUON Chambers.

$0.5m$ in the barrel and middle angle chambers and $0.4m$ in the end caps. The muon chambers are simply used as tracking devices giving two coordinates from each double layer's strip electrodes which run both parallel and perpendicular to the wires. The parallel strips are $0.4cm$ wide with pitch of $1.0cm$ and the perpendicular strips are $1.0cm$ wide with pitch of $1.2cm$.

3.8.3 Streamer Tube Operation.

Streamer tubes are similar in construction to proportional counters but operate at a higher voltage of $4250V$ in limited streamer mode. An incident charged particle induces a local avalanche around an anode wire. The size of the avalanche is however independent of the amount of primary ionization produced by the particle. Signals are induced on the cathode pads, and twisted pair cables, one of which is earthed carry the signals away.

3.8.4 Gas.

The standard mixture for streamer tubes is $30\%Ar - 70\%isobutane$ but this is deemed unsafe for underground use, so a $13\%Ar - 57\%CO_2 - 30\%isobutane$ mix is employed. This provides stable, reproducible operation, with fully efficient streamer formation and falls within the safety criteria. The total gas volume in HCAL+MUON is $54m^3$ and is exchanged every 2-3 days by the gas flow system.

3.8.5 Electronics and Readout.

There are three signals derived from the HCAL.

pads - energy deposited in the calorimeter.

wires - energy deposited in a single plane.

strips - shows the pattern of fired tubes in an event.

The formation of a streamer avalanche in a tube induces a positive pulse on a pad facing the open side of the tube plane. The signals from the pads in the same projective tower are summed electronically in mixer boxes (4 per module). The summed signals are then transfered to *FASTBUS* ADC units. At the input to an ADC, the range is automatically selected as either $200pC$ or $1600pC$ full scale. Typical fluctuations are $\simeq 3pC$ compared with a $280pC$ signal from a muon at normal incidence. A streamer also induces a positive pulse signal on a strip electrode situated on the opposite side of the tube plane to the pads. The pulse is converted to a $1\mu s$ long digital signal by a hybrid amplifier discriminator. The digital signal is then latched into 1-bit of a 256-bit shift register, then 24 shift registers are sent in parallel to an ALEPH Strip Readout Scanner (ASTROS), housed in a *FASTBUS* rack. The ASTROS modules are controlled by a Hadron Calorimeter Processor (HCP). The third signal induced by the formation of the streamer avalanche is on the wire itself and is read via capacitative coupling.

Wires from eight tubes in a plane are connected in parallel, so it is not possible to obtain individual wire signals.

3.8.6 DAQ.

The system consists of four coupled pairs of *FASTBUS* crates with two for the barrel and one for each end cap. There is also a *FASTBUS* crate housing the main HCAL DAQ control units, event builders and trigger supervisors. Individual pairs of crates are controlled by an HCP.

3.8.7 Performance and Resolution.

Monte Carlo estimates for typical muon misidentification probability at $5GeV$ for 95% efficiency are

0.7% to mistake a π for a μ.

1.6% to mistake a K for a μ.

The energy resolution is typically

$$\frac{\sigma}{E} = \frac{0.84}{\sqrt{E}} \tag{3.20}$$

with a spatial resolution accurate to $\Delta = 0.35cm$.

3.9 Luminosity Monitors.

3.9.1 Design Considerations.

The luminosity is determined by the rate of Bhabha events at small scattering angles, where the interference between γ and Z^0 is almost negligible and the cross section is well defined by QED. The differential cross section for small scattering angles θ for electrons with energy E to the lowest order in α is

	SATR	LCAL	SATR+LCAL	BCAL
Polar angle acceptance limits (mrad)	40-90	55-155	55-90	5-10
Azimuth angle acceptance interval (deg)	360	330	330	220
Cross section near Z^0 (μb)	0.063	0.033	0.025	0.67

Table 3.2: Acceptance Parameters Of The Luminosity Monitors.

$$\frac{d\sigma}{d\Omega} = \frac{4\alpha^2}{E^2}\frac{(\hbar c)^2}{\theta^4} \tag{3.21}$$

A precise measure of the polar angle is required due to the strong dependence of the cross section on the $1/\theta^4$ term. The energy of the e^+e^- pair needs to be accurately determined for their identification and background rejection. These measurements are made in the Luminosity Calorimeter (LCAL) and Small Angle Tracker (SATR), jointly known as the luminosity monitor. To provide a fast relative luminosity measurement, the Bhabha Calorimeter (BCAL) is used at very small angles. Parameters of all of the luminosity monitors are summarised in table 3.2.

3.9.2 Small Angle Tracking Device (SATR).

The tracker consists of two main sections situated at $z = \pm 2455mm$ from the interaction point. It fits around the beam pipe and has an inner radius of $92mm$ and outer radius of $300mm$. Each half of the SATR is constructed from nine layers of drift tube chambers. Adjacent layers are rotated by 15° w.r.t. each other to minimize dead zones. Additionally each layer is subdivided into 8 sectors each subtending an angle of 45° and housing 14 drift tubes each (112 per layer - 2016 total). This is shown in figure 3.15. The individual drift cells are brass tubes with a square cross section of $9.95 \times 9.95mm^2$ and wall thickness of $300\mu m$. A $25\mu m$ diameter anode wire runs along the axis of the tubes which range in length from $76.8 - 192.7mm$.

Gas.

A $90\%Ar - 10\%CO_2$ with 1% Isopropanol admixture is used.

Electronics and Readout.

The anode wire signals are amplified and are then digitized by a 10-bit TDC with a precision of $1ns$. Due to lack of space, some wire pairs are OR'ed so the 2016 anode wires are read out via 1152 channels, each having its own TDC. The digitized data is then relayed to buffer cards before being sent to the event builder.

Resolution.

The spatial resolution of a single drift cell is $320\pm20\mu m$ which gives an r.m.s. error of the tracks polar coordinate $\sigma_\theta = 0.08mrad$ for the whole chamber. The azimuthal resolution of the entire chamber $\simeq 13mrad$ which corresponds to an r.m.s. error of the fitted track position of $200\mu m$ in the radial direction, and $2mm$ in azimuth. The overall reconstruction efficiency of SATR is 99%.

3.9.3 Luminosity Calorimeter (LCAL).

At luminosities of $10^{31}cm^{-2}s^{-1}$ LCAL measures events with a count rate $\simeq 0.3Hz$. The LCAL is a lead/wire sampling device which is very similar to ECAL both mechanically and electronically. It is situated around the beam pipe inside the ECAL end caps, and has an inner radius of $100mm$ and outer radius of $520mm$. The first sampling layers are positioned at $z = \pm 2668mm$ and the overall thickness of the 38 sampling layers is $425mm$. Energy and position are determined with cathode pads which range in size from $28.6 \times 28.6 - 31.8 \times 31.8mm^2$. The pads are connected to form projective towers and each tower is read out in three depth sections or storeys as is the ECAL. Each wire layer houses 112 gold plated tungsten wires of $25\mu m$ diameter on a $5mm$ pitch. The wires run parallel to the ALEPH y-axis. Each sampling layer is built up from lead

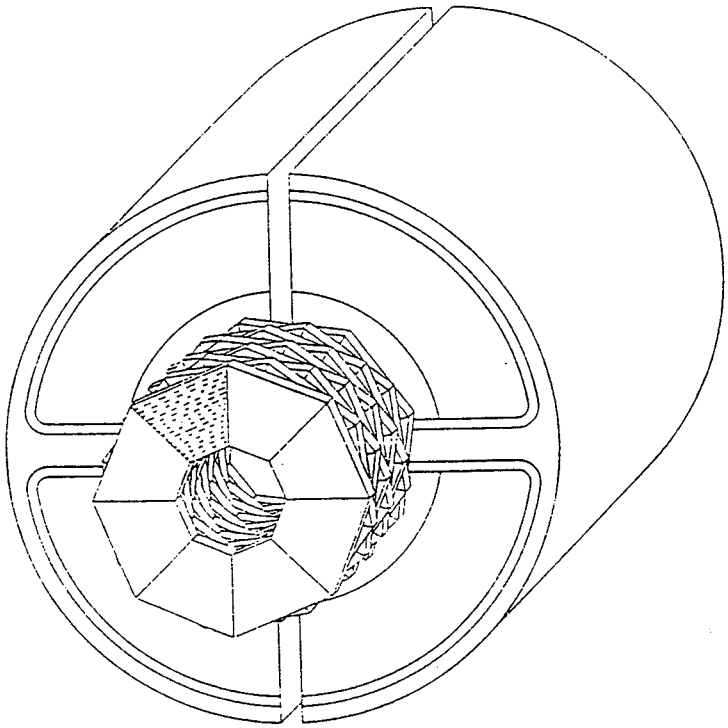

Figure 3.15: Half of the SATR in Position in Front of LCAL.

sheets, plastic proportional tubes, graphite and $1.0mm$ thick printed circuit boards. The nominal thickness of the device is 24.6 radiation lengths (X_0), which is divided into the three stacks as

1st. storey - 9 sampling layers of $4.77X_0$

2nd. storey - 20 sampling layers of $10.60X_0$

3rd. storey - 9 sampling layers of $9.25X_0$

The lead sheets are $2.8mm$ thick in stories 1 and 2 and $5.6mm$ thick in storey 3. A $40mm$ thick aluminium sheet sits in front of the whole detector.

Gas.

An $80\%Xe - 20\%CO_2$ mixture is used which is supplied by the ECAL gas system. The gas circulates in a closed loop within each module at constant volume and pressure but is maintained at $60mbar$ above atmospheric.

Electronics and Readout.

A total of 4608 cathode channels (from 1536 towers) and 152 wire plane signals are read out. They are multiplexed at two levels.

i) at the front end amplifiers which are on the calorimeter modules, where summing amplifiers sequentially read out 32 front end sample and hold amplifiers.

ii) at the FASTBUS ADC converters (MUX-ADC) where 8 input signals are combined.

A double gain system of $1\times$ and $8\times$ is applied to the signals from the front end summing amplifiers. This provides a 16-bit dynamic range from the 12-bit successive approximation ADC's. Zero suppression is performed at 10 counts at the MUX-ADC level and calibration constant corrections are performed by the readout controller (ALEPH EB).

Resolution.

The energy and position resolution of the LCAL is summarized below.

$$\sigma_E = 0.014E + \frac{0.20}{\sqrt{E}} \tag{3.22}$$

$$\sigma_x = \sigma_y = 1.4mm \tag{3.23}$$

3.9.4 Small Angle Luminosity Monitor (SALM/BCAL).

The main objective of the SALM or Bhabha calorimeter is the on-line monitoring of the relative LEP luminosity using a system of two pairs of calorimeters. These very small angle events are measured at a rate of $5Hz$ at luminosities of $10^{31}cm^{-2}s^{-1}$. Due to the defocussing effect of the superconducting quadrapoles and beam pipe elements, the effective production angle in the $x-z$ plane is $5{\leq}\theta_{prod}{\leq}12mrad$. This equates to

an acceptance of less than $2cm$ in the x-direction. Each half of the BCAL consists of two calorimeter modules (4 in total) on either side of the beam pipe at $z = \pm 7700mm$. Each module is a rectangular box of dimension $3 \times 5 \times 14cm$ and is constructed from 10 sampling planes. The planes are consecutive layers of tungsten converter sheets and layers of plastic scintillator. The scintillator is $3mm$ thick and is read out in pairs by $1cm$ diameter photomultiplier tubes. The first tungsten layer is $4X_0$ thick and the next nine are $2X_0$ thick. A final tungsten sheet of $6X_0$ thickness sit behind the modules. The first and last sheets are to protect the calorimeter modules from synchrotron radiation. A plane of vertical silicon strips is situated behind the first $8X_0$. The plane consists of 40 strips of length $5cm$, $300\mu m$ thickness on a $0.5mm$ pitch.

The readout consists of 20 p-m tube pulse heights and 160 silicon strip signals. A position resolution commensurate with the strip pitch is achieved.

Chapter 4

Data Acquisition and Event Reconstruction.

4.1 Introduction.

Data for input to physics analysis can be derived from two sources. Real e^+e^- events from the ALEPH experiment or Monte Carlo simulated data. Figure 4.1 shows the flow of data from either source to the analysis stage.

Monte Carlo events are produced with specific event generating programmes grouped under the heading KINGAL, (Kinematic Generator for ALEPH), which create the 4-vectors of the particles within an event. Next the data passes through the GALEPH programme (Generator for ALEPH) where the 4-vectors are converted to the detector output that such particles would produce. Here the real data and MC data paths merge and are processed by the JULIA [25] reconstruction programme (Job to Unveil LEP Interactions at ALEPH).

Events from ALEPH are both large and complex with the detector providing up to 700,000 channels of data per event. After digitizing this corresponds typically to $500 Mbytes$ of raw data. The bunch crossing rate of $45 kHz$ ($22 \mu s$) adds to the com-

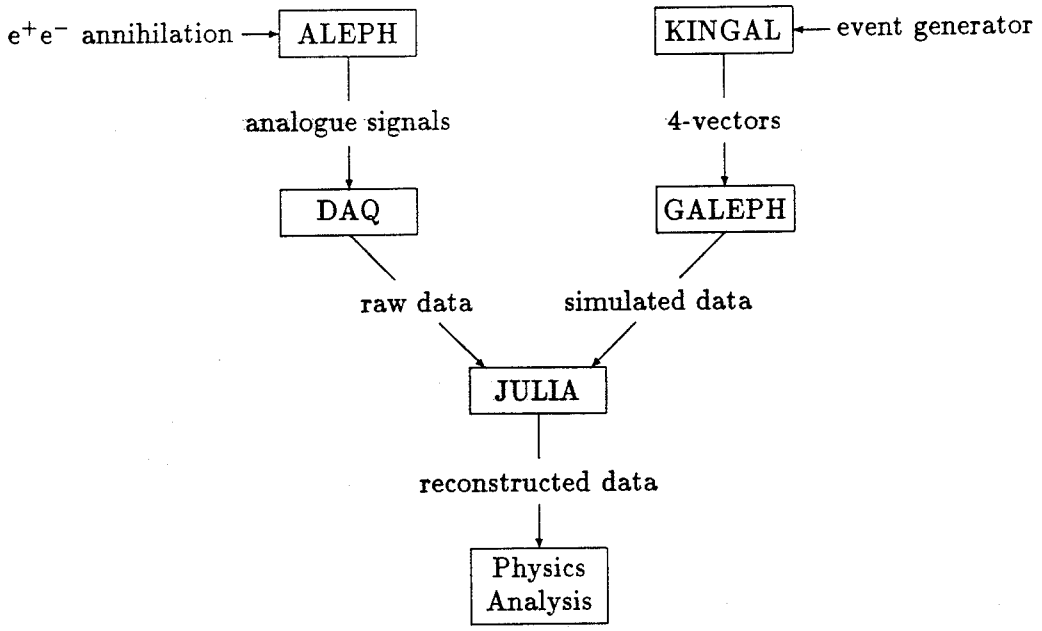

Figure 4.1: Data Flow in the ALEPH Experiment.

plexity. It is the job of the Data Acquisition (DAQ) system [26,27,28] to reduce this rate to below $100 kbytes/sec$; a rate which can be reasonably written to tape. At the design luminosity the interaction rate at the Z^0 pole is typically $\simeq 1Hz$. Hence, no particular events have to be selected. Only background events have to be removed. They are mainly due to beam gas interactions and off momentum particles striking the beam pipe components.

4.2 The Trigger.

Although strictly classed as a sub-detector component, the ALEPH trigger system [20,21,26] which is in fact a sub-component of the DAQ system, is best described in this chapter as it initiates the data collection process. The system was designed to accept all genuine e^+e^- interactions while rejecting all background events to an acceptable level. It is particularly sensitive to single particle or single jet configurations within events rather than events as a whole. This provides a greater scope for observing new and interesting physics events.

Several features had to be considered when designing the trigger, which necessitated as flexible a scheme as possible.

i) - Backgrounds were not well understood before start up.

ii) - Backgrounds can be unstable during fills.

iii) - Backgrounds may change with parameters in the LEP storage ring.

iv) - Signals from different detector components require many triggers to cover all possible event types.

More specific constraints which affected the design were

i) - The bunch crossing rate of $45kHz$ ($22\mu s$ spacing).

ii) - The physics event rate of $\simeq 1Hz$ at the design luminosity.

iii) - TPC gating rate sets the maximum trigger rate to $500Hz$.

iv) - ECAL requires $17\mu s$ to discharge and recycle itself.

v) - A maximum recording rate of $\simeq 2Hz$.

The final design which was adopted is composed of three levels. The first two are specially built hardware devices which look for signals in coarse segments of HCAL, ECAL, LCAL, ITC and TPC. The third is a software analysis based on the full detector readout.

4.2.1 Level 1.

Level 1 provides a fast decision within $5\mu s$ of the bunch crossing, and is designed to reduce the event rate to $\simeq$ few hundred hertz. There is an upper limit of $500Hz$ set by the gating rate of the TPC. Four detector elements (ITC,TPC,ECAL,HCAL) are employed by Level 1, each of which covers approximately 4π of solid angle. The sub-detectors are sub-divided into 72 angular segments in θ and ϕ which resemble their

modular geometries. The barrel has 12 sections subtending 30° in ϕ, and the end caps each have 6 sections of 60° in ϕ. More complex sectioning occurs in the θ (polar) range. The decision is based on ITC and TPC track candidates, energy in a trigger segment, the total energy in the barrel, either end cap or the entire detector. ECAL and HCAL provide both wire and pad (tower) data and the signals are grouped into 60 logical trigger segments. The LCAL tower signals are grouped into 24 segments and provide triggers on forward Bhabha events to monitor the collision rate. The most frequent types of physics event trigger are Bhabha, single muon, single electron, single jet, total energy or single photon. The single photon logic uses the LCAL for vetoing purposes.

Electronics.

All of the analog signals from the individual cells are summed to produce the segment signals. Each summed value passes through four discriminators which yield four YES/NO decisions per segment. The resulting digital signals are ordered into arrays of 60 bits length. The analog signals at the discriminator inputs are also digitized and are read out with the signals from the discriminator outputs, so performance and efficiency of the triggers may be monitored. The physics triggers are formed from the sub-detector source signal combinations below.

HCAL towers - 60 segments from 2 end caps, the barrel or whole calorimeter.

HCAL wires - 24 direct module signals or mapped onto 60 segments.

ECAL towers - 60 segments from 2 end caps, the barrel or whole calorimeter.

ECAL wires - 36 direct module signals or mapped onto 60 segments.

ITC pattern - track candidates from 6 ϕ segments.

TPC pattern - track candidates from 60 θ, ϕ segments.

LCAL towers - 2 $\times$ 12 overlapping towers.

Trigger	Sub-detectors used
Single muon	HCAL,ITC,TPC
Single charged electromagnetic energy	ECAL,ITC,TPC
Single neutral electromagnetic energy	ECAL
Single charged hadronic energy	HCAL,ITC,TPC
Single neutral hadronic energy	HCAL
Isolated photon (veto LCAL and ITC)	ECAL,LCAL,ITC
Bhabha	LCAL
Single-arm Bhabha	LCAL
Total energy	ECAL and HCAL
Cosmic	ECAL and HCAL
n-tracks	ITC,TPC
Random	

Table 4.1: Sub-detectors Employed in Trigger Formation.

A particular physics trigger, of which 32 are defined, is formed by taking the trigger conditions from each segment and ORing the segments. These signals are finally ORed to produce a global Level 1 YES/NO decision. Triggers and the sub-detectors they use are shown in table 4.1.

4.2.2 Level 2.

Level 2 is provided almost solely by the TPC with the decision time of $\simeq 50\mu s$ being limited by the TPC drift time. It filters Level 1 track triggers and checks for charged particle trajectories in the TPC which originate from the vertex. If Level 1 is not confirmed the readout is stopped and cleared. The track information provided by the TPC reduces the event rate to less than $10Hz$. Twenty four hardwired processors search independently for tracks in 6 ϕ sectors and 2 radial zones in each end plate.

The timing of the decision is governed by the TPC drift time and the ECAL refresh time. If Level 2 rejects the trigger, the experiment must be ready to accept the third bunch crossing after the one causing the trigger, i.e. after $67\mu s$. The ECAL requires $17\mu s$ to recycle, hence, the decision must be made within $50\mu s$ of the bunch crossing. A positive decision initiates readout of the whole detector. However, a reject decision has to be sent to all sub-detectors within $6\mu s$ of the end of the TPC drift time. To achieve this data is processed as it arrives during the drift period.

4.2.3 Level 3.

Level 3 is the final stage of the trigger system before data is recorded. It is a software implemented decision applied after the entire event is read out, and reduces the event rate to the required $\simeq 1 - 2Hz$. The decision is based on all of the sub-detector digital information from events passing Levels 1 and 2. As the events arrive they are sent in a 'round robin' to different computers running the same process (the ALEPH Event Processor). The concept of the overall programme design was one of efficient pattern recognition and low CPU demand, therefore, high level calibration of the analog signals is avoided. Event reconstruction is only applied to parts of the detector which supply Level 1 and 2 signals. Processing is halted as soon as a YES/NO decision can definitely be made.

4.2.4 Trigger Performance.

In general, annihilation events are triggered by two independent triggers, and other triggers which are not necessarily independent. This redundancy not only reduces the chances of missing an event, but allows the determination of trigger efficiencies. Events are generally triggered by more than one trigger. This reduces the chance of an erroneous YES decision. The trigger efficiencies are

$= 100\%$ for hadronic Z decays.

$\simeq 100\%$ for leptonic Z decays.

$= 99.7 \pm 0.2\%$ for Bhabha events.

Under standard running conditions, 20% of Level 1 triggers are track only. Level 2 removes 75% of these as they are predominantly beam gas events. The overall trigger rate is $0.5Hz$ at a luminosity $\mathcal{L} = 10^{30}cm^{-2}s^{-1}$. The Bhabha efficiency being calculated in the angular region of coverage described in 3.

4.3 The Data Acquisition System (DAQ).

The modular structure of the ALEPH detector necessitates a modular structure for the DAQ system [26,27,28]. Finding the right architecture was important, as although the detector configuration and hardware components may change as technology evolves, the DAQ architecture should remain constant. Also, the hardware and software were built in different institutes. Therefore, a structured data flow design was required so that all of the groups had a template to work with. The Structured Analysis/Structured Design (SASD) method was used. Structured analysis uses data flow diagrams to analyse a project in terms of data flows and processes, where a process creates, modifies or uses a flow. The diagrams are associated to data dictionaries which describe the flows in detail. Structured design incorporates a modular design of all lowest level processes. A strongly hierarchical tree like structure was employed, where components at the same level do not communicate.

Possibly the simplest way to describe the DAQ system, is firstly to examine its key concepts and features, then secondly to look at the DAQ chain and how they are used within it.

4.3.1 Control Flow Architecture.

The data taking cycle has three distinct stages.

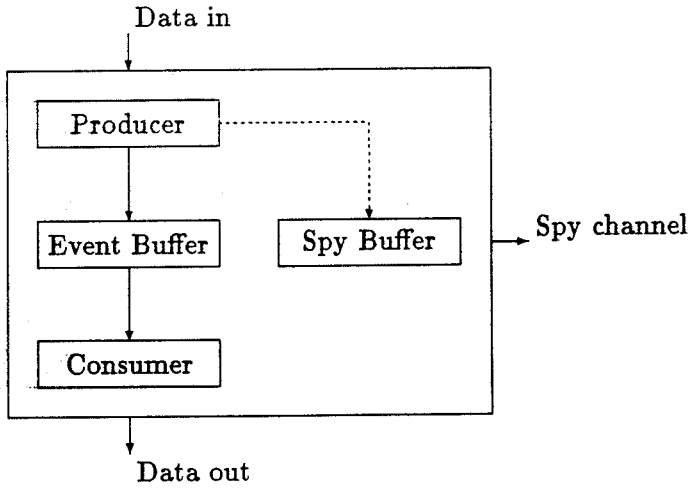

Figure 4.2: Task Architecture of a Processing Element.

a) A set up phase where the detector is made operational and the readout system is configured.

b) The data taking phase.

c) A close down phase which may involve a change in the operational state of the equipment.

The control system has to sequence the actions to ensure that each component is in its correct state at every stage of the cycle. To minimize the number of communication channels between the different processing elements, a dedicated controller task is resident in each readout processor.

4.3.2 Data Flow Architecture.

The task architecture of a processing element is illustrated in figure 4.2. The processing elements act as a master towards the detector and a slave towards the main computer. Therefore, any missing element may be skipped by joining its input and output and completing its function at the next highest level (figure 4.3). This also allows parallel data streams and hence optimizes buffering and processing.

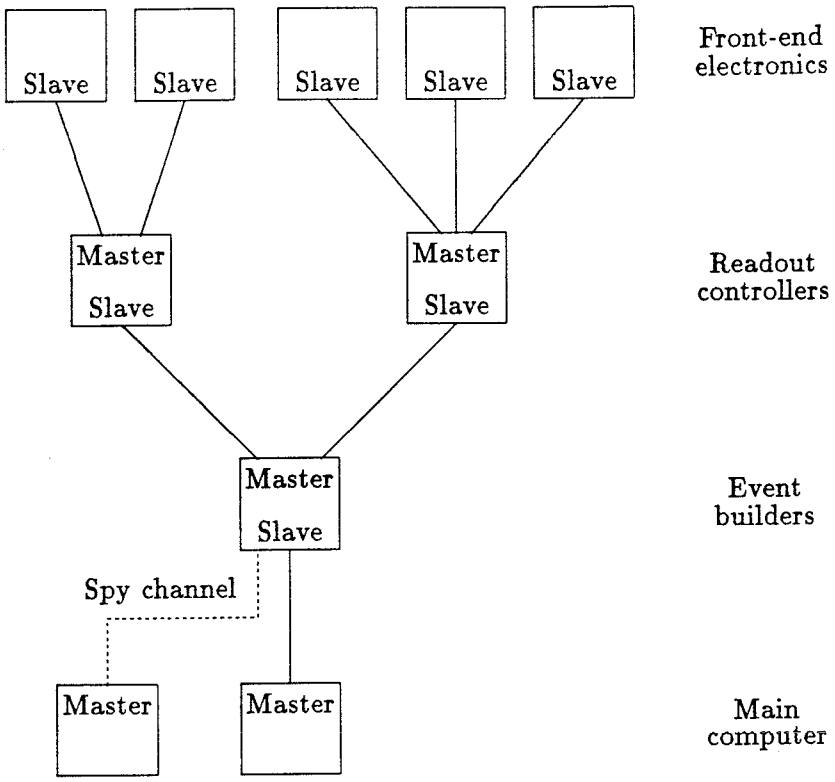

Figure 4.3: Basic Readout Architecture.

On the detector side, all ROC's are connected to the same timing signals, and on the host computer side, an Event Builder stage accepts only data belonging to the same event, thus achieving sychronization. The producer tasks read data from the previous stages and put it in a buffer so that the producer is ready to receive the next event. When the event is in the buffer, the consumer is notified and it transfers the data to the next stage of the readout and frees the buffer. The CDF buffer management package was employed, which ensures that consumers only receive events declared by producers with the same Partition identification.

4.3.3 Architecture Implementation.

The DAQ architecture (figure 4.4) is mainly built from the *FASTBUS* system and uses over 140 *FASTBUS* crates. Some *NIM* and *CAMAC* modules are also used in conjunction with *VME* for communications links.

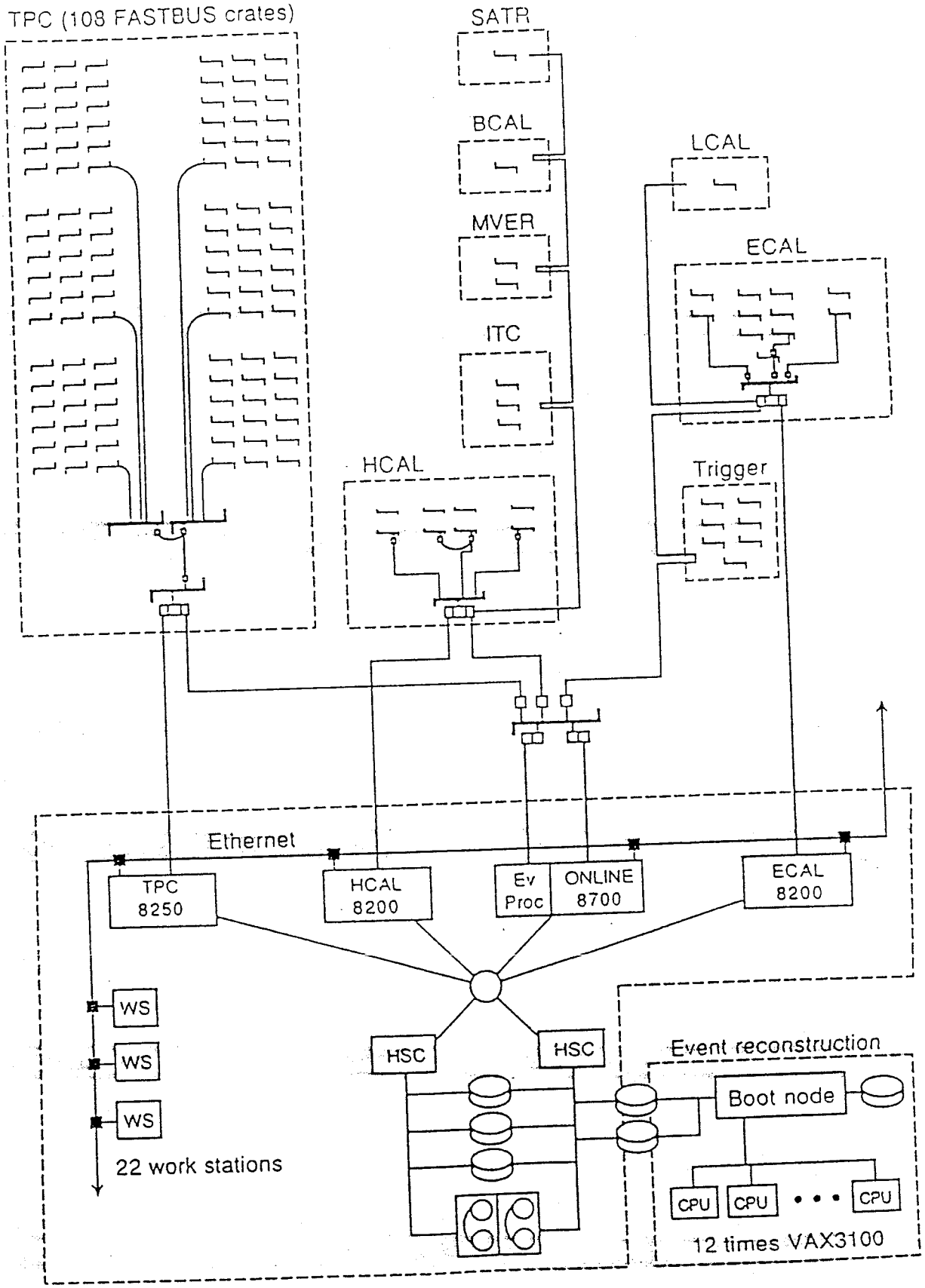

Figure 4.4: Schematic View of DAQ Architecture.

A sophisticated *FASTBUS* data base is employed to keep track of the detector configuration, define devices, define routing tables, routing of service requests and to initialize the system. The embedded processors are a family of 680x0 microprocessors running OS-9. System wide microprocessor support and DAQ control use centralized OS-9 disk server.

A VAX on-line cluster consisting of four BI based machines is used. One, a VAX 8700 serves as the main DAQ computer and main *FASTBUS* host. Three VAX 8200/8250 machines are used by the larger sub-detectors. Additionally 22 VAX work stations are connected to the cluster via *ethernet*, and all the machines share disk and tape drives. The four large VAX's are connected to *FASTBUS* via a $400m$ optical link, where a high performance interface connects *FASTBUS* to the Event Builders. Figure 4.4 shows the central *FASTBUS* crate and its dual path to the main VAX.

The real time performance of the DAQ VAX is supplemented by the 'Event Processor' (Level 3 trigger). This consists of 11 front-end, real time micro-VAX CPU cards which reside on one BI bus. One card acts as a controller and the remaining 10 process the data. Each processor runs the same code as an event is directed from the Main Event Builder to any free processor. Events passing this stage are moved to the memory of the VAX 8700 for later treatment and storage.

Hence, as there are only two CPU architectures involved - 680x0 and VAX, data conversion, which is a prerequisite of data transfer is minimized.

FASTBUS **Management.**

The *FASTBUS* database describes the components of *FASTBUS* and includes

a) Crates with a name, group address, type of logic etc..

b) Devices with a name, type and address.

c) Generic information on each device type.

d) Information relating to master/slave routes and service request sources and handlers.

The database design incorporates many rules of *FASTBUS* and can describe any *FASTBUS* system.

4.3.4 The Partition.

It is important that the detector appears as an integrated system of sub-detectors. Therefore the DAQ collects data independently from the different modules. The Partition was developed specifically for this purpose.

The Partition permits any subset of the DAQ system to be configured so that it can respond independently to triggers from the the remainder of ALEPH. Several Partitions may function simultaneously facilitating parallel data streams. Each can be viewed as an independent pipeline where data flows from the front end electronics to a consumer task running in one of the online processors. Hardware can not be shared across Partition boundaries, therefore, each Partition requires its own readout and trigger system. The global DAQ involving all of the sub-detectors is also a Partition in its own right. This is made possible by the selection of any combination of Read Out Controllers (ROC's) to take part in the data taking. It is implemented by programming Fan In Fan Out (FIO) units such that only those ROC's in the Partition receive trigger signals. The FIO units are cascaded to connect $\simeq$ 100 ROC's. They send timing and trigger signals to the ROC's and receive *BUSY* and *ACK* signals from them.

The ALEPH Partition Manager (APM) is a software utility which defines the Partition descriptions and creates an environment suitable for data taking. Data flow within the Partition can be seen in figure 4.5.

a) Digitizings from the sub-detector front-end electronics are processed and built into sub-detector events.

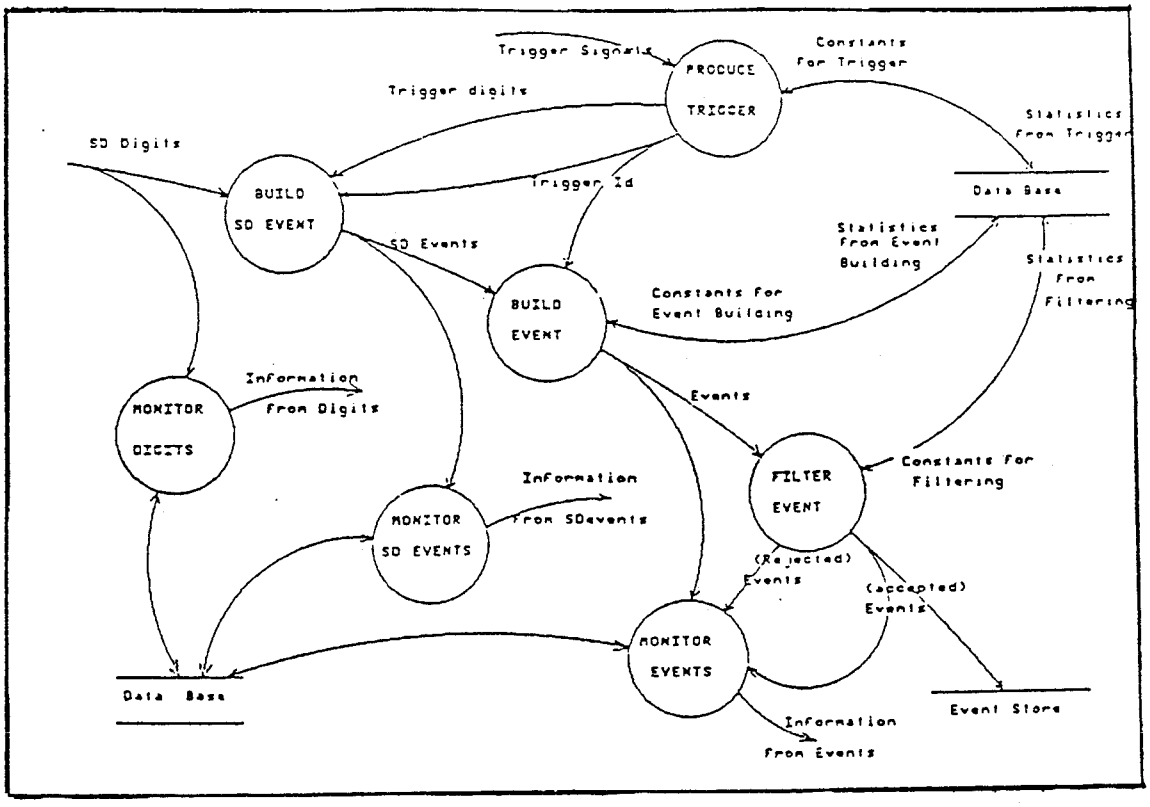

Figure 4.5: Data Flow in the Partition.

b) Sub-detector data structures (BOS) are combined to produce complete events.

c) The events are filtered to remove unwanted triggers and the data is recorded.

d) Data may be monitored at each stage and is supported by on-line computers.

4.3.5 Sub-Detector Partitions.

Any sub-detector can contribute data to the global DAQ, or can function in a stand alone state. Within a sub-detector, the trigger information is sent to the front-end electronics by the trigger supervisor. The readout process is controlled by the ROC's, and the FIO units manage the routing and logic of the trigger signals. The sub-detector event is constructed in an Event Builder (EB).

The Trigger Supervisor.

The trigger supervisor is a programmable *FASTBUS* module which synchronizes the readout process. It gets data from the trigger relating to the beam crossing, Level 1 and 2 decisions and the type of trigger. The ROC's send front-end *BUSY* signals to the trigger supervisor. All time critical signals are routed via the FIO boxes and other data is sent to the ROC's in a global broadcast after every Level 2 trigger.

Read Out Controllers (ROC's).

The ROC's are also *FASTBUS* modules acting as masters to the crate segment they control and slaves to the cable segment connected to the EB. ROC's are specific to each sub-detector but the protocols are identical. They receive trigger information, control the front end readout sequence and collect, format and store the digitized data in buffers so it can be accessed by an EB.

Event Builders (EB's).

Event builders gather data from all ROC's of a sub-detector and construct a sub-detector event. The readout process is initiated by a Level 2 YES decision. An EB can 'spy' on a sub-detector event for monitoring purposes.

4.3.6 Data Handling.

Data Reduction.

The raw data is reduced in two ways.

i) - Triggers reduce the rate.

ii) - Zero suppression and online calibration compactify the data. Zero suppression is a hardware process achieved by comparing the measured analog values with

preloaded thresholds. The ROC's format and calibrate the data signals, which may not reduce the data volume, but does save CPU time later.

Data Base and Storage.

A typical event is $\simeq 100kbyte$ and reconstructed output is written to a large disk subsystem, which houses all of the current years data. Previous years data is transferred to magnetic tape and cartridge, which is also the medium used to distribute the data to home labs.

The data base itself houses many megabytes of data in several formats and classifications. The online system requires fast and efficient access to typically $\simeq 100kbyte$ at a time. A relational data base provides all of the required features but the access time may be slow. For this purpose the ALEPH Data Model (ADAMO) was developed. It manipulates data tables in a core area of memory. The relational data base manager can organize the data into tables which are then loaded into memory where ADAMO can be used to increase the access speed.

4.3.7 Read Out Architecture.

Having previously described various sections and features of the DAQ, the complete flow of data and control signals from the bunch crossing to storage of the event can be summarised as follows, and is illustarted in figure 4.6

a) A timing signal from the $T0$ module is received by the trigger and Main Trigger Supervisor (MTS). The MTS synchronizes the readout electronics to the accelerator, notifies the ROC's via FIO modules about the availability of data, keeps track of the protocols and synchronization of the controllers, and measures the dead time.

b) ROC's initialize the front-end modules, read them out, format the data and do any initial calibrations.

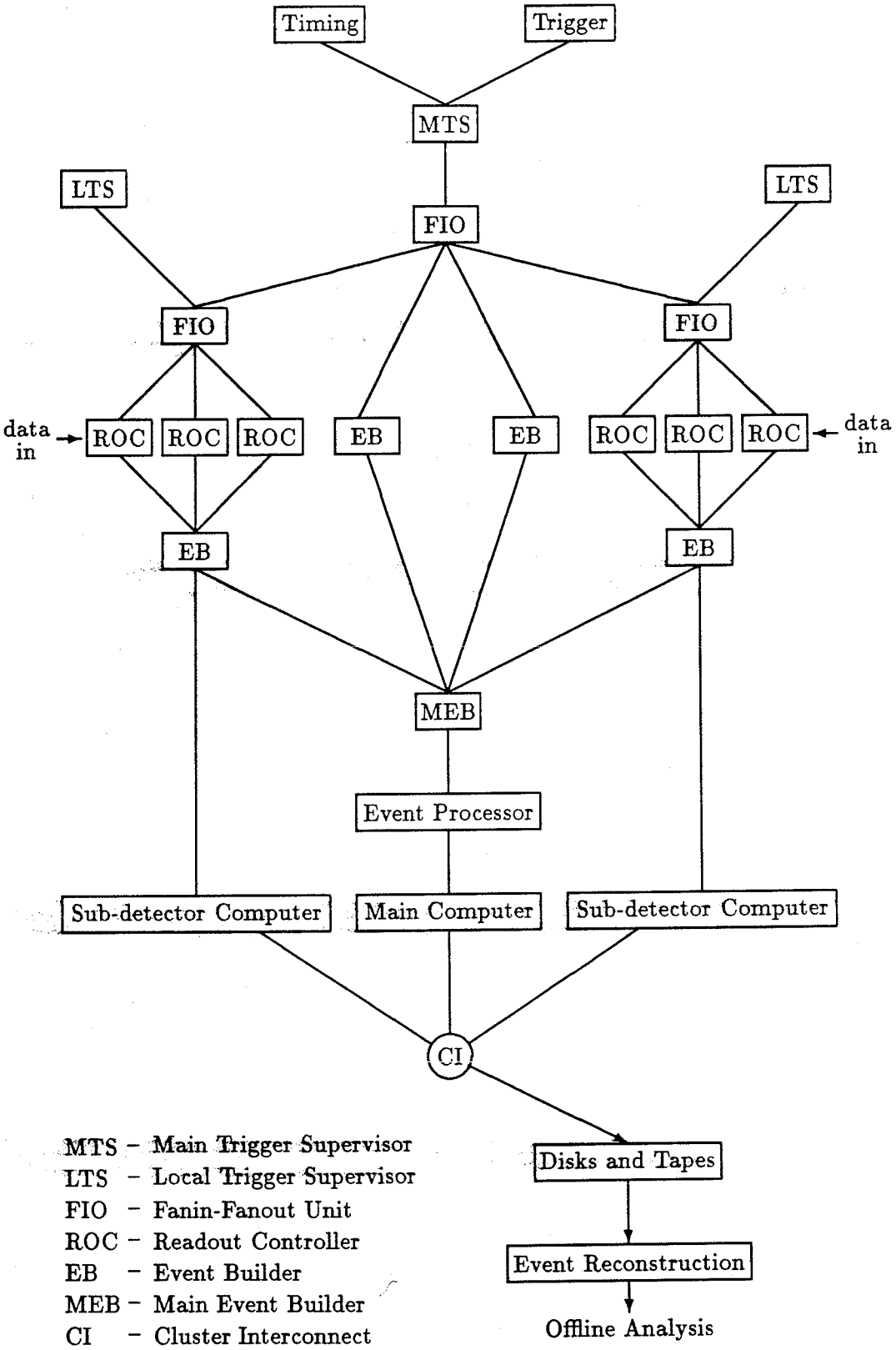

Figure 4.6: A Simplified View of the DAQ System.

c) EB's build sub-events at the sub-detector level and provide spy events to the sub-detector computers.

d) The Main Event Builder takes all pieces of the event from the sub-detector EB's and resynchronizes them if necessary before constructing the full event.

e) The Event Processor refines and reduces the data.

f) The main host and sub-detector computers collect the data for storage, on-line analysis, event display etc.. The sub-detector computers receive spy events and monitor the larger sub-detectors.

g) Event reconstruction occurs quasi-on-line at the experiment.

A full 32 bit architecture is employed in the DAQ chain, allowing for future expansion. The single family of machines used greatly simplifies the data flow.

4.4 Event Reconstruction.

After the DAQ readout is completed and the event has been assembled into one piece, the raw data is written to tape. However, before any physics analysis can be carried out, the data has to be reconstructed into a physics event of a discernible nature. This is done by the JULIA reconstruction programme which consists of three stages.

a) Individual corrections are applied to each sub-detector.

b) Raw data digitizings are reconstructed into hits in tracking chambers or energy deposits in calorimeters and then into particle tracks.

c) The particles are identified.

The reconstruction process is carried out quasi-on-line at the rate the events are produced, by a local area VAX cluster (FALCON 1) consisting of one boot node and 12 processing nodes. The 12 work stations each run the full operating system (*VMS*) and

the ALEPH reconstruction programme (JULIA), and operate in parallel to reconstruct the events. The results of the reconstruction are written to separate disk files which are then combined into a single file. The reconstruction output files are then immediately sent to off-line computers for analysis, writing to tape/cartridge (POT) and distribution to home labs.

4.5 Particle Track Reconstruction.

The tracking detectors are housed inside the ALEPH solenoid, which provides a uniform magnetic field of $1.5T$ parallel to the z-axis in the direction of positive z. Therefore, a charged particle experiences a force in the $x-y$ plane and its subsequent motion in this plane is curved. The overall motion of the particle is helical as its direction of flight is at an angle to the z-axis. The radius of the circle in the $x-y$ plane is dependent on the momentum of the particle and its angle of emission relative to the z-axis. This is illustrated in figure 4.7 along with the other parameters used to define the helix which are listed below.

ω - Inverse radius of curvature, signed $-ve$ if the track bends clockwise in the $x-y$ plane.

$tan\lambda$ - Tangent of the dip angle in the $S_{xy}-z$ plane. S_{xy} is the length of the track in the $x-y$ plane measured from the point of closest approach to the origin in that plane.

ϕ_0 - Emission angle in the $x-y$ plane at the point of closest approach to the origin in the $x-y$ plane.

d_0 - Distance of closest approach to the origin in the $x-y$ plane.

z_0 - Z coordinate measured at $x^2+y^2=d_0^2$.

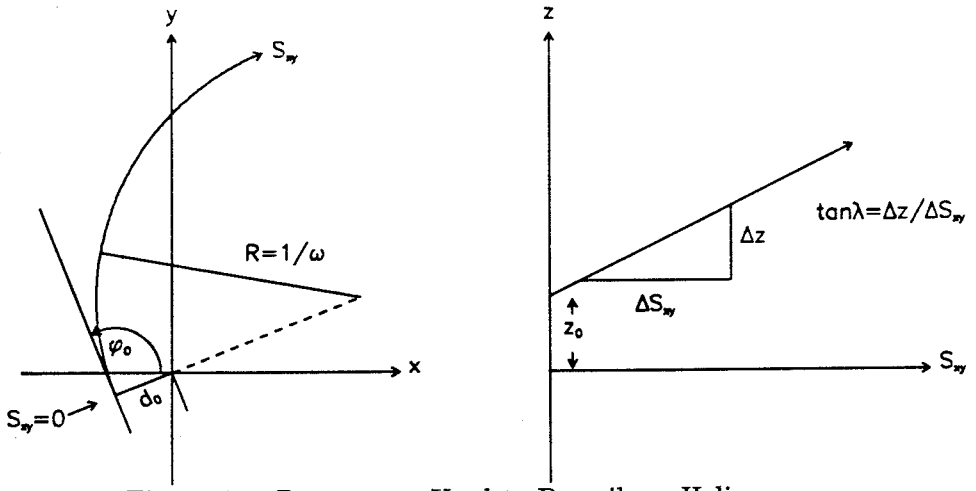

Figure 4.7: Parameters Used to Describe a Helix.

4.5.1 TPC Coordinate Determination.

The raw TPC data contains 2 major pieces of information

a) Pad hits containing the pad address, hit arrival time and pulse length.

b) Digitized pulse heights per time-slice ('bucket') corresponding to the pad hits.

Cluster Formation.

The first step of the coordinate reconstruction is the creation of 2-dimensional clusters. A typical cluster is shown in figure 4.8. The reconstruction proceeds as follows.

a) The pad hit information is used to define clusters of hits for each pad row.

b) The pad hits are linked to form a cluster if they lie on adjacent pads and overlap for at least one time-slice.

c) A good cluster is defined

$2 \leq$ number of pads in the cluster ≤ 20.

$5 \leq$ cluster length in time slices ≤ 35

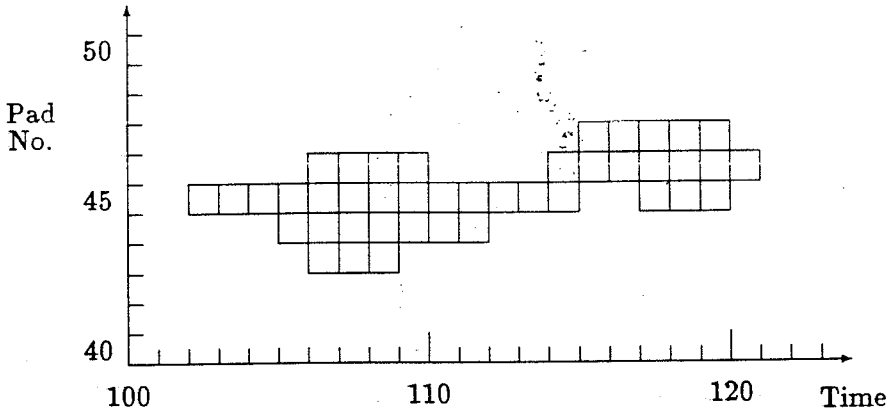

Figure 4.8: A Typical TPC Pad Cluster Formed by Two Tracks.

Sub-Cluster Formation.

Each pad within a cluster is then considered individually. The digitized pulse height information is used to try and divide the pad pulse into contributions from different tracks. (see figure 4.9). A sub-pulse is defined for each pad so that there is only one distinct maximum in the pulse height distribution for each sub-pulse. Sub-pulses from adjacent pads are linked into sub-clusters if they are consistent with originating from the same track. This is determined from the drift times associated to each sub-pulse. Sub-clusters can be divided in $r-\phi$ but only if the number of pads in the sub cluster $3 < n_{pads} < 7$.

Coordinate Determination.

Each sub-cluster is used to calculate a coordinate in z and $r-\phi$ using charge and time estimators for each sub-pulse of the sub-cluster. A sub-pulse charge is calculated from the sum of all samples with > 2 ADC counts. A time estimate is the mid-point between the leading and trailing edges of the pulse.

z-coordinate - Calculated from the charge weighted average of sub-pulse times within the sub-cluster. The known drift velocity is used to convert the time into a drift length.

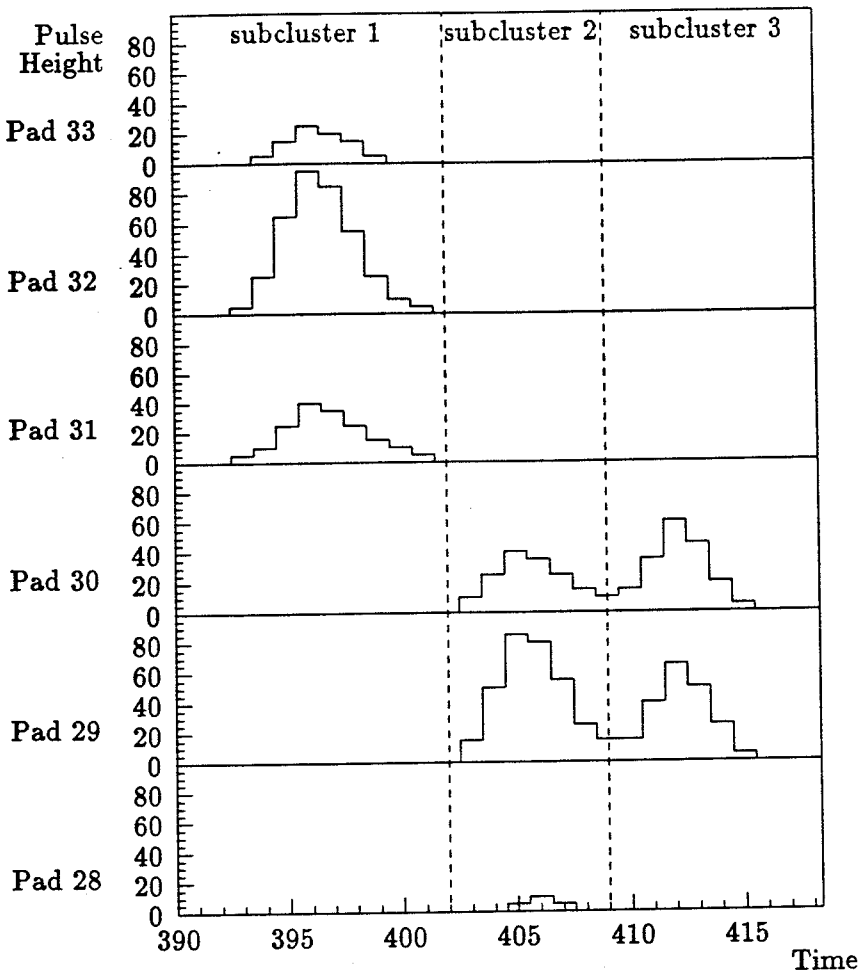

Figure 4.9: The Splitting of a Cluster into Three Sub-clusters.

$r-\phi$-coordinate - If the sub-cluster contains 2 or 3 pads the coordinate is obtained via a Gaussian fit to the pulse heights on the pads. For sub-clusters with ≥ 4 pads a charge weighted average of the pad positions is used.

4.5.2 ITC Coordinate Determination.

The ITC provides 3-dimensional coordinates for charged particles in the form of z and $r-\phi$ values.

$r-\phi$ - Determined via the drift time of charges collected by anode wires. The drift time defines a circle around the wire, but the exact position of the coordinate on the circle can not be found until the track is fitted through a drift cell.

z - determined from the difference of pulse arrival times at each end of the anode wire.

4.5.3 TPC Track Finding.

Coordinates from the ITC and TPC are used to reconstruct the helical tracks of charged particles. Neutral particles obviously leave no trace in the tracking chambers and are considered later in calorimeter reconstruction. The fitting of tracks to the coordinates involves three main stages.

Chain Formation.

Sets of radial points known as chains are formed as follows.

a) - A search is made in the list of TPC coordinates for groups of 3 points from adjacent pad rows which are consistent with lying on a helix.

b) - The points are fitted to a circle in the $x-y$ plane and a straight line in the S_{xy} plane.

c) - A 'road' about the fit is defined and a search for points lying within the road is made.

d) - Points found on pad rows adjacent to the currently associated points and inside the road are themselves associated to the chain. The track is then refitted to all of the points.

d) - When 2 adjacent pad rows have no associated coordinates the search is terminated.

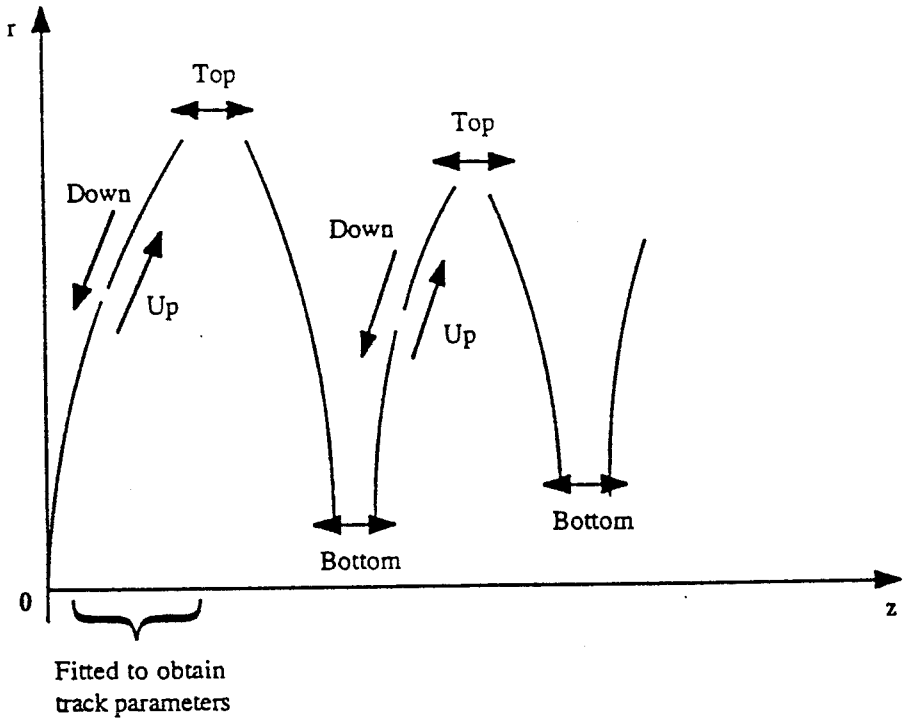

Figure 4.10: Possible Links Between Coordinate Chains.

Helix Formation.

Next, a helix is fitted to each chain. The helix is extrapolated to larger and smaller radii to define a road around a chain. A search for more coordinates within the road is made, and as they are added to the chain the road width decreases. Checks are performed to ensure that tracks split in the chain finding process are correctly recombined. Tracks may be split as low momentum tracks spiral in the TPC and form many chains, all of which have to be reassociated. Figure 4.10 shows the possible links that can be made between chains. The links are made by comparing the helix parameters of the individual chains to find pairs that fit.

Helix Fitting.

The first half of the arc of all track candidates fitted to a helix are used to extract the track parameters. The helix fit consists of two steps, a circular fit in the $x - y$ plane

yielding ω, d_0 and ϕ_0, and a straight line fit in the $S_{xy} - z$ plane yielding z_0 and $tan\lambda$. Four levels of fitting are successively applied until the required quality of fit is achieved.

1) A track is fitted without modification to a chain of points.

2) On the basis of their χ^2 values, up to two coordinates may be removed and the track is refitted.

3) A search for kinks in the track is made. If a kink is found the track is split.

4) Successively remove one coordinate and refit the track.

If after the fourth stage the required accuracy has not been attained, the fit from stage 1 is retained.

4.5.4 Combined ITC-TPC Track Finding.

Coordinates from both the ITC and TPC can be used in conjunction with each other to define tracks and provide more accurate fits. The TPC tracks are projected back into the ITC and hits within a road about the projection are associated to the track. If there are no hits within the road in the outer 2 layers of the ITC the search is abandoned. If 3 or more of the ITC layers have hits associated with a TPC track, then the track is refitted to both the TPC and ITC coordinates.

4.5.5 Calorimeter Reconstruction.

Before reconstruction of energy in the calorimeters occurs, the raw data is corrected for dead storeys and dead wires. Due to the large amounts of noise in the ECAL electronics, a cleaning procedure is also applied before reconstruction. In events which are only triggered by LCAL, any energy in the storeys of ECAL is assumed to be noise and is subtracted from other events. The three stages of the calorimeter reconstruction are

1) Find topological clusters of fired calorimeter storeys.

2) Assign tracks reconstructed in the ITC and TPC to the clusters.

3) Find relationships between ECAL and HCAL clusters.

Cluster Finding.

In the initial stages of cluster formation, the ECAL and HCAL are treated separately. A cluster is formed from a group of neighbouring storeys, whereby two fired cells are combined into a cluster if they have at least one adjacent corner. In the ECAL a storey must have an energy $> 30MeV$ to be included in the clustering process, and a cluster is only defined if at least one storey has an energy $> 90MeV$. There are no thresholds applied in the HCAL.

Track Assignment.

Tracks found in the ITC and TPC are projected into the ECAL. If any of the storeys intersected by the extrapolation are part of a cluster, or have a corner in common with a cluster, then the track is associated to that cluster. If more than one cluster is associated to the track, they are combined to form an ECAL object. Many tracks can be associated to one cluster and likewise, many clusters associated to one track. Thus, one to many relationships are defined.

Calorimeter Cluster Association.

The association between ECAL clusters, HCAL clusters and tracks are formed by considering three distinct cluster types.

Minimum Ionizing Particles (MIP's).

Tracks with ECAL clusters consistent with the track being a MIP, are extrapolated through the HCAL wire planes. In each plane the distance between the projection and any storey containing an energy deposit is calculated. Any HCAL clusters falling within a set distance of the track projection are associated to the track.

Non-Minimum Ionizing Particles.

Clusters in the ECAL which are not due to MIP's are associated to HCAL clusters on the basis of relative transverse momentum p_t. Again, the track associated to the ECAL cluster is extrapolated into the HCAL. The distances between the projection and the HCAL clusters are calculated, and the p_t associated with the distances determined. The ECAL and HCAL clusters are associated if the p_t is less than a predefined value.

Neutral Clusters.

ECAL clusters without a TPC track association are classed as being neutral. Their 'track' is defined by a straight line from the event vertex to the cluster.

4.6 Detector Simulation.

The ALEPH detector is simulated with the GALEPH programme, which is a mathematical model of the detector. Initially, the major role for GALEPH was in the development of the JULIA reconstruction programme. However, GALEPH is now almost solely used to calculate corrections arising from the detector acceptances and efficiencies. The corrections are applied to physical distributions and cross sections and must be well understood if any meaningful comparison is to be made between real data and theory. Any type of event generator can be interfaced to GALEPH via the KINGAL programme, which produces the particle 4-vectors for particles from an event generator. GALEPH is then responsible for

a) Tracking particles through the inner detectors and showering particles in the calorimeters.

b) Converting analog signals to digital values.

c) Trigger simulation.

c) Converting all data into a raw data format.

The ALEPH detector geometry, properties and construction are described by GEANT. GEANT performs tracking of particles through the inner detectors allowing for multiple scattering, energy loss via ionization, decays, pair production etc.. Electromagnetic interactions are simulated by GEANT and hadronic interactions by GHEISHA. The analog signals from the sub-detectors are converted to digital output by simulation of each sub-detectors electronics, allowing for noise, thresholds, gain variations etc.. The digital output is finally formated exactly as if it were real data to produce a raw data file which can be interfaced to JULIA.

Chapter 5

Event Selection.

5.1 Introduction.

A crucial factor in any analysis of experimental data, is the efficiency and surity with which we can select the events of interest, while at the same time, discarding event types that we do not wish to include. These events are termed background and need to be eliminated, or more realistically reduced to a small fraction of the total event sample. However, the selection criteria must not be so stringent that they also drastically reduce the data of interest. Moreover, prior to any event selection, data from ALEPH events must be reconstructed. The accuracy and efficiency of this process also has to be well understood if any credence is to be attached to analysis based on the data.

In tests of QCD processes and interactions, the strong force is the dominant underlying factor, which in turn requires the use of hadronic events in the subsequent investigations. Hadronic events are in general, a complex array of many final state charged tracks which between them carry a large fraction of the centre of mass energy. Therefore, the primary concern is the precision with which charged tracks can be reconstructed and identified within the central tracking detectors of ALEPH (ITC and TPC).

In both tests of track reconstruction and event selection, much use is made of Monte

Carlo simulated data. This is produced by several event generating programmes which will be described in turn later. The event generator output is then passed through the GALEPH detector simulation programme, before finally being processed by the JULIA reconstruction package. It is therefore vital that GALEPH provides a true reflection of the detector output.

5.2 Charged Track Reconstruction and Selection Efficiency.

Charged tracks in the ITC and TPC are reconstructed by JULIA. The reconstructed tracks fall into two predominant classes.

a) - Good tracks - which are genuine paths of charged particles. These are either well measured or badly measured and originate from

1. The Interaction Point (IP).
2. Decays of short lived particles.
3. Particle interactions with detector material and beam gas interactions.

b) - Bad tracks - which JULIA reconstructs by incorrectly combining real track coordinates and by the use of bad coordinates.

To study the reconstruction and selection efficiencies, $q\bar{q}$ events were generated using the $DYMU02 + HVFL02$ event generator, in conjunction with the LUND $JETSET$ parton shower fragmentation scheme [29,30]. The events were then passed through GALEPH and JULIA. The tracks are reconstructed from coordinates of hits in the ITC and TPC. The ITC provides $4 \leq n_{ITC} \leq 8$ and the TPC $3 \leq n_{TPC} \leq 21$. (It is possible for a track to have no ITC or TPC hits if the track fails to escape from the ITC or has a very low dip angle). However, the ITC's limited resolution combined with the high track density within its volume results in the creation of many false tracks.

Also, until the ITC z-processor becomes operational, only 2-dimensional coordinates are available. Therefore a track possessing only ITC coordinates cannot be relied upon to give an accurate representation of the track.

The track finding efficiency of JULIA has been found to be $98.6 \pm 0.2\%$ [31]. However, falsely created JULIA tracks still have to be eliminated. These may be due to bad tracks, partially lost tracks or tracks which are split. Also, it is desirable to remove tracks from beam gas interactions and cosmic rays, which although genuine are both possible backgrounds in an event. However, the scheme employed must not discard tracks which have been faithfully reproduced. The method used to determine whether a reconstructed track is good or not is as follows. Reconstructed tracks are matched to Monte Carlo (MC) generated tracks (or true tracks). A one to one relationship does not exist here as JULIA reconstructs false tracks which have no MC association. These are the bad tracks which must be eliminated. The matching procedure used is as follows.

1. All reconstructed tracks in an event are considered in turn.
2. All MC tracks which are potential matches to the reconstructed track are examined.
3. To be considered as a match, the two tracks must share at least 4 hit coordinates.
4. If more than one track is matched, the pairing with the greatest number of shared hits is taken.

The reconstructed JULIA tracks could then be be divided thus

Matched tracks - which are matched to MC tracks. These in turn can be subdivided into

i) - Primary tracks which originate from close to the IP.

ii) - Secondary tracks whose origin is away from the IP.

Unmatched tracks - for which no match to a MC track can be made.

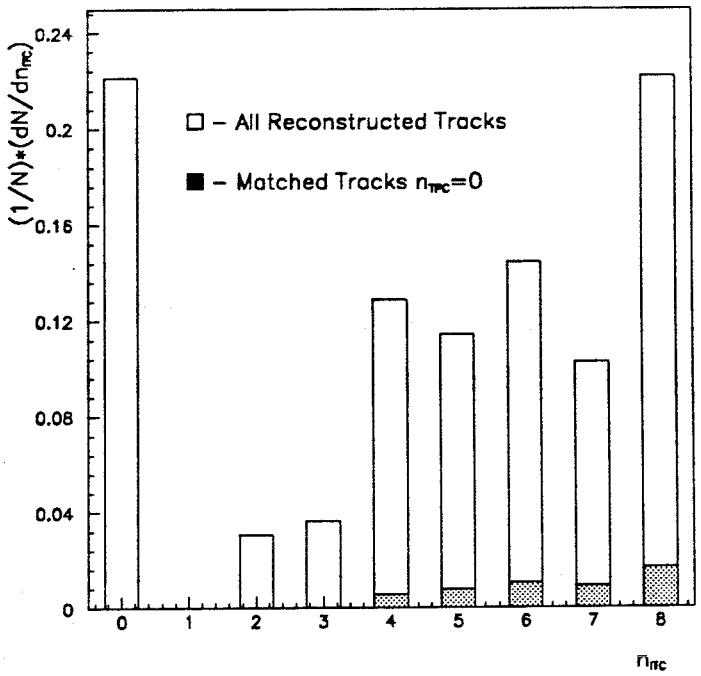

Figure 5.1: Track Matching as a Function of ITC Hits.

The secondary tracks are produced by short lived particle decays and interactions with the detector material etc.

Figure 5.1 shows all reconstructed tracks and those with only ITC hits that are actually matched. This highlights the ineffectiveness of relying upon tracks created solely within the ITC volume. Demanding that a track has $n_{TPC} \geq 4$ removes almost all spurious tracks created from the ITC alone so little inefficiency is added by not using the ITC. Very few tracks have 3 or fewer TPC coordinates and those that do have very poor momentum resolution, or may be fitted through coordinates which belong to other tracks. Thus, the loss in efficiency by not using the ITC is negligible.

To determine whether a track is good or bad, several parameters are employed. These are outlined below.

n_{TPC} - number of TPC coordinates.

θ - the polar angle of the track relative to the beam axis.

p_t - the tracks transverse momentum relative to the beam axis.

d_0 - distance of closest approach of the track to the beam axis in the $x-y$ plane.

z_0 - distance along the beam axis at the point where d_0 is measured.

Their relationship with matched or unmatched tracks is now examined further, and cuts on their values to optimize rejection of unmatched tracks determined. The MC data is also compared with real data to ensure that the two are compatible and that the cuts will be equally valid when applied in the experimental case

$n_{TPC} \geq 4$ - Figure 5.2 shows that this cut greatly reduces the number of falsely reconstructed tracks with little effect on good tracks. The majority of good tracks that are removed have very poor momentum resolution due to the low number of coordinates that they posses.

$cos\theta$ - It can be seen (figure 5.3) that the polar angle θ is also related to n_{TPC}, as to traverse ≥ 4 TPC pads, a track must have $|\theta| \geq 16.5°$. A cut of $|cos\theta| \leq 0.95$ is imposed which corresponds to a polar angle of 18.2°. This ensures that tracks are clear of the TPC boundary and traverse at least four pad rows.

P_t - A track's transverse momentum (figure 5.4) is also related to both θ and n_{TPC}. Tracks with very low P_t are likely to turn over and spiral, resulting in poor momentum resolution for the track due to multiple scattering and the low number of TPC pads traversed. This in turn decreases the probability of correctly identifying the particle concerned. A cut of $P_t \geq 0.2GeV$ reduces this effect and removes many bad tracks.

$d_0 - z_0$ - The combination of these parameters defines a cylinder about the interaction point with the beam axis running along its centre. Projections of tracks trajectories are required extrapolate back through this nominal volume. (figures 5.5 5.6) The values of d_0 and z_0 should be tight enough to remove tracks from beam gas or detector interactions and cosmic rays, yet still include tracks from short lived particle decays. These cuts are the harshest in terms of removing bad tracks but this is not without

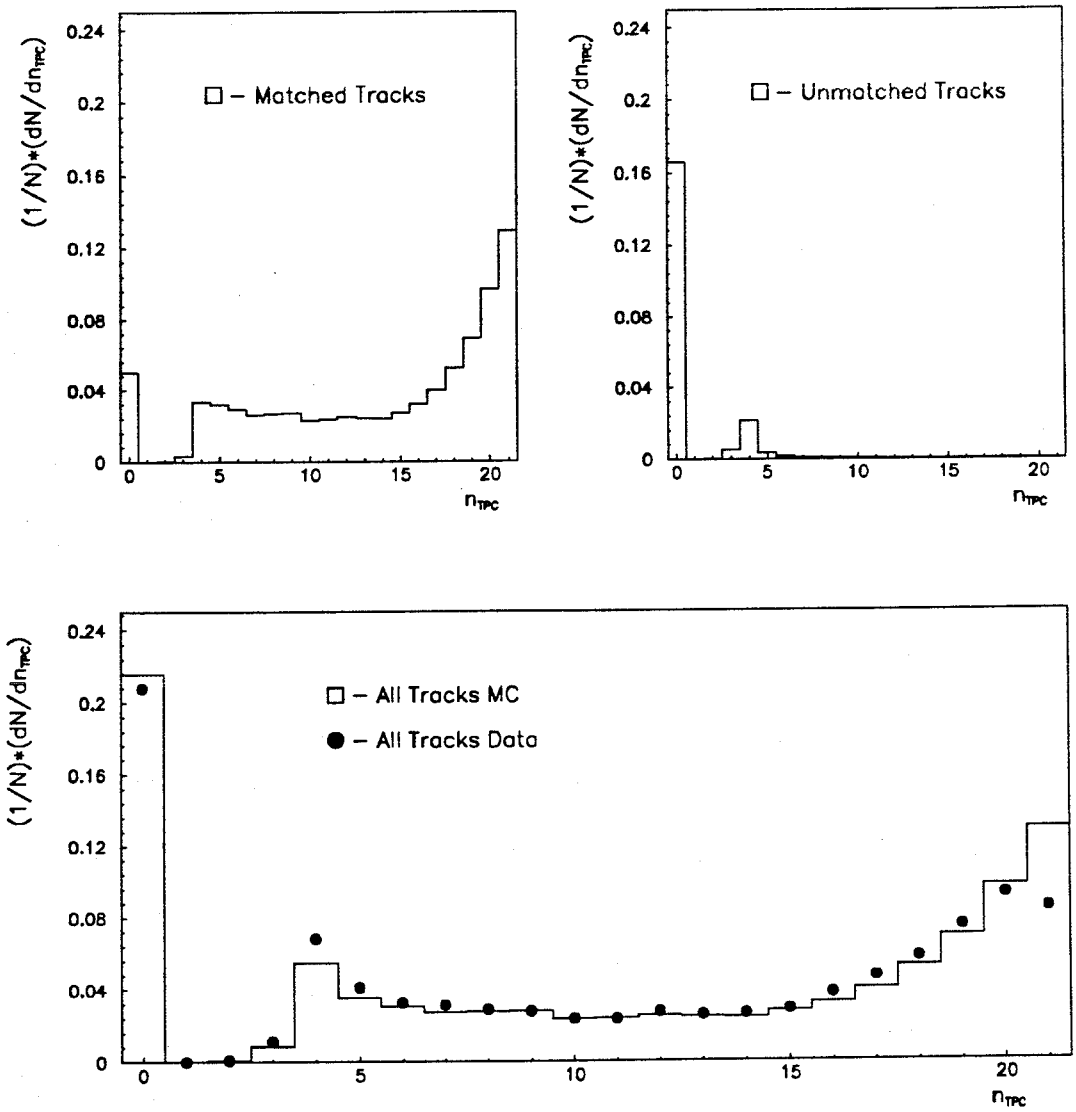

Figure 5.2: Track Matching as a Function of TPC Hits.

some effect on well reconstructed track elimination.

In summary, a reconstructed track is accepted as good if it satisfies the cuts below.

- $n_{TPC} \geq 4$
- $|cos\theta| \leq 0.95$
- $P_t \geq 0.2GeV$

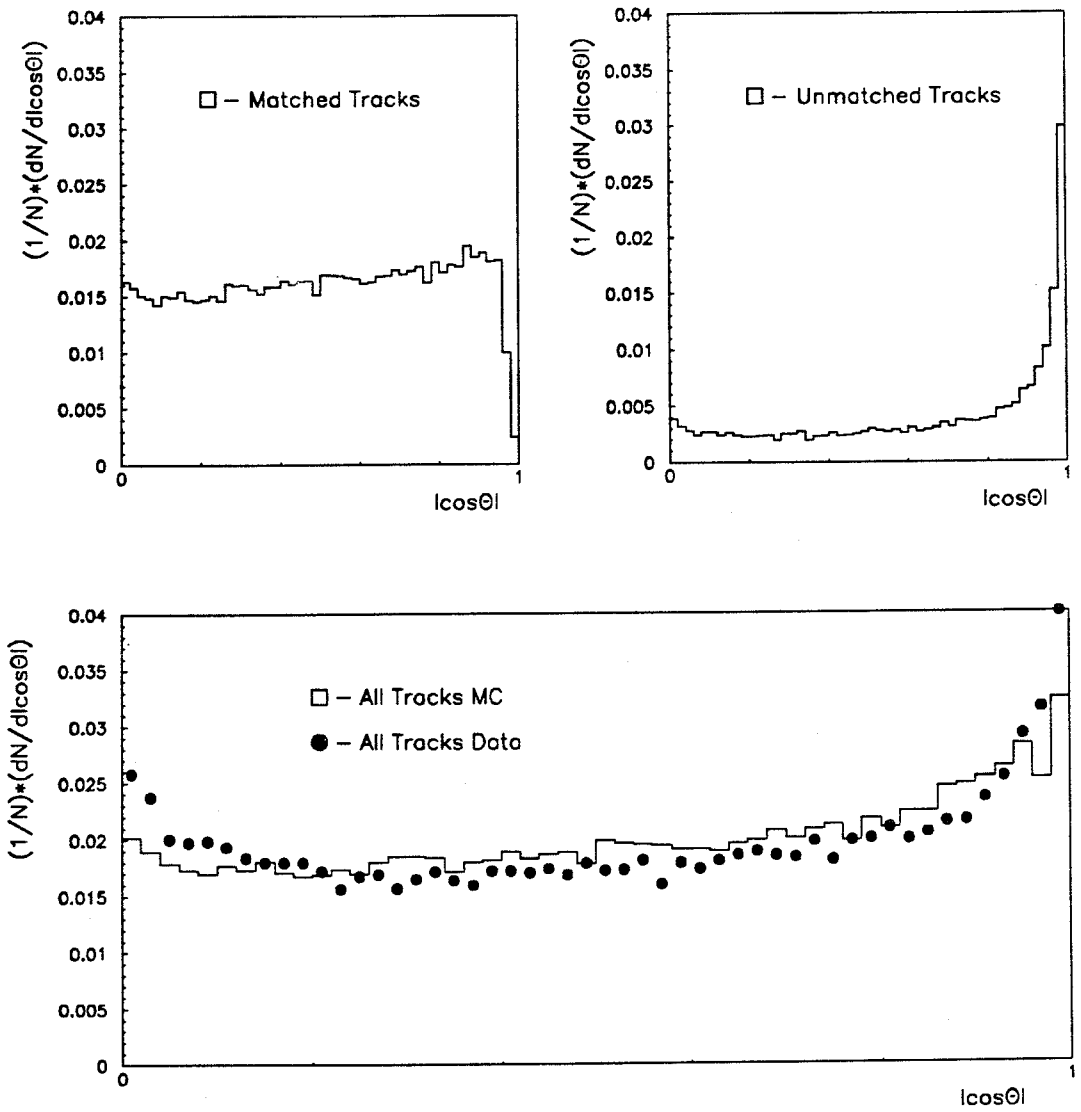

Figure 5.3: Track Matching as a Function of Polar Angle θ.

- $|d_0| \leq 2.0cm$
- $|z_0| \leq 5.0cm$

The effect of these cuts on the unmatched tracks tracks is shown in table 5.1. The figures represent the efficiencies of accepting and rejecting unmatched tracks. (The errors are statistical). It should be noted that some 20% of JULIA tracks are unmatched.

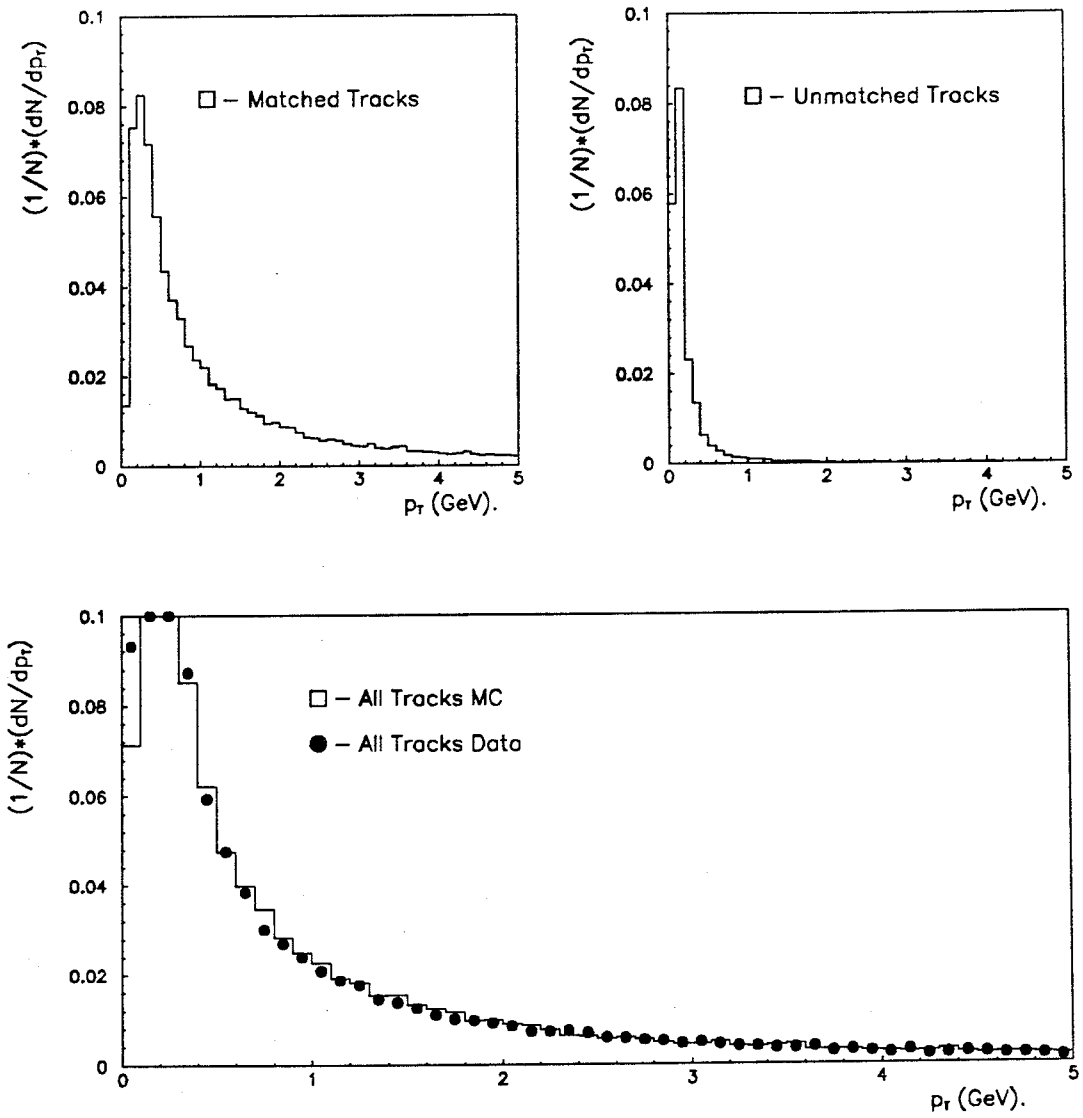

Figure 5.4: Transverse Momentum P_t of Tracks.

5.3 Event Selection.

Having defined and selected reconstructed charged tracks, we can proceed to select events of interest for a particular analysis. Efficient selection of hadronic events is enabled by their high charged track multiplicity n_{ch} and charged energy fraction E_{ch}. These features also allow us to successfully eliminate almost all background processes.

Monte Carlo events were produced by several event generating programmes [29,30,32]

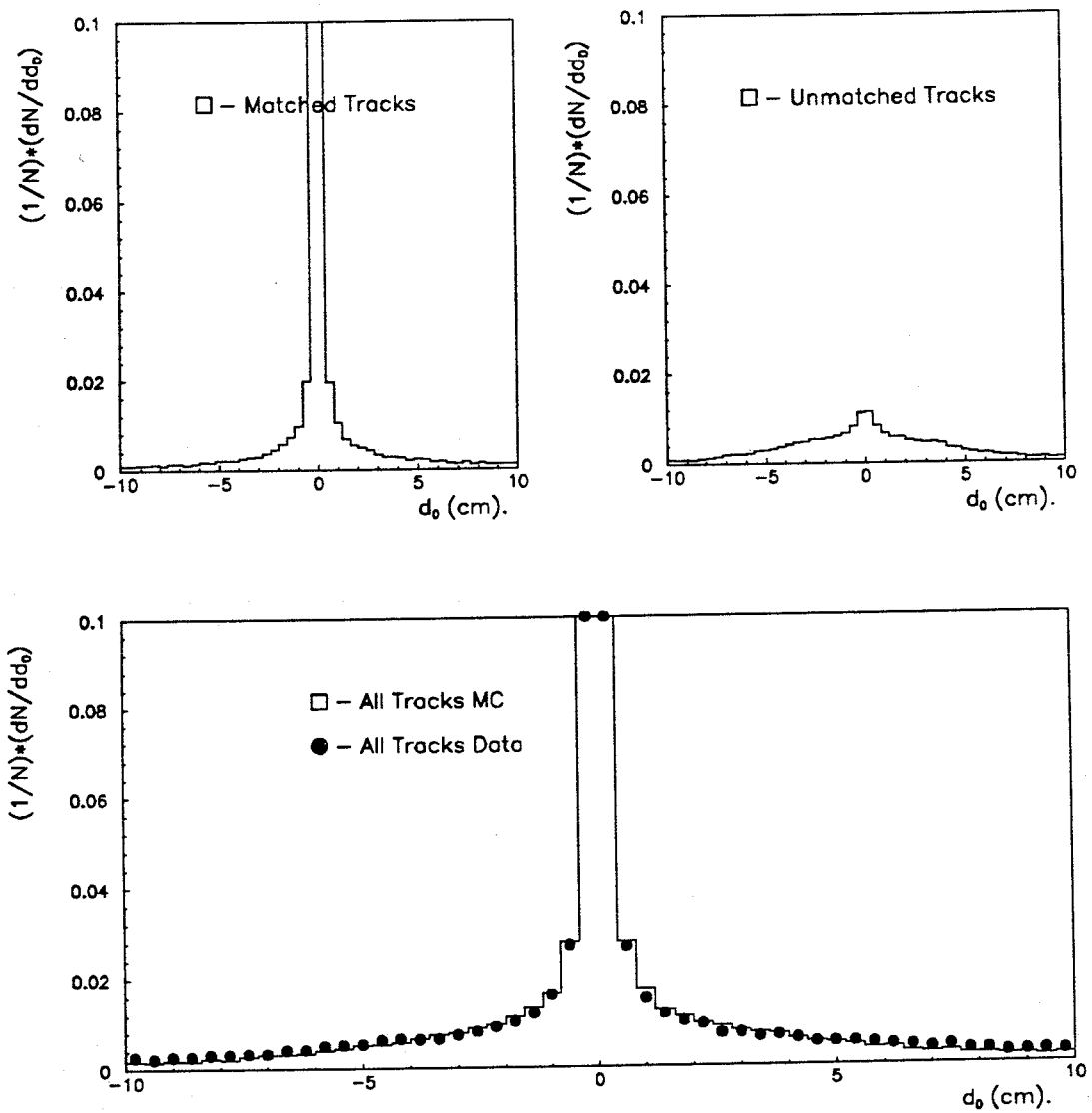

Figure 5.5: Track Extrapolation wrt the d_0 Parameter.

to encompass the range of event types observed at LEP. The event generator output was then passed through GALEPH and JULIA.

Figure 5.7 shows the charged multiplicity for each events type. The e^+e^- and $\mu^+\mu^-$ events clearly peak at $n_{ch} = 2$. Occasionally more tracks are produced due to particle interactions with the detector. Fewer tracks are observed when tracks are lost or escape down the beam pipe. A cut of $n_{ch} \geq 5$ eliminates all but a negligible fraction of these

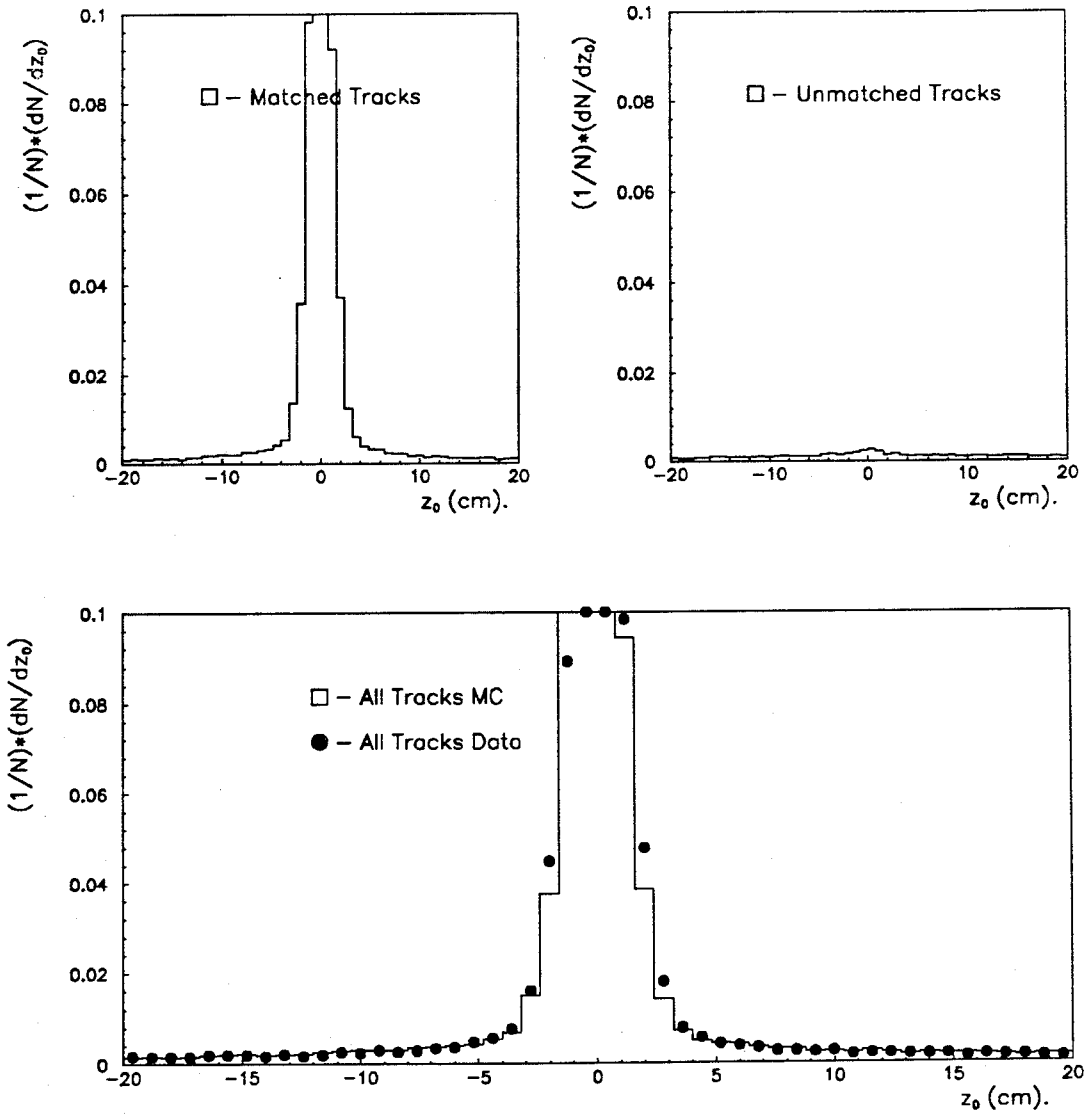

Figure 5.6: Track Extrapolation wrt the z_0 Parameter.

events whilst still retaining the majority of hadronic events. The $\tau^+\tau^-$ events also result in relatively few tracks, but generally more than the above two leptonic cases, due to their hadronic decay modes. Two photon ($\gamma\gamma$) events may also have several tracks, and either of these event types may pass the n_{ch} cut. (Here all $\gamma\gamma$ subprocesses from both the VDM and QPM have been considered. In the VDM model the Q^2 of the photons is close to the masses of the the vector mesons ρ, ω, ϕ. The photons

Cuts	Accepted	Rejected
n_{TPC}	16.59 ± 0.33	83.34 ± 0.33
$\|cos\theta\|$	75.53 ± 0.38	24.47 ± 0.38
P_t	31.45 ± 0.41	68.55 ± 0.41
$\|d_0\|$	36.66 ± 0.43	63.34 ± 0.43
$\|z_0\|$	10.29 ± 0.27	89.71 ± 0.27
All	1.13 ± 0.09	98.87 ± 0.09

Table 5.1: The Effect of Cuts on Unmatched Reconstructed Charged Tracks (percentages).

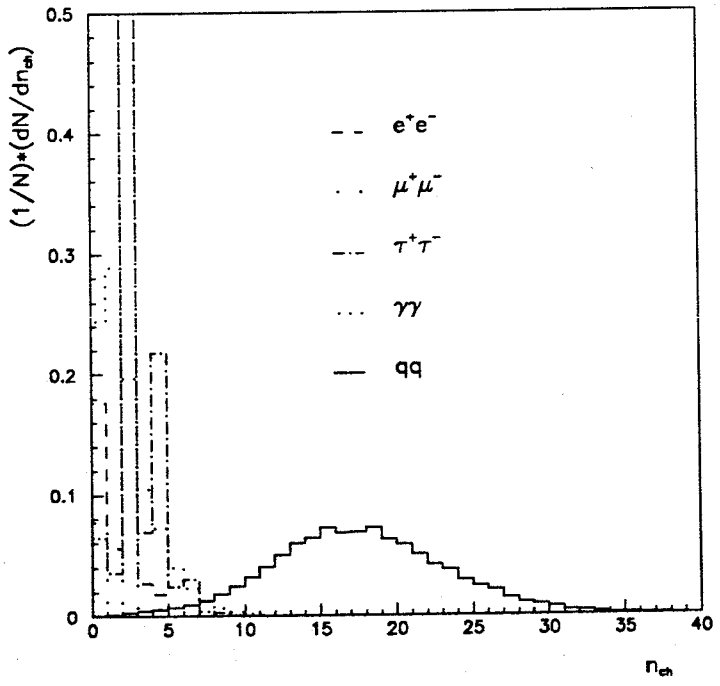

Figure 5.7: Charged Track Multiplicity.

couple directly to the vector mesons and the interaction proceeds in a similar fashion to meson-meson scattering. The QPM is valid when the Q^2 of the photons is away from the vector meson masses, i.e. large Q^2. The invariant mass of the 2γ system was $W_{\gamma\gamma} > 4GeV$ in all cases). However if we also consider the charged energy fraction E_{ch} figure 5.8 ($E_{ch} = \sum E/E_{C.M.}$ of the tracks, where the energy is determined from the TPC assuming the pion mass) and apply a cut of $E_{ch} \geq 0.15 \times E_{C.M.}$, the $\gamma\gamma$ events can be efficiently removed, as their tracks charged energy fraction is small. This is because the photons carry only a few percent of the incident e^+e^- energy. Unfortunately, the $\tau^+\tau^-$ events have a large E_{ch} consistent with hadronic events, so this cut has little further effect on this event type. Indeed, it is the $\tau^+\tau^-$ events which form the major background in hadronic events. During track selection, some good tracks are obviously rejected. Due to the high number of tracks in hadronic events, this has little effect on the n_{ch} cut. The charged energy is reduced by $\simeq 7GeV$ per event which again, considering the high charged energy fraction of these events does not seriously degrade their selection.

A final cut on the sphericity axis of the event relative to the beam axis - $35° \leq \theta_{sph} \leq 145°$ - ensures that any event is well contained within the detector volume. The selection efficiencies of the different event types upon applying each cut are summarized in table 5.2.

However, when considering the relative contributions of each event type, in addition to the selection efficiency we must also include the cross section for their initial production. The number of events selected N is then

$$N = \mathcal{L}\varepsilon_T(\varepsilon_{had}\sigma_{had} + \varepsilon_\tau\sigma_\tau + \varepsilon_e\sigma_e + \cdots) \tag{5.1}$$

$\mathcal{L}$ -Luminosity.

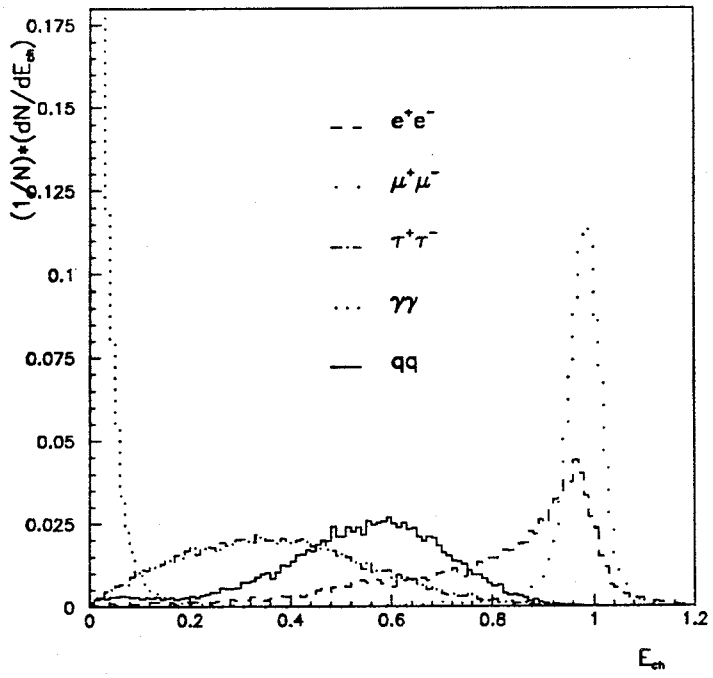

Figure 5.8: Charged Energy Fraction.

ε_T - Trigger efficiency for hadronic event types.

ε_i - Selection efficiency for event type i.

σ_i - Cross section of production for event type i.

5.4 Trigger Efficiency.

Several triggers, which may not be independent, are used for hadronic events. However, two triggers which are independent, and in conjunction successfully trigger all hadronic events are the Single Penetrating Track and the ECAL Energy triggers. The penetrating track trigger employs the ITC and HCAL and demands $\geq$ 5 ITC hits and $\geq$ 4 HCAL double layers to be fired by any single track in consistent trigger segments from each sub-detector. The ECAL energy trigger uses the wire energy in several combinations from the barrel and end caps. Either barrel $\geq 6.5GeV$, end cap $\geq 3.8GeV$ or both end

Event Type	Cuts			
	a)	b)	c)	d)
$q\bar{q}$	98.51 ± 0.09	95.94 ± 0.14	95.85 ± 0.14	74.48 ± 0.31
e^+e^-	0.04 ± 0.01	81.40 ± 0.28	0.04 ± 0.01	0.03 ± 0.01
$\mu^+\mu^-$	0.0	92.02 ± 0.19	0.0	0.0
$\tau^+\tau^-$	6.29 ± 0.17	82.74 ± 0.27	6.25 ± 0.17	5.20 ± 0.16
$\gamma\gamma$	9.18 ± 0.17	1.22 ± 0.06	0.54 ± 0.04	0.13 ± 0.02

Table 5.2: Event Selection Efficiencies Upon Applying a) Track, b) Energy, c) Track and Energy, d) Track, Energy and Sphericity Cuts.

caps $\geq 1.6GeV$. The independence of these two triggers can be utilised to calculate the trigger efficiency which has been determined from the data [21], and has been found to be

Single Penetrating track	$98.34 \pm 0.05\%$
ECAL Energy	$99.989 \pm 0.004\%$

Giving an overall combined efficiency of effectively 100%. Therefore, event losses from trigger inefficiency are negligible.

5.5 Data Corrections.

To compare experimental results with QCD theoretical predictions and other experiments, the data distributions must be corrected to account for

- Incomplete acceptance.
- Detector inefficiencies.

- Selection inefficiencies.
- Initial state radiation.
- Missing neutral particles.

To achieve this Monte Carlo events are generated and passed through GALEPH and JULIA. This data is then analysed using the same methodology and programme that is used on the real data. Then a second set of Monte Carlo data is generated with no initial state radiation. Also, any particle with $\tau < 1ns$ is allowed to decay. The two MC data sets can then be used to calculate bin by bin correction factors for the real data. The correction factor C is then

$$C = \frac{n_{mc}^{gen}}{n_{mc}^{JULIA}} \tag{5.2}$$

and

$$n_{data}^{corr} = C \times n_{data} \tag{5.3}$$

where the n_i^j are the normalized bin contents of a distribution.

Chapter 6

Data Analysis and Results

6.1 Introduction

The unambiguous identification of quark induced and gluon induced hadronic jets is not a simple task. However, its worth can not be underestimated as it would test a corner stone of QCD theory, by allowing the study of the Triple gluon Vertex, which is itself a consequence of the non-Abelian nature of QCD, and the determination of α_s via the investigation of azimuthal asymmetries at a particular energy scale. Unfortunately[1]

> *Despite a considerable amount of experimental effort, unambiguous differences between quark induced and gluon induced jets have not yet been established.*

Ideally, to identify measurable quantities which could be used to differentiate between the two jet types, one would use a pure sample of each in an identical environment. (e.g. with the same E_{cm} and detector etc.). However, when dealing with data, we can not say which parton induced a particular jet of hadrons. The problem is further compounded as many QCD predictions are made perturbatively at the parton level, but our observables are the particles produced when the partons fragment

[1] *Phys. Rev. Lett. Vol. 63 No. 17 23 September 1989*

or hadronize, where non-perturbative effects dominate and may obscure any underlying differences. Thus, variables that are fragmentation model independent should be sought, and progress has to be made with caution to avoid the pitfalls which abound in this field.

When trying to identify differences, jets of the same energy should be compared to avoid effects due purely to the energy scale of a particular jet. Also, data from e^+e^- colliders is best suited to the work as it provides a clean sample of $q\bar{q}g$ events (at $O(\alpha_s)$), in contrast to that from $p\bar{p}$ experiments where the partonic final states are less clearly defined. Two basic approaches can be employed.

1. Compare 2-jet events from one experiment with 3-jet events from an experiment at a higher centre of mass energy, such that $E_{q\bar{q}}/2 \simeq E_{q\bar{q}g}/3$. However, here almost colinear 2-jet events are being compared with symmetrical 3-jet events, which may give rise to large kinematical differences which would be superimposed on any dynamical differences. This effect is due to the different environments of the experiments and the phase space available to the jets. i.e. we have 2-jet events fragmenting into 4π of solid angle at one energy, compared with 3-jet events into 4π at another. This method can also be used with the same detector if two data sets are obtained at differing E_{cm} but the above problem still remains.

2. Compare jets from one detector at one centre of mass energy. Here a sample of 3-jet events is produced and a subset is selected with an underlying symmetry. However this requirement results in very low statistics with this approach. A remedy is to use semi-symmetrical events where the jet opening angles lie in the range $100° \leq \theta_{ij} \leq 140°$ rather than the stringent requirement of $\theta_{ij} \simeq 120°$. This improves the statistics but can result in energy differences $E_{highest} \simeq 1.4 \times E_{lowest}$ between the jets, which again could lead to kinematical effects.

The large amount of data collected by the *ALEPH* experiment helps to improve statistics and thus prompts the choice of the second approach in the following analysis.

6.2 Quark and Gluon Jet Differences.

In QCD gluons carry a larger colour charge than quarks and are therefore more likely to radiate via bremsstrahlung. This is expected to result in softer jets which would be observed through a higher particle multiplicity, a softer particle momentum spectrum and broader jets. [33,34]

QCD predicts that the ratio R of average multiplicities of gluon jets to quark jets is 9/4 [35,36] which is effectively a ratio of the branchings shown.

$$R = \frac{< n >_{gg}}{< n >_{q\bar{q}}} = \frac{g \longrightarrow gg}{q \longrightarrow qg} \tag{6.1}$$

This is also known as the the ratio N_C/C_F, where the colour factor C_F determines the strength of the coupling of a gluon to a quark or antiquark; and N_C describes the strength of the splitting of a gluon into two further gluons. Thus, this ratio is a direct measure of the relative strength of the Triple Gluon Vertex (TGV) compared to the $q-g$ coupling.

It should be noted however, that this ratio is calculated at the parton level for pairs of colinear gg and $q\bar{q}$ jets at infinite (asymptotic) energy and at leading order. Finite energy corrections of order $\sqrt{\alpha_s}$ (i.e. proportional to $ln^{-\frac{1}{2}}(Q/\Lambda)$), heavy quark effects and 2nd. order calculations reduce this ratio to $\simeq$ 1.3-1.6 at present energies [37,38]. However, if this effect is maintained through fragmentation, its effects should still be inherent at the hadron level.

The remainder of this chapter deals with the search for differences which may be evident in data from $e^+e^- \longrightarrow$ 3-jet events collected with the ALEPH detector. In section 6.3 the terminology and parameters used in the analysis are defined. This is

followed by an investigation of the ratio of equation 6.1 at LEP energies, as this is the foundation of the expected differences between the jet types.The outcome of the study is summarized in section 6.4. Section 6.5 describes the variables considered and the expectations of their values when looking for differences, and presents the experimental results. The results are then discussed and compared with other works in section 6.6 and concluded in section 6.7

6.3 Terminology and Event Definition.

Many parameters and variables are required as a frame of reference and definition for the events. The most salient are briefly discussed below.

6.3.1 Global Event Selections.

The selection of hadronic events has been previously covered in chapter 5. However, the main features are outlined below for convenience. A hadronic event must have at least 5 good charged tracks, whose summed energy exceedes $0.15 \times \sqrt{s}$. The sphericity axis of the event is also required to lie within the range $35° \leq \theta_{sph} \leq 145°$ to ensure that the event is well housed in the detector. A good charged track has

- $n_{TPC} \geq 4$
- $|cos\theta| \leq 0.95$
- $P_t \geq 0.2GeV$
- $|d_0| \leq 2.0cm$
- $|z_0| \leq 5.0cm$

Good neutral clusters are required to have

- $|cos\theta| \leq 0.95$
- $E \geq 0.3GeV$

The neutral particles are not associated to a charged track (i.e. isolated clusters) so the problem of double counting energy is not met. The charged track energy is calculated assuming the pion mass and neutral particles are taken to be massless. Neutral particles are included in the determination of some of the variables later in the analysis and in the jet clustering process. This helps to ensure a more authentic jet direction vector is recreated. Particles failing these requirements are not included in any further stages.

6.3.2 The Event Plane.

An event plane is defined in momentum space by using the eigenvalues of the sphericity tensor of equation 6.2

$$T_{\alpha\beta} = \frac{\sum P_{i\alpha} P_{i\beta}}{\sum P_i^2} \tag{6.2}$$

$P_{i\alpha}$ - momentum of the i_{th} particle.

α - x, y, z component of momentum.

The tensor is constructed and diagonalized for each event such that its normalized eigenvalues Q_1, Q_2, Q_3, ($Q_1 < Q_2 < Q_3$ with $Q_1 + Q_2 + Q_3 = 1$) correspond to the three orthogonal eigenvectors q_1, q_2, q_3 of the momentum elipsoid. The vectors q_2, q_3 define the event plane and q_3 is the sphericity axis. The normal to the plane is the direction of the vector q_1.

6.3.3 Jet Definition.

Any jet analysis should start with a good jet definition [39]. A good jet definition is one that

a) - is insensitive to hadronization and must be able to combine final state hadrons to give the best possible measure of the initial partons.

b) - is defined at any order of perturbation theory. One must decide when two partons count as two jets and when they count as one. It is this treatment of the finite jet size which renders the jet cross section finite at all orders of perturbation theory.

c) - is simple to implement both theoretically and experimentally.

In e^+e^- annihilation, simple infra-red safe jet finding algorithms are provided by clustering routines based on an invariant mass cut off. To this end the clustering algorithm originally introduced by the JADE group [40] is employed. Here, the scaled mass squared (scaled by the visible event energy as opposed to the centre of mass energy)

$$y_{ij} = \frac{m_{ij}^2}{Evis^2} \tag{6.3}$$

where

$$m_{ij}^2 = 2E_iE_j(1 - cos\theta_{ij}) \tag{6.4}$$

is calculated for each pair of particles i, j in the event. If the smallest of the y_{ij} values is less than a parameter y_{cut}, the two particles are merged into a pseudo-particle. Several techniques exist for merging the particles, each with its own merits, but here the Lorentz invariant E-scheme has been used where $P_{ij}^{\mu} = P_i^{\mu} + P_j^{\mu}$. Normally the merging process would be iterated until all of the y_{ij} values exceeded y_{cut}. The resulting number of pseudo-particles being the jet multiplicity. However, the algorithm was modified so that a prespecified value of y_{cut} was not required, and merging continued until only three jets remained. Section 6.3.5 describes how a symmetric three jet sample was selected and background events were removed.

6.3.4 Jet Energies.

Two measures of the energy of a jet can be employed. These are the visible energy E_{vis} and the reconstructed energy $E_{jetaxis}$ defined by equations 6.5 and 6.6.

$$E_{vis} = \sum_{i=1}^{n_j} E_{ij} \tag{6.5}$$

n_j - number of particles in jet j. $(j = 1, 2, 3)$

E_{ij} - energy of the i_{th} particle in jet j.

The particle energies assume the pion mass for charged particles and the photon mass for all neutrals.

The second method uses the direction of the jet axes returned from the clustering algorithm (i.e. the vector sums of the particle momenta within each jet), and is energy and momentum conserving.

$$E^x_{jetaxis} = \frac{sin\theta_{yz}}{sin\theta_{12}sin\theta_{23}sin\theta_{31}} \cdot \sqrt{s} \tag{6.6}$$

The axes are projected into the event plane, and the angles between the axes are determined. i.e. θ_{yz} - angle between jets y and z in the event plane. It should be noted that this procedure is only strictly applicable in the case of three massless jets. However, it does provide a very close approximation to the jet energy, and is the value used to define the jet's energy scale. The jet with the lowest value of $E_{jetaxis}$ is assumed to be the gluon induced jet.

6.3.5 Mercedes or 'Symmetric' Events.

After the clustering algorithm had been applied, Symmetric events were selected based on the condition that the angles between the jet axes satisfied the requirement

$100° \leq \theta_{ij} \leq 140°$. Additionally, each jet was required to contain at least 4 particles (charged + neutral). These preconditions effectively reduce the background from $\tau^+\tau^-$ events to zero.

It can be seen that the approach employed by using the modified clustering routine will always result in the production of 3-jet topologies, even when in reality the nature of the event is not a genuine 3-jet topology. This occurs when the merging stops at three jets but should be allowed to continue, or when merging proceeds too far in events where the number of jets is greater than three.

An investigation was made to determine the number of non 3-jet events in the sample. Figure 6.1 shows the invariant mass (y) distributions for all data ('all') and the symmetrically selected sample, when events are force clustered into either 3 or 2 jet configurations. The invariant mass is that at which the event goes from a 4-jet to 3-jet (4-3) topology, or a 3-jet to 2-jet (3-2) topology. The distribution for each sample is normalized to unit area.

In the 3-2 case, the symmetric events are clearly separated from the 'all' data. This is because in 'all' events, many events really have a 2-jet structure and are on the 3-2 borderline when merging terminates. However, in the symmetric sample, the jets are both well defined and separated, and merging into two jets results in a much larger jet invariant mass. Also, the 4-particle requirement reduces events where although the separation is good, one or two isolated high energy tracks imitate a jet.

In the 4-3 case the difference is less clear. However, it can be seen that the symmetric events lie in an invariant mass range typically $y \simeq 0.01 - 0.05$. (Fairly standard values of invariant mass used for for selection of three jet events with the conventional JADE algorithm are $y = 0.02 - 0.03$ [41,42,43]). To further study this region, the symmetric event sample was reclustered with the conventional JADE algorithm using invariant mass cuts of $y_{cut} = 0.02$ and $y_{cut} = 0.04$. Figure 6.2 shows the number of jets produced in each case from 'all' data and the symmetric events (which are superimposed on the

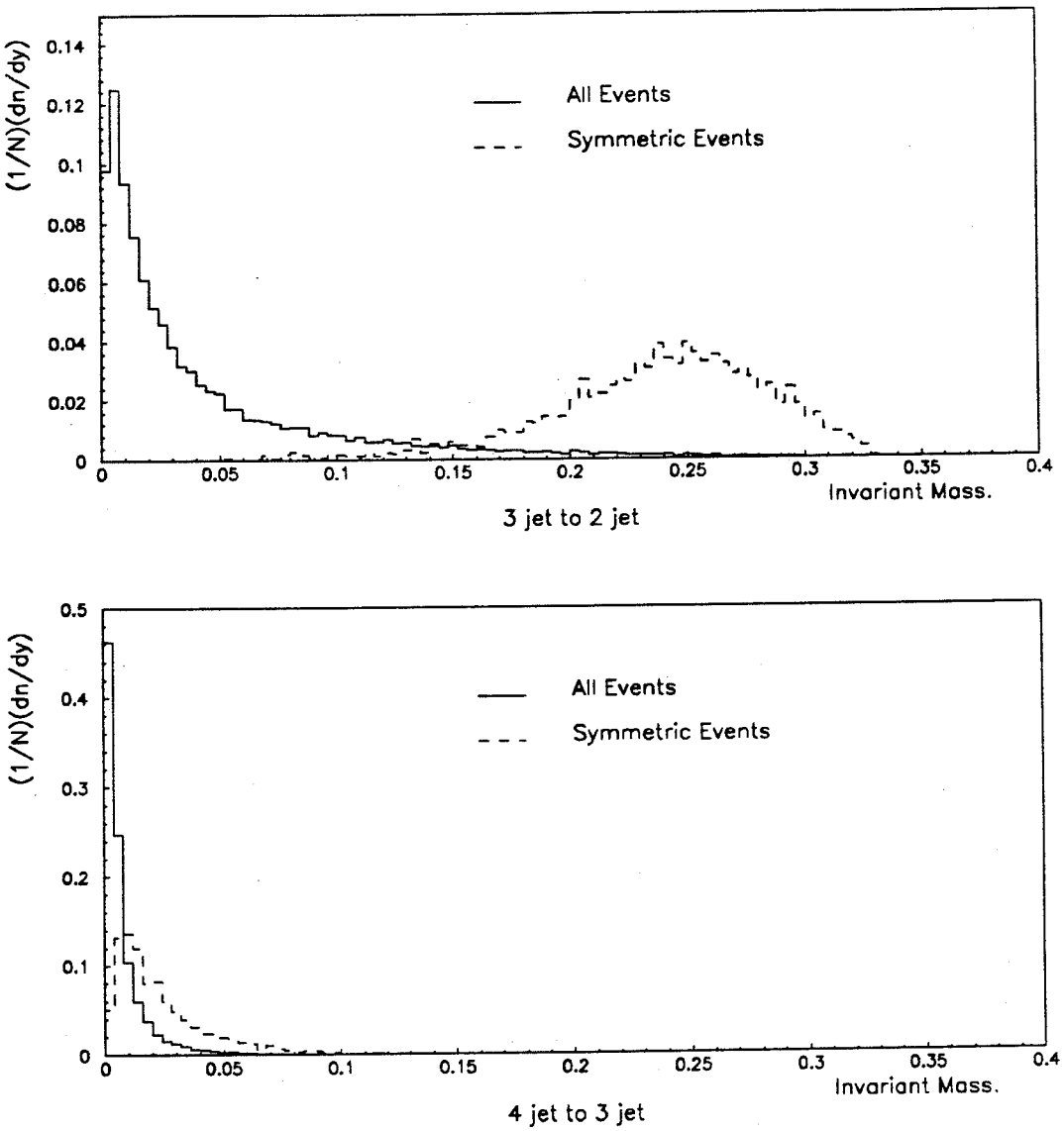

Figure 6.1: Normalized invariant Mass (y) Distributions when Events Change from 3-jet to 2-jet or 4-jet to 3-jet Topologies.

'all' events). In these regions there are clearly no 2-jet events in the symmetric sample, but a residue of 4-jet events is present. However, the number of jets in an event is never clearly defined and is in any case only a function of the invariant mass cut used in the jet finding routine. i.e. by choice of invariant mass cut, we can let the same event have

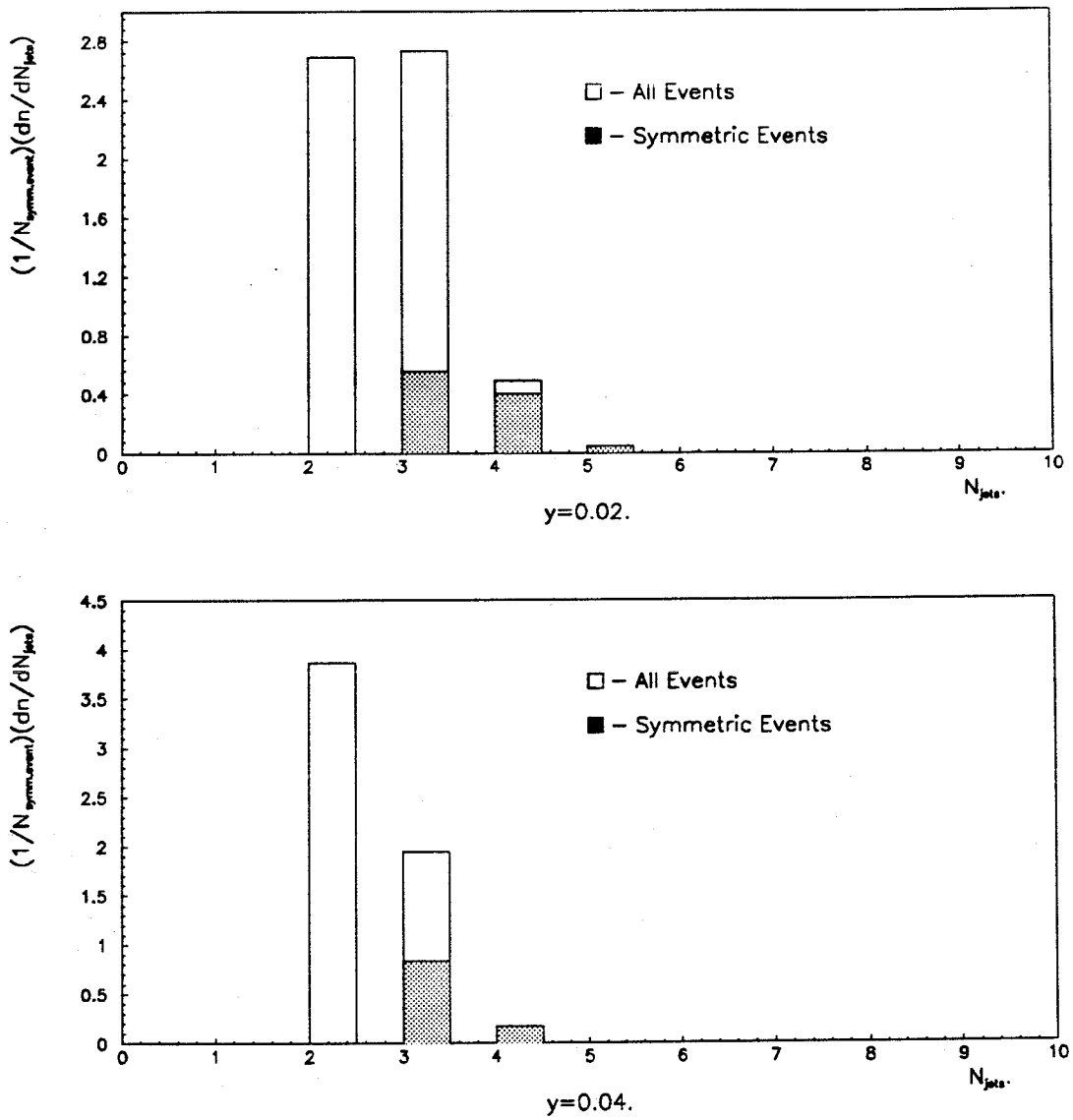

Figure 6.2: The Number of Jets Produced from 'All' Data and the Symmetric Sample Using a Fixed y_{cut} as Shown.

many or few jets, regardless of its true nature.

To determine any possible effect from 4-jet contamination, the symmetric data was reclustered using the two fixed invariant masses above, and events where three jets were produced were selected. i.e. non 3-jet events removed. These were then analysed in an identical manner to the force clustered symmetric sample for certain variables, and the

results compared to estimate any residual effects.

6.4 Colour Charge Effects at LEP.

The ratio R of equation 6.1 has been studied to ascertain the effect that may be visible at LEP. This work was carried out using events generated by the *LUND JETSET* programme (*version* 7.3) with the parton shower fragmentation scheme. Several variations of initial parton configuration, branching ratios and parton identification methods were used. The results are summarised in tables 6.1 and 6.2. The analysis details and terminology are outlined below.

1. All events were generated at $E_{cm} = 91.2GeV$.
2. A three parton $q\bar{q}g$ mercedes initial configuration was formed, where each parton had $E_{parton} = E_{cm}/3$
3. In the conventional $q\bar{q}$ initial configuration each parton had $E_{parton} = E_{cm}/2$
4. Two models were employed. The QCD model used all default settings of the event generator (i.e. shower parameters etc.), whereas in the Toy model, the branching probability $g \longrightarrow gg$ was set equal to $q \longrightarrow qg$. Then the only difference between quark and gluon branchings was the Altarelli-Parisi z-splitting Kernel [44,45]. The splitting kernels define how the momentum of a parent parton is divided between its daughters after a branching has occured.
5. After the parton shower had terminated (prior to any hadronization) the final state partons were clustered into three jets using the modified JADE algorithm previously described, and symmetric events were selected. However, no requirement upon the number of tracks within a jet was made.
6. It should be noted that although the $q\bar{q}g$ configurations were initially in a perfect Mercedes state ($\theta_{ij} = 120°$), due to the fact that the partons aquire mass during

the shower and the effects of clustering, this is not necessarily the final case. For this reason this event class was also checked for the symmetry requirement.

7. After clustering the partons could be assigned to a jet in two ways.

   a) - Association - where the jet to which the parton is assigned in the clustering process is used.

   b) - Direction - where the jet axes produced by the clustering process are used. The partons are then reassigned to the jet to whose axis they are closest. This is more likely to affect softer particles which are merged first in the clustering routine.

8. Each parton was then assigned a parton number such that $q = 1$, $\overline{q} = -1$ and $g = 0$.

9. The sum of parton numbers within each jet was computed to produce a jet number. Only events where the three jets had numbers 1, -1, 0 were considered, and each jet was then labelled according to its jet number.

10. Additionally, the parton closest to the jet axis was also used to identify the jet, (this assumes that the parton nearest to the axis actually belongs to the jet in question), as its history could be traced back to a parent parton. This could only be employed with the $q\overline{q}g$ events, as there is no initial state gluon in the $q\overline{q}$ events.

11. The ratio of multiplicities R was determined as $R = (< n_g >)/(< n_{q'} >)$, where $< n_g >$ is the mean gluon jet multiplicity, and $< n_{q'} >$ the mean quark jet multiplicity, is taken as the average of the q and $\overline{q}$ multiplicities.
    i.e. $< n_{q'} >= (< n_q > + < n_{\overline{q}} >)/2$.

12. The ratios shown in tables 6.1 and 6.2 are for all 3-jet events and those passing the symmetry cut. Before progressing further, some explanation and clarification of the results should be given.

Parton Assign.	Direction				Association			
Model	Toy		QCD		Toy		QCD	
Jet Config.	All	Symm.	All	Symm.	All	Symm.	All	Symm.
$R = \frac{<n_g>}{<n_q/>}$	1.10	1.12	1.32	1.37	1.13	1.14	1.40	1.46

Table 6.1: Multiplicity Ratios for $q\bar{q}g$ Initial Parton Configurations.

Parton Assign.	Direction				Association			
Model	Toy		QCD		Toy		QCD	
Jet Config.	All	Symm.	All	Symm.	All	Symm.	All	Symm.
$R = \frac{<n_g>}{<n_q/>}$	0.85	1.13	0.94	1.39	1.07	1.17	1.19	1.48

Table 6.2: Multiplicity Ratios for $q\bar{q}$ Initial Parton Configurations.

After selecting symmetrical events the samples are fairly pure 3-jet events. These consist of two quark jets and a gluon initiated jet formed by a 'hard' gluon emission in the $q\bar{q}$ case, or the already present gluon in the $q\bar{q}g$ case. However, due to the nature of the clustering algorithm used, the $q\bar{q}$ sample will contain fake three jet events which are really non 3-jet topologies as described in section 6.3. Therefore, the results for the $q\bar{q}$ events in the four 'all' final states can be assigned very little credibility. However, due to the underlying initial symmetry and genuine 3-jet nature of the $q\bar{q}g$ events, this problem is not encountered and very few final state events are rejected due to lack of symmetry. This is reflected by the similarity of the ratios for both the 'all' and 'symm.' final states in the $q\bar{q}g$ events.

In the Toy model calculations, the branching strengths $g \longrightarrow gg$ and $q \longrightarrow qg$ were the same. However, the difference of the Altarelli-Parisi z-splitting kernels is still

expected to introduce a difference in jet multiplicities [46]. This is determined from the ratio of the integrated kernels (gg/qg) and gives a value $22/18 = 1.22$. Therefore the mean gluon jet multiplicity is expected to be higher by a factor 1.22. Also, even in the 'symm.' final states the energies of the jets were typically $E_q \simeq 33GeV$ and $E_g \simeq 25GeV$ in the $q\bar{q}$ sample but slightly closer in the $q\bar{q}g$ data. Multiplicity is related to energy via a $\ln(E)$ dependence and this would tend to reduce the ratio, as $\ln 25/\ln 33 = 0.92$. Therefore the ratios from the TOY model are expected to exceed unity by an amount $1.22 \times 0.92 = 1.12$. In the Toy model the values from both event types and are typically $\simeq 1.1$ (the statistical error is typically $\simeq 0.01$) which is consistent with expectation when allowing for jet energy and splitting function effects.

In the QCD model the ratio is expected to exceed that of the Toy model as the $g \longrightarrow gg$ branching probability is greater than that of the $q \longrightarrow qg$. The results for the 'symm.' final states from both the $q\bar{q}$ and $q\bar{q}g$ data suggests a ratio of multiplicities $\simeq 1.4-1.5$, which is in good agreement with the value quoted in section 6.2 ($\simeq 1.3-1.6$). Also the close similarity between the $q\bar{q}$ and $q\bar{q}g$ results enforces the validity of the formation and selection methods for 3-jet events.

In conclusion, the difference in gluon jet and quark jet multiplicities due to the higher colour charge carried by the gluon yields a ratio $\simeq 1.4 - 1.5$ at LEP energies. This is obviously lower than the naive expectation of 9/4 but is in agreement with the theoretical parton level prediction. Therefore, at least at the parton level, there is an underlying difference between the jet types.

6.4.1 Energy Ordering of Jets.

In the previous parton level Monte Carlo study, two definite methods of jet identification were employed, but in the analysis of data, no such mechanisms exist. When considering the data, jet identification was established via an energy ordering approach, where the lowest energy jet of a 3-jet event is assumed to be gluon initiated. The parton level

Event Type	Jet-1	Jet-2	Jet-3
'All'	3	15	82
Symmetric	19	28	53

Table 6.3: Percentage of Cases Where Each Jet is Gluon Initiated.

work was used to estimate the efficiency and sample purity that this technique provides, by identifying the jets as described previously when they were energy ordered. The percentage of cases where each jet in $q\bar{q}$ events was gluon initiated is shown in table 6.3. (Jet-1 being the highest energy and jet-3 the lowest). In 'all' events the method is obviously effective as the three jets have a large energy range and jet-3 usually has a much lower energy than jets 1 or 2. However, in symmetric events, the three jet energies are much closer which results in more quark 'interference' in the lowest energy jet.

Although these values were calculated at the parton level, they should be equally valid at the hadron level, since the difference between parton-jet direction and hadron-jet direction is small, compared to the overall jet separation in symmetric events.

6.5 Results.

Data collected by the Aleph detector during the 1991 running period has been used in the analysis. This amounts to 228,345 $Z^0 \longrightarrow$ hadronic events at the Z^0 resonance, corresponding to an integrated luminosity of 7630 nb^{-1}. However, the global selections previously described in conjunction with the Symmetric three jet requirement reduce this to 2724 events, with a further reduction to 2635 events by demanding the presence of at least four particles in each jet. The results presented have been corrected for detector and track selection inefficiencies, and the effects of initial state radiation as

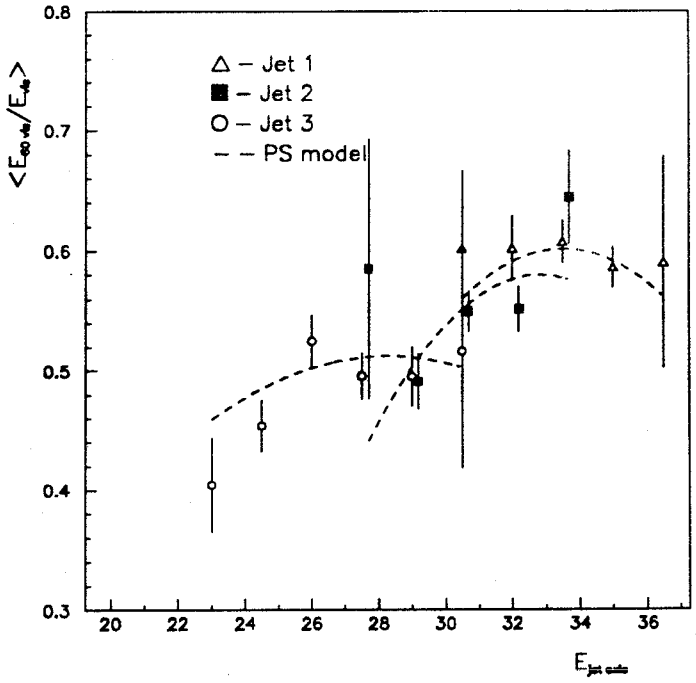

Figure 6.3: Mean Core Energy Fraction Scaled by E_{vis} as a Function of $E_{jetaxis}$.

defined in chapter 5. Additionally, all particles with lifetimes $< 10^{-10}s$ were allowed to decay in the generator level MC. i.e. K_s^0, Λ^0, Ξ^0, Ξ^+, Σ^+, Σ^-, Ω^-. The number of Monte Carlo events used for this purpose was commensurate with the data sample. In the following plots, the data point for each energy bin denotes the mean value $< x >$ of the distribution within that energy range. The error is statistical only and is defined $e = \sigma_x/\sqrt{n}$. Interested parties should refer to appendix A for more details. The PS model is shown by a dashed line for each of the three jets, and is the value of n_{MC}^{gen} as defined in chapter 5. Also, it should be noted that the jet 2 values are offset by +0.2 *GeV* to ensure visibility of the data points and error bars.

6.5.1 Core Energy Fraction.

The core energy fraction is defined as the fraction of a jet's visible energy that is contained in a cone of half angle $60°/\sqrt{E}$, coaxial with the jet axis. The $\sqrt{E}$ scaling is motivated by the expectation that the widths of the jets should decrease with increasing energy [47,48]. The separation of an event into a certain number of jets is ambiguous as

a) - In a particular event it may be equally correct to identify particles as belonging to one jet, two jets, or more, as a jet often has substructure consisting of further jets.

b) - Due to colour coherence, soft particles do not belong to any particular jet, but have emission properties dependent on all jets in the event.

Collimation of the QCD cascade around the parent parton becomes stronger as the parton energy increases. Moreover, the collimation of energy flux grows more rapidly compared to multiplicity flow. Therefore at asymptotically high energies, each event should clearly posses the geometry that reflects the topology of the partons participating in the interaction. While the hard component of a hadron system (a few hadrons with energy fraction $z \simeq 1$) determine the partonic skeleton of an event, the soft component (the remainder of the hadrons with $z \ll 1$) forms the bulk of the multiplicity. Thus, the energy spectrum depends not on the jet energy, but the hardness of the process producing the jet, and although multiplicity has a $\ln(E)$ dependence, it is the hardness of the leading partons that introduces the $\sqrt{E}$ factor.

The angle can be scaled by $E_{jetaxis}$ or E_{vis} with the corresponding core energies denoted by E_{60axis} and E_{60vis}. Both charged and neutral particles are used when calculating the core energy, and their energies added to it if $\theta_{ij} \leq 60°/\sqrt{E}$. ($\theta_{ij}$ - angle between a particle and its jet axis). The core fractions are shown in figures 6.3 and 6.4.

$$f_{60x} = \frac{E_{60x}}{E_x} = \frac{1}{E_x}\sum_{i=1}^{n} E_i\left(\theta_{ij} \leq \frac{60^\circ}{\sqrt{E_x}}\right) \tag{6.7}$$

The sum runs over all particles in a particular jet and x is either vis or $axis$.

If as expected gluon jets are broader than quark jets at a particular jet energy, then the particles within the jet will be dispersed over a wider angular range. The core fraction examines any differences between the energy inside a central cone around the jet axis. However, jets are also expected to become more collimated with increasing energy, which in turn would lead to a rise in the core fraction of higher energy jets, if the cone size was not reduced accordingly. Thus, the higher energy quark jets would appear to have a larger core fraction simply due to energy effects. This is the reason for introducing the scaling factor for the angle of the cone considered. If the scaling effectively compensates for the energy narrowing of the jets, then a ratio of the gluon jet core fraction to the quark jet core fraction should be less than unity, and entirely due to the original nature of the jets. However, if the scaling is not valid, its effect would depend on whether it over or under compensated for the jet narrowing with increasing energy.

If the scaling factor is too small and under compensates, the cone will decrease too slowly. This would increase the core fraction as the jet energy increased, since the narrowing jet would introduce more energy into the central region. Conversely if the scaling is too large and over compensates, the cone will decrease too fast and subsequently decrease the core fraction as the jet energy increases. This is because the angle would be converging faster than the jet and would therefore exclude energy from the central region. Under compensating would increase any difference in core fractions between the lower and higher energy jets, whereas over compensation would decrease the difference. (In the symmetric sample, the scaled core angle was typically in the range $10^\circ - 12^\circ$). Therefore, it is important to ascertain the effect of the scaling factor.

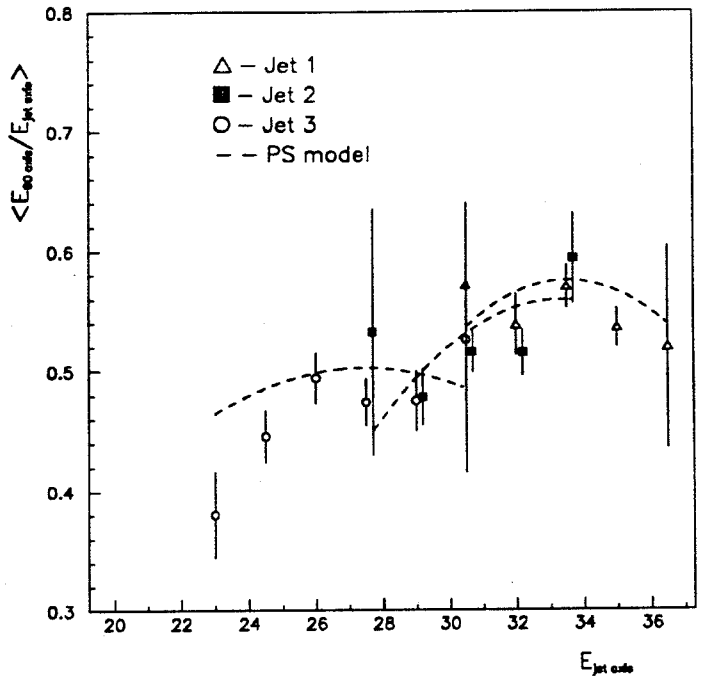

Figure 6.4: Mean Core Energy Fraction Scaled by $E_{jetaxis}$ as a Function of $E_{jetaxis}$.

An experimental determination of jet width is difficult due to the fact that the jet structure is dependent on the jet forming algorithm. Soft particles in the outer region of a jet are particularly susceptible to misassignment, and as previously mentioned, tend not to belong to one particular jet. A common definition of jet width (that used in the theoretical reasoning above) is the angle in which a given fraction of the jet's energy lies. However, an accurate determination of this value requires pure samples of quark and gluon jets.

In order to study the effect of the scaling factor, the core fraction was also examined using the two scaling factors outlined below.

i) - An unscaled fixed cone of half angle 10° for all jet energies (denoted as f_x^{fix10}) which acts as an under compensating factor, as the angle is fixed and does not decrease with increasing jet energy.

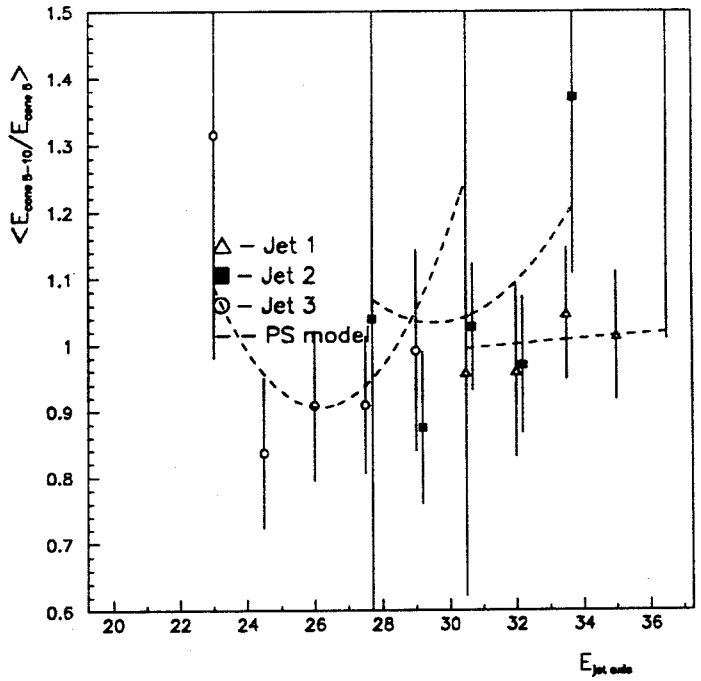

Figure 6.5: Mean Cone Energy Fraction as a Function of $E_{jetaxis}$.

ii) - A more highly scaled factor where the angle is scaled by $0.2E$ (denoted as $f_x^{20\%}$). Although not a power of E, this doubles the rate of decrease of the cone (compared to $\sqrt{E}$) and acts as an over compensation measure. (In this case the scaled angle is typically $8.33° - 12°$).

Also, as this variable was thought to be most susceptible to effects from non-three jet event contamination as described in section 6.3.5, the core fractions were calculated for 3-jet events produced by the JADE clustering algorithm using invariant mass cuts $y_{cut} = 0.02$ and $y_{cut} = 0.04$, denoted as f_{60x}^{y} (where $y = 0.02, 0.04$).

The results from the different scaling and fixed y_{cut} analyses are summarised in tables 6.6 and 6.7 and discussed in section 6.6.

6.5.2 Cone Energy Fraction.

This is a similar quantity to the core fraction above. However, in this case two cones of half angles 5° and 10° are defined. Again the cones are coaxial with the jet axes but here, no compensation for jet narrowing with jet energy is made, and the cones are not scaled in this case. The ratio of energies inside the two cones is then defined

$$f_{cone5-10} = \frac{E_{cone5-10}}{E_{cone5}} = \frac{E(5° < \theta_{ij} \leq 10°)}{E(\theta_{ij} \leq 5°)} \tag{6.8}$$

The results can be seen in figure 6.5 but note should be made of the large error bars attributed to each point. Again both charged and neutral particles were considered.

Without any scaling to compensate for the jet narrowing associated with increasing jet energy, higher energy jets should have a greater fraction of their total energy concentrated around the jet axis. So as the jet energy increases the cone fraction decreases (as the denominator E_{cone5} increases). Conversely, as the jet energy decreases, the cone fraction should increase. Additionally, if the gluon jets are broader, this should also contribute positively to the cone fraction as less energy is housed in the range covered by E_{cone5}. Therefore, if any effect is due only to increasing jet energies, the outcome would be a linear decrease of the cone fraction with increasing jet energy. However, the expected jet broadening due to increased gluon radiation superimposed on this effect should produce an additional effect for jet-3 in any smooth energy related decrease.

6.5.3 Transverse Momentum to Jet Axis.

The sum of the transverse momentum to the jet axis (P_t) of all charged particles was calculated and then averaged over the number of charged tracks n in the jet. Thus

$$< P_t - JetAxis >= \frac{1}{n}\sum_{i=1}^{n} P_t^i \tag{6.9}$$

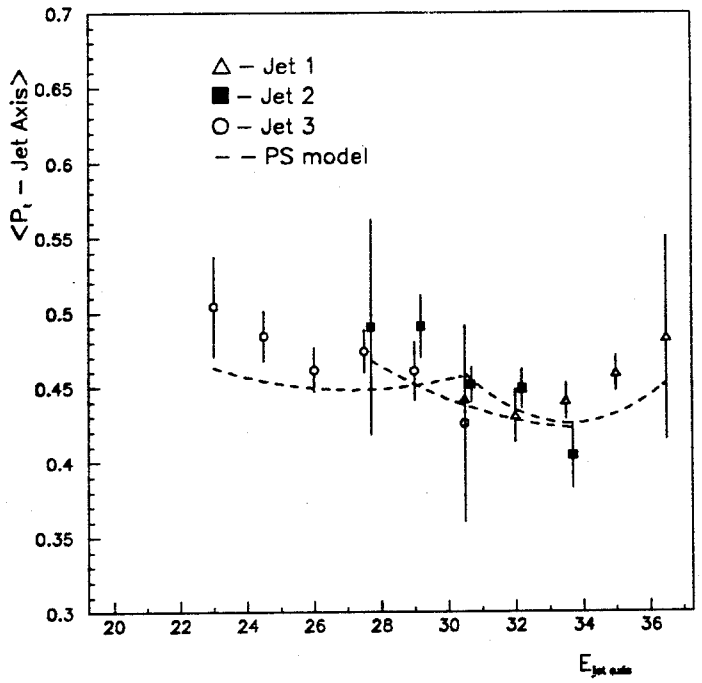

Figure 6.6: Mean Charged Track Transverse Momentum P_t to the Jet Axis as a Function of $E_{jetaxis}$.

Both this variable and the following two are related via the same underlying causal effect. If the parton multiplicity in gluon jets is greater than that of quark jets by the ratio of equation 6.1 as previously discussed in sections 6.2 and 6.4, then assuming that the parton and hadron multiplicities are related via a phenomenological energy independent parameter, we would expect the gluon jets to have higher particle multiplicities. The increase in multiplicity due to increased gluon bremsstrahlung also results in a softer longitudinal momentum spectra and an increase in transverse momenta. The $q\bar{q}g$ events are planar and as fragmentation occurs, the hadrons should on average be uniformally distributed in azimuth about the partons' axes. However, if fragmentation occurs via the string effect, as is believed, then the majority of the transverse momentum of the hadrons will be in the event plane, with a much smaller fraction out of the plane. Therefore, momentum out of the plane P_{out} should be quite sensitive to any

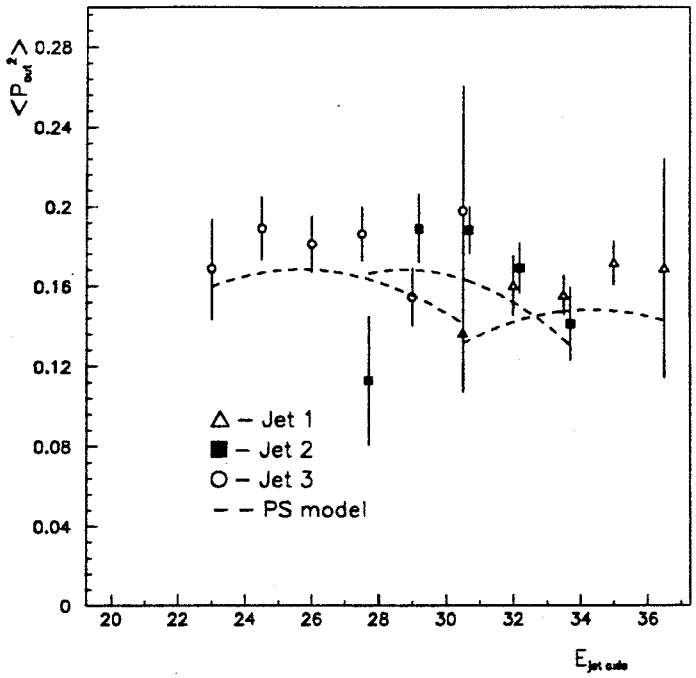

Figure 6.7: Mean of Squared Charged Track Momentum Out of the Event Plane as a Function of $E_{jetaxis}$.

differences between the jet species, and the squaring of P_{out} increases the sensitivity further. Thus, the expectation for all three variables would be larger for gluon jets than those of quarks. The data are shown in figures 6.6, 6.7 and 6.8.

6.5.4 Momentum Out of the Event Plane.

A similar variable to the transverse momentum above, except that the sum was over the component of the charged particles' momenta out of the event plane (P_{out}). (i.e. the momentum component of the particle parallel with the event plane normal q_1). Additionally, each component was squared before summing.

$$< P_{out}^2 >= \frac{1}{n} \sum_{i=1}^{n} (P_{out}^i)^2 \tag{6.10}$$

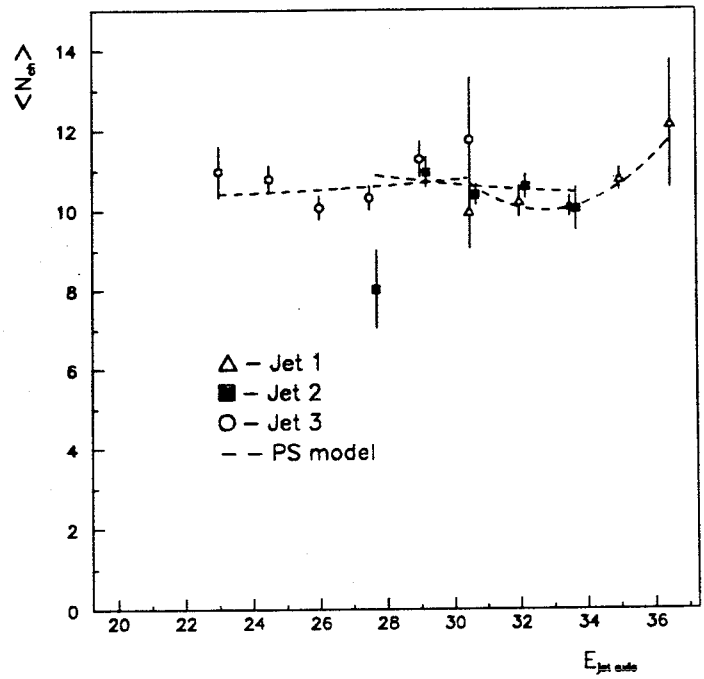

Figure 6.8: Mean Charged Track Multiplicity as a Function of $E_{jetaxis}$.

6.5.5 Charged Track Multiplicity.

The charged multiplicity of each jet was examined with the results shown in figure 6.8. The Multiplicity is calculated simply as the number of charged tracks in each jet.

6.5.6 Variable Comparisons.

Some of the variables considered and shown in the plots do not exhibit dramatic differences between the three jets. Therefore, a mathematical comparison is required. The two methods used are outlined below.

1. For a particular jet, the average value of the variable is calculated across all energy bins (6 bins for jet-3, 5 bins for jets 1 and 2).

Variable	Jet 1	Jet 2	Jet 3
f_{60axis}	0.55 ± 0.01	0.51 ± 0.01	0.47 ± 0.01
f_{60vis}	0.60 ± 0.01	0.55 ± 0.01	0.49 ± 0.01
$f_{cone5-10}$	1.02 ± 0.06	0.99 ± 0.06	0.92 ± 0.06
$P_t - JetAxis$	0.447 ± 0.008	0.451 ± 0.007	0.472 ± 0.007
P_{out}^2	0.162 ± 0.006	0.172 ± 0.007	0.177 ± 0.007
N_{ch}	10.4 ± 0.2	10.5 ± 0.2	10.5 ± 0.2

Table 6.4: Average Values of Variables for the Three Jets Over All Energy Bins.

Variable	$< r_{32} >= \left\langle \frac{x_3}{x_2} \right\rangle (26.75 \leq E_{jetaxis} \leq 31.25 GeV)$
f_{60axis}	0.98 ± 0.06
f_{60vis}	0.98 ± 0.06
$f_{cone5-10}$	1.13 ± 0.20
$P_t - JetAxis$	0.94 ± 0.05
P_{out}^2	0.87 ± 0.10
N_{ch}	1.06 ± 0.05

Table 6.5: Average of Ratios of Jet-3 to Jet-2 Values in Each Overlapping Energy Bin ($26.75 \leq E_{jetaxis} \leq 31.25 GeV$).

2. In the energy range $26.75 \leq E_{jetaxis} \leq 31.25 GeV$, three energy bins of jet-2 and jet-3 overlap. For each of the three bins the ratio $r_{32} = x_3/x_2$ was determined, and then averaged over the three bins to give $< r_{32} >$.

The values determined by method 1 are listed in tables 6.4 and 6.6, and those from method 2 in tables 6.5 and 6.7.

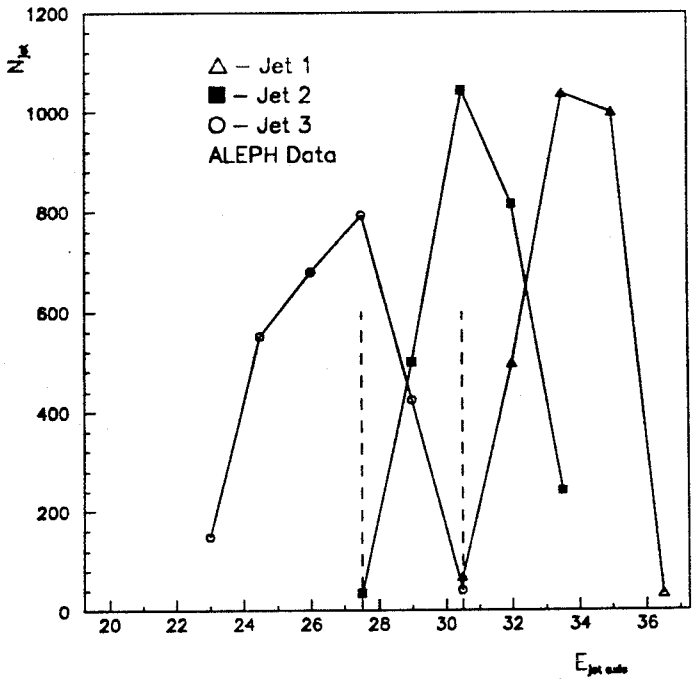

Figure 6.9: The Frequency of the Three Jets in the Energy Bins Defined by $E_{jetaxis}$.

Variable	Jet 1	Jet 2	Jet 3
f_{axis}^{fix10}	0.54 ± 0.01	0.49 ± 0.01	0.41 ± 0.01
$f_{axis}^{20\%}$	0.50 ± 0.01	0.48 ± 0.01	0.46 ± 0.01
$f_{60vis}^{y=0.02}$	0.68 ± 0.01	0.62 ± 0.01	0.55 ± 0.01
$f_{60vis}^{y=0.04}$	0.63 ± 0.01	0.58 ± 0.01	0.50 ± 0.01
$f_{60axis}^{y=0.02}$	0.65 ± 0.01	0.61 ± 0.01	0.54 ± 0.01
$f_{60axis}^{y=0.04}$	0.60 ± 0.01	0.55 ± 0.01	0.49 ± 0.01

Table 6.6: Average Values of Variables for the Three Jets Over All Energy Bins for Events Selected with a Fixed Invariant Mass (y_{cut}) or Different Energy Scaling.

Variable	$< r_{32} >= \left\langle \frac{x_3}{x_2} \right\rangle (26.75 \leq E_{jetaxis} \leq 31.25 GeV)$
f_{axis}^{fix10}	0.97 ± 0.06
$f_{axis}^{20\%}$	0.99 ± 0.07
$f_{60vis}^{y=0.02}$	0.96 ± 0.05
$f_{60vis}^{y=0.04}$	0.98 ± 0.06
$f_{60axis}^{y=0.02}$	0.97 ± 0.06
$f_{60axis}^{y=0.04}$	0.97 ± 0.06

Table 6.7: Average of Ratios of Jet-3 to Jet-2 Values in Each Overlapping Energy Bin ($26.75 \leq E_{jetaxis} \leq 31.25 GeV$) for Events Selected with a Fixed Invariant Mass (y_{cut}) or Different Energy Scaling.

6.6 Discussion.

When considering the variables previously defined, we would expect to see the following differences between the gluon enriched jet-3 sample and quark enriched jets 1 and 2 at a naive level. f_{60x} should be lower in gluon jets than quark jets, whereas $f_{cone5-10}$, $P_t - JetAxis$, P_{out}^2, and N_{ch} should be larger.

As can be seen in figure 6.9, the three energy bins used in the calculation of the $< r_{32} >$ ratios fall across the end point of the jet-3 energy range and the start of the jet-2 range. Therefore, the low statistics afforded by the jet rates in this region may well lead to wild fluctuations in the mean value determined by this method. The $< r_{32} >$ ratios are not in good agreement with the expectations in the case of the variables P_t and P_{out}, but both the core fraction and cone fraction follow the expected trend. However, all of these measures may be erroneous for the same reason.

The stability offered by averaging over all of the energy bins for a particular jet helps to eliminate the bin to bin fluctuations that occur, and it is from these values

that any trends in the data can best be discerned. In the following discussion it is these values that are used when comparing data trends to those anticipated.

Both measures of the core fraction support the supposition that gluon jets are more diffuse than quark jets. This can be seen by a marked decrease of the jet-3 fraction, which is outside the bounds of the error (see tables 6.4 and 6.6). This then does suggest that gluon jets have less of their total energy centred around their axes than do quark jets.

The core fractions determined from events which were clustered and selected using a fixed invariant mass cut to remove 4-jet events, also support this hypothesis. The four combinations (f_{60vis} or f_{60axis} for each value of y_{cut}) yield rises in the core fractions for all three jets. In each case, the jet-1 and jet-2 values increase by the same amount, with the jet-3 increase being typically $\simeq 0.02 - 0.03$ units less. This can be explained simply by the removal of 4-jet events from the data sample. If a 4-jet event is force clustered into a 3-jet topology, one of the three jets will actually consist of two sub-jets and will thus have an inherent diffuseness. The inter-jet region between the sub-jets is effectively the central region of the single jet when they are merged. This jet will consequently have a lower core energy fraction as the central region contains the empty space between the two incorrectly merged jets. The overall increase in core fraction of all three jets implies that the 4-jet contamination was fairly evenly dispersed throughout the jets, but the slightly higher relative differences between jet-2 and jet-3 implies a marginally larger fraction in jets 1 and 2. Due to the larger coupling of the gluon, we would expect the majority of 4-jet events to originate from the branching of the gluon jet (which is generally the lowest energy jet). However, the higher energy of the quark jet may induce increased branching which outweighs that of the gluon, resulting in 4-jet events of quark origin.

However, the effect of a reduced core energy fraction in gluon jets as compared to that of quark jets is still clearly visible and has in fact improved under these circum-

stances. Thus, 4-jet contamination in a 3-jet event appears to effectively reduce any differences and should therefore be carefully monitored.

Moreover, this variable appears to be most sensitive to the narrowing of jets with increasing energy and the compensation that is made for this. The scaling factor used to determine the cone size from which the core energy is determined can drastically affect the results, as can be seen in table 6.6. When using an unscaled cone with a fixed angle of 10° (which should act to under-compensate for increased jet collimation), the difference in core fractions between jet-1 and jet-3 does increase as would be expected. The actual difference of 0.13 units represents an increase of the same order of magnitude as the original effect when the values were determined using the $\sqrt{E}$ scaling (here the jet-1 to jet-3 difference being 0.08 units), yet the maximal change initiated is that the cone size of the lower energy jets is reduced by only $\simeq 2°$. When scaling the cone by a factor $0.2E$ (which should act to over-compensate for increased jet narrowing) again the maximal change is a reduction in cone size of $\simeq 2°$, except this time for the higher energy jets. The expectation that the difference in core fractions between higher and lower energy jets should decrease under these circumstances is upheld. The jet-1 to jet-3 difference being only 0.04 units in this case (half the difference with $\sqrt{E}$ scaling). However, even employing this extreme a scaling, the difference (although smaller) is still present, and it is therefore reasonable to assume that the extra broadness is due to the increased gluonic nature of the jets.

It is therefore evident that the choice of scaling factor is very influential on the overall result, as even the small changes to the cone size above have a marked effect. Therefore, although this variable shows great promise as one that could differentiate between jet species, both theorists and experimentalists must acquire a fuller understanding of how jet widths vary with energy and how the widths are defined. This would then allow fine tuning of the scaling factor, hopefully leading to a more significant result.

Due to the large errors associated with the data points, few conclusions can be drawn here regarding the cone fraction. The main cause of the large error is the width of the distributions of the cone fractions within each energy bin. However, based on the assumption that the fraction of a jet's energy in the 5°-10° region remains fairly constant, then the trend exhibited by the data when averaged over all bins is in the opposite sense to that which would be anticipated. Moreover, although the bin averaged values do show some effect, the data or PS model do not appear to follow any particular pattern as can be seen in figure 6.5. The cone fraction should increase in an enriched gluon sample due to the broadening of the jets which should give a decreased energy deposit in the 0°-5° region. Also, any effect caused by jet narrowing attributed to increasing jet energy should further increase the cone fraction in lower energy jets compared to those of higher energy, as again less energy is expected in the 0°-5° region.

The transverse momentum does tend to agree with the presumption that gluon jets have a less soft P_t spectrum, but P^2_{out} and N_{ch} do not show any significant differences which may have been anticipated. The absence of any difference in the P^2_{out} values of the three jets may well be attributable to the planar nature of 3-jet events. The transverse momentum of each jet may well be constrained to lie in the event plane (particularly if one considers the concept of string fragmentation). This reasoning is supported by the observed difference in momentum transverse to the jet-axis P_t, which does not take account of how much a particle is directed into or out of the plane. The charged multiplicity, although failing to highlight any differences between the jet species, is highly dependent upon the formation of a jet from the data. The misassignment of some of the many soft particles in the outer regions of the jets may well swamp the effect we seek, so we should perhaps not be surprised at the lack of progress made with regard to this variable.

Finally comment must be made concerning the 19, 28, 53% gluon content of jets 1,2,3. Though, it should be pointed out that these values were determined from force

clustered parton level events and may therefore not be precisely the same for events selected with fixed y_{cut}. If the above suppositions regarding P^2_{out} and N_{ch} are correct, i.e. transverse momentum is constrained within the event plane and particles are mis-assigned by the clustering routine, then this factor would have little effect on these variables anyway, as they would either not be affected by the quark or gluon content of a jet, or would be suppressed by clustering uncertainties. However, P_t appears to increase by just under $\simeq 0.001$ units per extra percent of gluon content present in the jet (but note should be made of the ± 0.007 unit error). The trend in the core energy fraction is also quite linearly related to gluon content. In the fixed y_{cut} selected events, the jet-1 and jet-2 difference equates to an approximate 0.01 unit decrease for each extra 2% of gluon content, and the jet-1 to jet-3 difference to a similar amount for each additional $2\frac{1}{2} - 3\%$. The difference in the force clustered events, being affected by 4-jet contamination does not quite fit this pattern, but does tend in the right direction.

6.6.1 Other Experimental Results.

As can be seen from other works [43,49,50,51,52,53,54], several authors have also addressed the problem investigated here. However, nothing conclusive has been established to date, and often, different experiments offer conflicting results.

The AMY collaboration [49,50] have examined the core energy fraction, transverse momentum to the jet axis and charged multiplicity of planar 3-jet events over an energy range $\sqrt{s} = 50.0 - 60.8 GeV$. They have observed a definite decrease in the the core fraction of the lowest energy jet (jet-3), and a minor increase in the P_t (using charged and neutral particles) and N_{ch} values relative to the two higher energy jets. However, the data has not been corrected so a quantitative difference has not been quoted.

JADE [51] combined planar 3-jet events at C.M. energies $\sqrt{s} = 22.0 GeV$ and $\sqrt{s} = 29.0 - 36.4 GeV$. This greatly improves the frequency of jets in the jet-2 - jet-3 overlap regions. They have determined the following values :- Transverse momentum to the jet

axis $< r_{32} > = 1.16 \pm 0.02$ for P_t using charged and neutral particles, and $< r_{32} > = 1.18 \pm 0.02$ for P_t with only charged particles. Momentum out of the event plane P_{out} yielded $< r_{32} > = 1.16 \pm 0.02$ but no difference was observed in multiplicity. Particle and energy flow within the jets was also tested. Jet-3 showed a decrease relative to jet-2 in the angular region $0° - 25°$ about the jet axis but vice-versa in the region $25° - 60°$.

The TASSO experiment [52] using symmetric ($\theta_{ij} > 55°$) events at $\sqrt{s} = 34.6GeV$ report on squared momentum out of the event plane P^2_{out}, however, their result of $< r_{32} > = 1.01 \pm 0.03$ does not suggest any apparent variations between the jets. In a later publication [43] they quote results from other groups, mainly that CELLO, comparing the lowest energy jets from three jet events at $\sqrt{s} = 35GeV$ to two jet events at $\sqrt{s} = 14GeV$ observe $< P_t(35) > / < P_t(14) > = 1.03 \pm 0.03$; and the TPC collaboration using three jet events at $\sqrt{s} = 29GeV$ see $< r_{32} >$ of $P_t = 1.08 \pm 0.02$.

In an earlier work, the High Resolution Spectrometer (HRS) experiment [53] looked at the charged multiplicity ratios of planar 3-jet events at $\sqrt{s} = 29GeV$, and quote a ratio $< n >_g / < n >_q = 1.29 \pm 0.20^{+0.21}_{-0.41}$, thus seeing no significant difference between the two jet species.

More recently, OPAL [54] at LEP employed a novel approach, which combined energy ordering of three jet events with lepton tagging of heavy flavour decays to identify one (two if a double tag existed) of the jets as quark induced. Comparisons were made between the two lower energy jets. When investigating the particle energy spectrum, the gluon jets displayed a softer distribution nearer the jet cores, but the mean particle energies were about the same for both jet types in the outer regions. A ratio of gluon to quark jet multiplicities gave values of $< n >_g / < n >_q = 1.03 \pm 0.03^{+0.15}_{-0.00}$ for charged and neutral particles and $< n >_g / < n >_q = 1.02 \pm 0.04^{+0.06}_{-0.00}$ with only charged particles. (The second error here is not truly systematic, but is due to the difference in values determined from a sample using all quark jets, and those which are heavy flavour lepton tagged events). However, the distribution of the multiplicity

exposed a depletion in the gluon jet core region and an increase in the outer region relative to the quark jet. The same trend was manifested in the transverse momentum variables P_{in} and P_{out}, where the ratios of the means of the distributions showed little difference between the jet categories. However, when the distributions were fitted and the widths compared, differences were revealed yielding $\sigma_g^{in}/\sigma_q^{in} = 1.42 \pm 0.08^{+0.04}_{-0.00}$ and $\sigma_g^{out}/\sigma_q^{out} = 1.46 \pm 0.14^{+0.06}_{-0.00}$.

Of all of the variables considered, the core energy fraction shows the most marked difference, but note should be made of the effects caused by varying the scaling factor used to define the cone size from which the core energy is determined, and this may require much more fine tuning before we can be certain. However, this result is supported by the similar observations of the AMY group. Both OPAL and JADE investigated the energy flow of particles within the jets, which is in essence the same measure as the core fraction. A lower energy concentration in the core region of jet-3 relative to the higher energy jets was observed by both teams.

No effect was exhibited by comparing the average multiplicities of the jets, which is in agreement with the results of all of the other experiments. It therefore seems that differences in multiplicity observed at the parton level when investigating the colour charge ratio R, are somehow lost in the hadronization process and do not transpire in the final state particles. Additionally, misassignment of particles by the jet clustering algorithm employed could also account for the absence of any difference. However, JADE and OPAL have reported differences in the particle flow within the jets, such that jet-3 has a lower concentration of particles in its core region and an increase in its outer region relative to jet-1 and jet-2.

With the exception of JADE, all measures of transverse momentum are consistent in that no difference can be discerned between the jet species. Again however, these comparisons are based on mean values, but the shape of the distribution for each jet would seem to differ judging by OPAL's result.

It appears that differentiating jet types by comparing mean values of a certain variable is unsatisfactory. However, the multiplicity distribution within the jet does seem to change, in that the gluon jet has fewer particles near the jet axis and more further away, relative to the two quark jets. This is in accord with the observations of the core fraction and energy and particle flows which depend on the particles' directions relative to the jet axis. This is not to say that the other variables should be discarded. On the contrary, it may well prove fruitful to reanalyse the data, but by looking at the shape of each distribution rather than its mean value, as the particle density about the jet axis does seem to be the influential factor.

Additionally, variables that can be studied at the parton level with Monte Carlo would be good choices, as a comparison could be made between parton and hadron level results. This would hopefully provide us with a greater understanding of the fragmentation process. Also, by fitting Monte Carlos to the data, the values of parameters describing a jet could be ascertained. i.e. the width of the transverse momentum distribution and hadronization properties. Again, this would increase our knowledge of the hazy area of hadronization.

6.7 Conclusion.

A sample of symmetric 3-jet events from e^+e^- annihilations at LEP energies ($\sqrt{s} = 91.2GeV$) has been studied in an attempt to ascertain differences between quark induced and gluon induced hadronic jets of particles. However, we are still in the unfortunate position of being unable to unambiguously define the two species as the variables considered did not highlight any significant variations.

Differences predicted by QCD at the parton level do not manifest themselves clearly in the final hadronic phase, which is particularly evident in the ratio of charged multiplicity of the jet types. The experimental value is consistent with being equal to unity

- somewhat less than the naive expectation of 9/4 or even the modified prediction of $\simeq 1.5$ for present energies.

Never the less, the search does generally appear to be heading in the right direction, as the trends shown by the data suggest a breakthrough is tantalisingly close. Observations of the core energy fraction and particle flow imply that future work should aim towards studies of the angular distribution of the multiplicity within a jet, as although the mean values of the distributions of the jet variables are often similar, the two jet varieties seem to exhibit differing 'hard' and 'soft' regions within a distribution. Additionally, the improved statistics which future data will afford should also help to clarify any uncertainties that are presently held.

Appendix A

Statistical Methodology.

In most of the distributions considered, a variable $< x >$ is shown as a function of $E_{jetaxis}$. Here $< x >$ is the mean value of the distribution of x within the bounds of each energy bin. The error is statistical only and is calculated as $e = \sigma_x/\sqrt{n}$ where σ_x is the standard deviation of the x-distributon and n is the number of entries.

To combine uncorrelated distributions, as is necessary to correct the data (see chapter 5) or when calculating the r_{32} values, equations A.1 and A.2 are used. The resulting distribution is denoted by a and the input distributions by b and c.

$$a = b^r c^s \tag{A.1}$$

$$\left(\frac{e_a}{a}\right)^2 = r^2\left(\frac{e_b}{b}\right)^2 + s^2\left(\frac{e_c}{c}\right)^2 \tag{A.2}$$

Then for linear combinations when $r = s = \pm 1$

$$e_a = a\sqrt{\left(\frac{e_b}{b}\right)^2 + \left(\frac{e_c}{c}\right)^2} \tag{A.3}$$

When calculating the average value of all $< x >$ across all energy bins for a single jet (i.e. 1,2,3), then the weighted linear method is used.

$$< y >= \frac{\sum_{i=1}^{n_{bins}} < x >_i / e^2_{<x>i}}{\sum_{i=1}^{n_{bins}} 1/e^2_{<x>i}} \tag{A.4}$$

and

$$\frac{1}{e_y^2} = \sum_{i=1}^{n_{bins}} \frac{1}{e^2_{<x>i}} \tag{A.5}$$

References

[1] David Griffiths, *Introduction to Elementary Particles,* John Wiley and Sons 1987.

[2] Donald H. Perkins, *Introduction to High Energy Physics,* Addison and Wesley 1987.

[3] I. J. R. Aitchison and A. J. G. Hey, *Gauge Theories in Particle Physics,* Adam Hilger 1989.

[4] Francis Halzen and Alan D. Martin, *Quarks and Leptons: An Introductory Course in Modern Particle Physics,* John Wiley and Sons 1984.

[5] E. D. Commins and P. H. Bucksbaum, *Weak Interactions of Leptons and Quarks,* Cambridge University Press 1983.

[6] O. W. Greenberg, American Journal of Physics 50 (12) December 1982.

[7] H. J. Lipkin, *Quarks For Pedestrians,* Physics Reports 8 No.3 (1973).

[8] H. D. Politzer, *Asymptotic Freedom: An Approach to Strong Interactions,* Physics Reports 14 No.4 (1974).

[9] O. W. Greenberg, *Spin and Unitary-Spin Independence in a Paraquark Model of Baryons and Mesons,* Phys. Rev. Lett. 13 598 (1964).

[10] M. Gell-Mann and Y. Ne'eman, *A Schematic Model of Baryons and Mesons,* Phys. Lett. 8 214 (1964).

[11] G. 'tHooft, *Renormalization of Massless Yang-Mills Fields,* Nucl. Phys. B33 173 (1971).

[12] G. 'tHooft, *Renormalizable Lagrangians for Massive Yang-Mills Fields,* Nucl. Phys. B35 167 (1971).

[13] F. H. Combley, *(g-2) Factors for the Muon and Electron and Consequences for QED,* Rep. Prog. Phys. 42 1889 (1979).

[14] G. Kramer and B. Lampe, *Two Jet Cross section in e^+e^- Annihilation,* Z. Phys. C34 497 (1987).

[15] G. Kramer and B. Lampe, *Jet Cross sections in e^+e^- Annihilation,* DESY 86-119 (1986).

[16] D. H. Saxon, *Quark and Gluon Fragmentation in High Energy e^+e^- Annihilations,* RAL-86-057 July 1986.
T. Sjöstrand, *QCD and Jets at LEP,* CERN-TH 5902/90 October 1990

[17] B. Andersson et al., *Parton Fragmentation and String Dynamics,* Phys. Rep. 97 33 (1983).
T. Sjöstrand, *The LUND Monte Carlo for e^+e^- Jet Physics,* Comp. Phys. Comm. 28 229 (1983).

[18] W. Bartel et al. (JADE Collaboration), *Experimental Studies of Jets in e^+e^- Annihilation,* Phys. Lett. 101B 129 (1981).

[19] *LEP - Large Electron Positron Storage Ring. Technical Notebook,* CERN Publication (1989).

[20] D. Schlater and G. Redlinger, *ALEPH in Numbers,* ALEPH Publication.

[21] D. Decamp et al., *ALEPH: A Detector for Electron-Positron Annihilations at LEP.,* Nuclear Instruments and Methods in Physics Research A294 (1990) 121.

[22] ALEPH Collaboration, W. Blum (Editor), *The ALEPH Handbook 1989,* ALEPH 89-77(1989).

[23] P. Holl et al., *The ALEPH Minivertex Detector,* Nuclear Instruments and Methods in Physics Research A257 (1987)587-590.

[24] W. B. Atwood et al., *Performance of the ALEPH Time Projection Chamber,* CERN PPE/91-24(1991).

[25] J. Knobloch and P. Norton, *Status of Reconstruction Algorithms for ALEPH,* ALEPH Internal Note (1991).

[26] I. Videau, *The Data Acquisition System for ALEPH,* IEEE Transactions on Nuclear Science, Volume NS-32, No. 4, p1484-9 August 1985.

[27] W. Von Rüden, *ALEPH Contributions to the Real Time 89 Conference, Williamsburg, Virginia,* ALEPH 89-116(1989).

[28] P. Mato et al., *ALEPH Contributions to the Real Time 89 Conference, Williamsburg, Virginia,* ALEPH 89-116(1989).

[29] B. Bloch-Devaux, *KINLIB Documentation,* ALEPH 91-078 PHYSIC 91-071.

[30] M. Bengtsson and T. Sjöstrand, *The LUND Monte Carlo Programmes for Jet Fragmentation and e^+e^- Physics - JETSET Version 7.3,*

[31] I. R. Tomalin, *Track Finding Efficiency in the Central Detector,* ALEPH 89-135 SOFTWR 89-18.

[32] G. Altarelli, R. Kleiss, C. Verzegnassi, *Z Physics at LEP 1 - Vol. 3 Event Generators and Software,* CERN 89-08 21 October 1989

[33] S. J. Brodsky, T. DeGrand, R. Schwitters, *Are Gluon Jets Oblate,* Phys. Lett. 79B 255 (1978).

[34] J. F. Gunion and G. Bertch, *Hadronization by Colour Bremsstrahlung,* Phys. Rev. D25 746 (1982).

[35] S. J. Brodsky and J. F. Gunion, *Hadron Multiplicity in Colour-Gauge Theory Models,* Phys. Rev. Lett. 37 402 (1976).

[36] A. Bassetto et al., *Inelastic Distributions and Colour Structure in Perturbative QCD,* Nucl. Phys. B163 477 (1980).

[37] Z. Fodor, *How to See the Differences Between Quark and Gluon Jets,* Phys. Rev. D41 No.5 402 01 March 1990.

[38] B. R. Weber, *A QCD Model for Jet Fragmentation Including Soft Gluon Interference,* Nucl. Phys. B238 492-528 (1984).

[39] S. D. Ellis, Z. Kunszt, D. E. Soper, *One Jet Inclusive Cross Section at Order α_s^3: Gluons Only,* Phys. Rev. Lett. 62 726 (1989).

[40] W. Bartel et al. (JADE Collaboration), *Experimental Studies on Multijet Production in e^+e^- Annihilation at PETRA Energies,* Z. Phys. C33 23-31 (1986).

[41] D. Decamp et al., *Measurement of α_s from the Structure of Particle Clusters Produced in Hadronic Z Decays,* Phys. Lett. 257B 479-491 (1991).

[42] M. Z. Akrawy et al., *A Study of Jet Production Rates and a Test of QCD on the Z^0 Resonance,* Phys. Lett. 235B 389 (1990).

[43] W Braunschweig et al. (TASSO Collaboration), *Comparison of Inclusive Fractional Momentum Distributions of Quark and Gluon Jets Produced in e^+e^- Annihilation,* Z. Phys. C45 1-10 (1989).

[44] T. Sjöstrand, *QCD and Jets at LEP,* CERN TH.5902/90

[45] G. Altarelli and G.Parisi, *Asymptotic Freedom in Parton Language.* Nucl. Phys. B126 298-318 (1977).

[46] G. Cowan, *Private Communication.*

[47] Yu. L. Dokshitzer, V. A. Khoze, S. I. Troyan, *Coherence and Physics of QCD Jets,* DESY 88-093 July 1988 sections 7.3.1 - 7.3.4.

[48] Yu. L. Dokshitzer, D. I. Dyakonov, S. I. Troyan, *Hard Processes in Quantum Chromodynamics,* Phsics Reports 58 No. 5 (1980) 269-395.

[49] Y. K. Kim et al. (AMY Collaboration), *Comparison of Quark and Gluon Jets Produced In High-Energy e^+e^- Annihilations,* Phys. Rev. Lett. 63 1772 (1989).

[50] Y. K. Kim et al. (AMY Collaboration), *Comparison of Quark and Gluon Jets Using Three-Jet Events from e^+e^- Annihilation at TRISTAN,* KEK 90-79 AMY 90-10 (1990).

[51] W. Bartel et al. (JADE Collaboration), *Experimental Evidence for Differences in $< P_t >$ Between Quark Jets and Gluon Jets,* Phys. Lett. 123B 460 (1983).
Particle Distribution in 3-Jet Events Produced by e^+e^- Annihilation, Z. Phys. C21 37-52 (1983).

[52] M. Althoff et al. (TASSO Collaboration), *A Study of 3-Jet Events in e^+e^- Annihilation into Hadrons at 34.6 GeV c.m. Energy,* Z. Phys. C29 29-40 (1985).

[53] M. Derrick et al. (HRS Collaboration), *Comparison of Charged Particle Multiplicities in Quark and Gluon Jets Produced in e^+e^- Annihilation at 29GeV,* Phys. Lett. 165B 449 (1985).

[54] G. Alexander et al. (OPAL Collaboration), *A Direct Observation of Quark-Gluon Jet Differences at LEP,* Phys. Lett. 265B 462 (1991).